Importance of meteorology on dispersion of air pollution in the surface layer. The use of modeled and observed meteorology in dispersion models

ELIN CECILIE RISTORP AAS

Thesis submitted for the Degree of
Master of Science in Meteorology and Oceanography
60 Credits

Department of Geosciences
Faculty of Mathematics and Natural Sciences

UNIVERSITY OF OSLO

August 15, 2018

Importance of meteorology on dispersion of air pollution in the surface layer. The use of modeled and observed meteorology in dispersion models

This work is published digitally through DUO – Digitale Utgivelser ved UiO
http://www.duo.uio.no/

Printed: Reprosentralen, University of Oslo

Abstract

Air pollution from traffic is a major health problem in urban areas, and there is a great interest in modeling and measuring the dispersion of pollutants from near-ground sources. Due to the complex nature of the motions in the boundary layer, it is not straightforward to obtain the necessary meteorological data to perform dispersion calculations.

This thesis present a study on the use of modeled meteorological data and locally observed data in dispersion calculations. The thesis will also investigate the importance of different micrometeorological variables on the calculations. The Research LINE model (RLINE) and the dispersion model EPISODE have been run with meteorological input from both locally measured observations, and modeled meteorology from the Weather Research and Forecasting model (WRF). To evaluate the model results, concentrations of NO_2 have been measured with passive samplers near a road in close proximity to the meteorological observation site. The measurements were conducted in winter and spring conditions.

The results indicate that the effects of thermal instability have a larger impact on dispersion calculations than mechanically generated turbulence.

The differences in wind speed between measured and modeled meteorology were generally large. A sensitivity test gave concentration reductions in the range of 38%-57% when increasing the lowest wind speed to the same magnitude as the highest wind speeds.

The study reveals several challenges connected to the use of both modeled and measured meteorology for dispersion purposes, and it has not been possible to say that one is more advantageous than the other.

Acknowledgements

First and foremost I would like to thank my main supervisor, Erik Berge for giving me the opportunity to write my thesis about an interesting and challenging topic. I would also like to thank my co-supervisor Terje Koren Berntsen for always answering any question.

A big thanks to several NILU employees for being so kind, and taking their time to help me with EPISODE. Gabriela Sousa Santos, for everything from model installation and input preparation to random questions. Henrik Grythe for preparing and explaining the emission setup, and Thorleif Weydahl for great help with installing the model on my computer.

Anne Claire Fouilloux at MetOs also deserves a big thanks, for always having a solution to any computer-related problem.

Last, but not least, thanks to my fellow students for sharing laughs, frustrations and knowledge, it would not have been the same without you!

Oslo, 15.08.18
Elin Ristorp Aas

Contents

Chapter 1

Introduction

1.1 Background

We live and breath in the lowermost part of the atmosphere, the Planetary Boundary Layer (PBL). This is also where most air pollutants are emitted. The dynamics in this layer are greatly affected by the presence of the earth's surface, with buildings, vegetation and other disturbances. Small-scale turbulent motions arise from the exchange of heat, momentum and energy between the surface and the air above. Because of their complexity, these turbulent motions are not practically possible to describe or forecast from the "usual" equations of motion. Instead, statistics, similarity theory or other types of parameterizations are used [Stull, 1988]. The description of the surface layer parameters has been a great challenge to atmospheric scientists for several decades. Even with the massive technological progress in science the last century, many of the theories developed in the 1940's to the 1960's are still widely used today. An example is the similarity theory developed by Monin and Obukhov [Monin and Obukhov, 1954].

One of the main reasons for the interest in describing the boundary layer conditions is to predict how different kinds of emissions spread from near-ground sources. This is relevant for many different scenarios, like predicting the damage of accidental emissions from industry, predicting how smell spread from a garbage dump, or how pollution from traffic affect an area. To help determine the spread, different kinds of dispersion models have been developed. Some are based on a Lagrangian approach, while others uses an Eulerian approach. Some models are built as a combination of the two. One of the most widely used concepts for modeling point and line sources, is the Gaussian dispersion distribution. That the concentration distribution is Gaussian in shape, is in many cases a rather uncertain assumption. Still, if it is used with carefully chosen input, the result is generally regarded as an acceptable compromise between accuracy and computational time. The dispersion models requires information about the surface layer parameters mentioned above, in addition information about wind speed and direction.

In an urban area, measurements of meteorological variables like wind and temperature are difficult, because the effect of buildings and anthropogenic heat emissions influence the measurements. This means that the measurements only describe the conditions very close to the observation site. The parameterization of the turbulent

motions are also further complicated by the effect of a city. It can therefore be tempting to turn to weather prediction models for providing the parameters needed to perform dispersion calculations. Provided that the model are capable of predicting the near-surface meteorology in a satisfactory manner, this may be a less resource demanding way of calculating concentrations. It is therefore of interest to explore this opportunity further.

The quality of the air we breathe has a large impact on our health. Both long and short term exposure to air pollutants have been linked to several negative health effects. Asthma, cardiovascular diseases and premature deaths are some of the main concerns, and children and elderly are most vulnerable. (`https://www.fhi.no/publ/2013/luftkvalitetskriterier---virkninger/`). People who live and work in urban areas are extra exposed to these pollutants. To minimize the negative health effects, both reduction of pollutants and mitigation of the human exposure time is desirable. In order to control the exposure, both observation and modeling of pollution are essential. The fact that there are so many challenges and uncertainties associated with modeling dispersion of pollutants, that has so many negative health effects is thought-provoking, and trigger further investigations on the topic.

1.2 Description of this study

In order to investigate how meteorological conditions are reflected in dispersion models, we wanted to compare observed air pollution concentrations with modeled concentrations. More specifically, we wanted to look at how the pollution concentration gradient changes outwards from a line source, typically a road, and how well models are able to reflect this gradient. Focus has been on the meteorological parameters used as input to the models, how they are obtained, and how they affect the dispersion calculations. We chose to use passive samplers to measure the concentration of NO_2. This is a simple, yet effective tool to measure pollutants. Because they are small and don't require electricity, passive samplers are attractive for air quality management purposes [Denby and Sundvor, 2008]. NO_2 is one of the air pollutants with largest health effects in urban areas. Samplers for NO_2 are cheap, and readily available, and it was therefore decided to do measurements of this species in the study. Bjørvika, the area in which the samplers were placed was chosen because it has the characteristics of an urban area. In addition, much construction work and city planning are still going on, which makes it desirable to investigate the exposure of this area further. Fig. 1.1 shows already built, and ongoing building projects in Bjørvika. Many people will live, work and go to school here, and thereby be exposed to the pollution from the roads in the area. Another important reason for the choice was the opportunity to evaluate the use of locally measured meteorological data. Availability of measured meteorological data in urban areas is limited, and it was desirable to investigate how the use of this meteorology affect dispersion calculations.

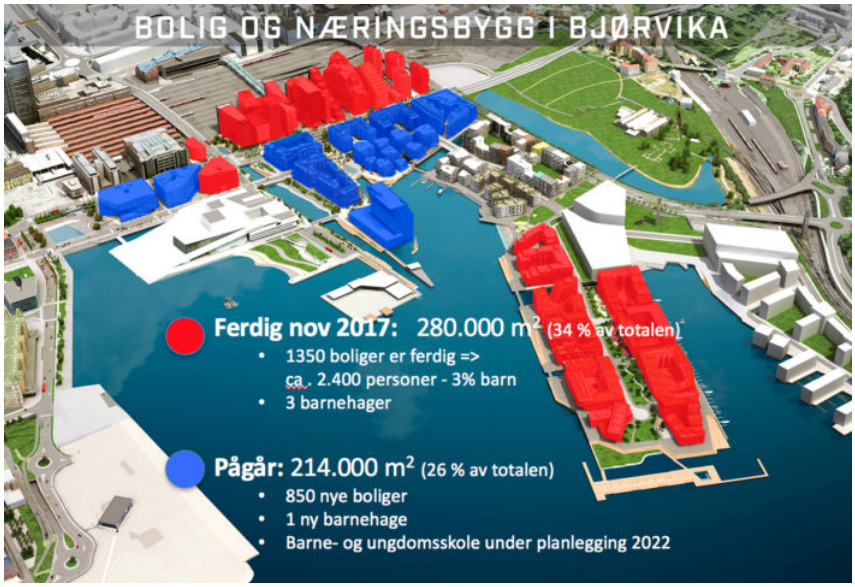

Figure 1.1: City developement in the Bjørvika area. The red buildings are finished, while the blue are ongoing projects in 2018. Source: `www.bjorvikautvikling.no/portfolio-item/bolig-og-naering/`.

Concentrations of NO_2 were measured and modeled for three periods during winter and spring in 2018. The pollution measurements were conducted simultaneously as a meteorological measurement campaign performed by Pernille Borander, a fellow master student at the University of Oslo. In her study, wind and temperature sensors were placed at different heights in a tower crane in the same area as the passive samplers. She also ran the numerical weather prediction model WRF for that period of time. Her work will be referred to as *Borander's master thesis* in this study.

The two types of meteorological input have been used in two different dispersion models, namely the EPISODE model, developed by the Norwegian Institute for Air Reasearch (NILU) [Slørdal et al., 2003] and the Research LINE model, RLINE [Snyder et al., 2013].

The models have been run for the same periods as the concentration measurements, in order to compare model performance with the observations. The results from the models will also be compared to each other.

The aim is to investigate how meteorological conditions affect the performance of the models. The relative importance of different meteorological parameters will be presented, and consequences of this will be discussed. In addition, we will look into the difference between using modeled and observed meteorology in the dispersion models, and discuss the challenges of both approaches. Based on the result, we will present suggestions and improvements for future studies on the topic of dispersion modeling and observations in urban areas.

Chapter 2

Theory

To determine the spread of pollution, dispersion models need information about meteorological parameters, like wind velocity, stability conditions and surface fluxes. Due to the complex nature of the boundary layer, mentioned in the introduction, this information is not straightforward to find. Therefore, a thorough introduction to boundary layer theory and its challenges will be given, before turning to the more practical use of the parameters in dispersion models.

2.1 Boundary layer meteorology

The lowest part of the troposphere is called the Planetary Boundary Layer (PBL), alternatively the Atmospheric Boundary Layer (ABL). According to Stull [1988, p.2] the PBL can be defined as "*that part of the troposphere that is directly influenced by the presence of the earth's surface and responds to surface forcings with a timescale of about an hour or less.*" An idealized representation of the PBL is given in Fig. 2.1. The figure show a diurnal variation of the PBL in fair weather over land. This variation is a consequence of the radiative heating and cooling of the earth's surface from the sun. After sunrise the ground quickly heats to temperatures higher than the air above. This leads to the creation of rising thermals that rapidly mixes the air, and the daytime mixed layer is established. After sunset the ground becomes colder than the air, the thermals ceases, and a stable boundary layer appears. The residual layer above holds remains of moisture, heat and pollutants from the previous mixed layer. The limit between the PBL and the free atmosphere is defined by a capping inversion. In this layer temperature increases with height, causing very stable conditions. This stable area works as a lid, preventing the well mixed air in the PBL to mix with the free atmosphere above. However, air from the free atmosphere can be entrained into the PBL underneath, causing the PBL to grow during daytime.

The lowest 10% or so of the PBL is called the surface layer. Here, the wind, temperature and humidity vary a lot with height due to interactions with the surface. However, the vertical, turbulent fluxes of heat, momentum and mass typically vary with less than 10% of their magnitude [Stull, 1988]. For this reason, one often assumes that these fluxes are constant in the surface layer. The turbulent fluxes will be discussed more in Section 2.1.1. In addition, the effect of the Coriolis force

is neglectable on the surface layer scales. These assumptions makes it possible to derive relatively simple expressions for describing the atmospheric motions close to the surface, like the Monin Obukhov similarity theory that will be described in Section 2.1.3.

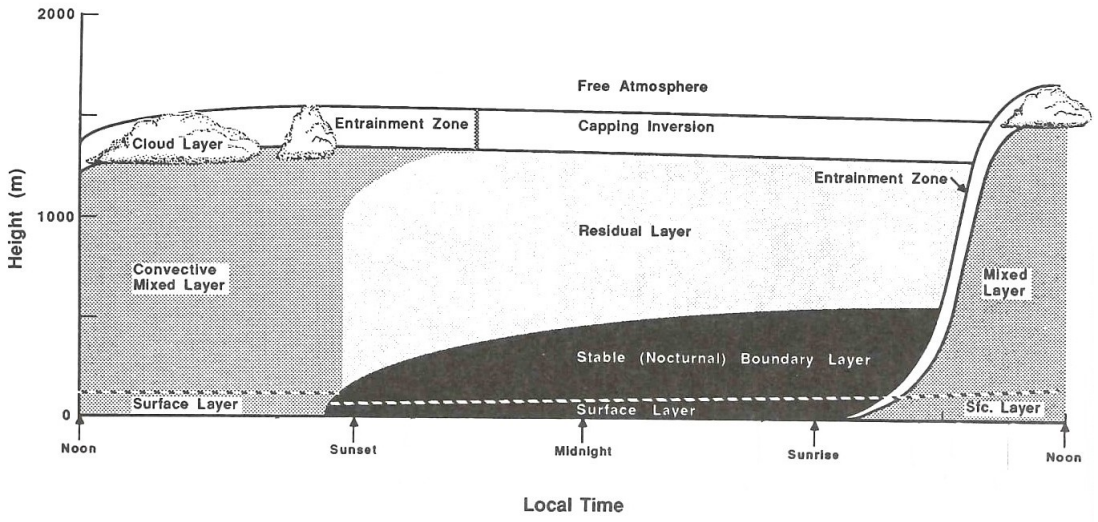

Figure 2.1: Ideal representation of the diurnal variation of the Planetary Boundary Layer. Adapted from Stull [1988].

It should be noted that the diurnal variation in Fig. 2.1 is not very pronounced in winter conditions with short days, low temperature and possibly snow covering the ground. Topography and surface elements like buildings and trees will also affect the evolution of the boundary layer. Still, the fact that the PBL is shallower (deeper) in stable (unstable) conditions is an important feature in dispersion of pollutants in the boundary layer. For example, in a stable boundary layer (SBL) with light winds, the concentration of pollutants will accumulate in the shallow layer near the ground and can cause severe pollution episodes. Dispersion in light winds are difficult to predict, so these cases are also the hardest to model accurately [Qian and Venkatram, 2011]. To better understand the complex motions of the PBL air, the concept of turbulence needs to be explored.

2.1.1 Turbulence

The theory in this section is largely based on Chapter 5 in Stull [1988] and Chapter 9 in Wallace and Hobbs [2006]. Whenever there is a difference in say temperature, concentration or pressure in the atmosphere, nature will try to even it out and reach equilibrium. In this process turbulent motions will occur. The nature of turbulent motion is highly non-linear, hence almost impossible to predict deterministically. Instead, different statistical variables are used to describe turbulent behavior. Two such variables are the *variance* and the *covariance*. To define these, we need to split the variable into two parts, one mean component and one turbulent component. This can be done by *Reynold's averaging* and is illustrated for a variable, x, in Eq. (2.1). x can be any fluctuating variable, for example pressure, temperature or wind

speed.

$$x = \bar{x} + x' \tag{2.1}$$

x is the instantaneous value, $\bar{x}$ is the mean, and x' is the fluctuating component. The variance is defined as

$$\sigma_x^2 = \frac{1}{N}\sum_{i=1}^{N}(x_i')^2 = \overline{(x')^2} \tag{2.2}$$

Here, N is the number of sampling intervals of x. The variance indicates the amount of kinetic energy that is associated with the turbulent motions. The standard deviation, $\sqrt{\sigma_x^2}$, can be seen as an average turbulent pertubation. If, for example, x represent wind speed, the standard deviation represent the average gustiness of the wind [Stull, 2012].

The covariance between two variables x and y is defined as

$$cov(x, y) = \frac{1}{N}\sum_{i=1}^{N}(x_i')(y_i') = \overline{x'y'} \tag{2.3}$$

This describes how change in a variable x can be related to change in another variable, y. The covariance also works as a measure of the turbulent flux/transport of different scalars. Of special interest in PBL meteorology are the vertical, kinematic heat flux, $\overline{w'\theta'}$, the vertical, kinematic momentum flux, $\overline{u'w'}$, and the vertical, kinematic water vapor flux, $\overline{q'w'}$. w, θ, u, and q are the vertical wind, potential temperature, horizontal wind and humidity, respectively. The primes show that they are the fluctuating parts of the instantaneous values.

If the turbulent statistics do not vary in time, the flow is said to be *stationary*. If they do not change in space, the flow is *homogeneous*. The flow is *isotropic* if the flow is homogeneous in all directions, both horizontal and vertical. These situations happens rarely, or not at all in the real PBL, and never over longer periods in time. Diurnal variations and the passing of synoptic and mesoscale weather systems makes stationarity virtually impossible. Horizontal homogeneity can only occur if the surface is flat and smooth, that is, no trees, buildings etc. Although these ideal situations are not descriptive of the real world, they are often used to simplify equations. For example, the Gaussian plume equation, which is discussed in Section 2.2 is based on (among others) assumptions of stationarity and horizontal homogeneity. Still, this equation has been shown to give satisfactory results, despite of the large assumptions it is based on.

Turbulent Kinetic Energy (TKE)

Turbulent Kinetic Energy (TKE) is a measure of the intensity of turbulence. Specific TKE is defined as $\bar{e} = TKE/m = \frac{1}{2}(\overline{u'^2} + \overline{v'^2} + \overline{w'^2})$, m is mass of the air. Eq. (2.4) is a simplified version of the TKE budget equation (see Stull [1988]) that describes different sources and sinks of turbulence in the atmosphere. In this equation horizontal homogeneity is assumed and subsidence neglected. The coordinate system has been aligned with the mean wind direction, so that $\overline{U}$ represents the

total wind following the x-axis. This means that $\overline{V} = 0$.

$$\frac{\partial \bar{e}}{\partial t} = \underbrace{\frac{g}{\overline{\theta}_v}\overline{w'\theta'_v}}_{\text{buoyancy}} - \underbrace{\overline{u'w'}\frac{\partial \overline{U}}{\partial z}}_{\text{shear}} - \underbrace{\frac{\partial\left(\overline{w'e}\right)}{\partial z}}_{\text{transport}} - \underbrace{\frac{1}{\overline{\rho}}\frac{\partial\left(\overline{w'p'}\right)}{\partial z}}_{\text{pressure correlation}} - \underbrace{\epsilon}_{\text{dissipation}} \tag{2.4}$$

Here, g, is the gravitational constant,θ_v is the virtual temperature, ρ is density, and p is pressure. The term on the left side can be regarded as a storage term for TKE that grows when the magnitude of the sources exceeds the sinks on the right hand side, and vice versa. In stationary conditions, this term is zero.

The buoyancy term consist of the buoyancy parameter $g/\overline{\theta_v}$ and the vertical heat flux, $\overline{w'\theta'_v}$. The term will act as a source when the turbulent heat flux is positive and a sink when the heat flux is negative. $\overline{w'\theta'_v}$ is defined as positive when the ground heats the air above.

The mechanical shear term consists of the vertical momentum flux, $\overline{u'w'}$ and the mean wind shear, $\frac{\partial \overline{U}}{\partial z}$. They often have opposite signs because the wind normally increases with height. Therefore, the term usually contributes as a source to the TKE budget.

The transport term describes how turbulence can transport itself. This term does not really generate or consume TKE, it just moves it from one location to another. The same is the case with the pressure correlation term.

Turbulence is dissipative. That means that turbulent motions will die out if there is no generating effects feeding it. The dissipation term, ϵ, represent this loss of turbulence into heat.

In this study, focus will be on the buoyancy and shear term, which are useful quantities for analyzing the stability conditions in the PBL.

Turbulence closure

When Reynolds averaged variables are used in the equations of motion, a number of extra terms appear in the expressions. These are nonlinear, turbulent flux terms that cause difficulties when trying to solve the equations. The fluxes are generally not known, so there are more unknowns than equations in the system. If we try to express them with prognostic equations, the result is even more unknowns with higher order. This is the so called closure problem of turbulence. In order to close the system the turbulent terms needs to be parameterized in some way. Depending on their statistical order, parameterizations are divided into categories. A 0th order closure parameterize the variable in question directly, while a 1st order closure parameterize the flux terms, like $\overline{w'\theta'}$. A common 1st order closure is gradient transport theory, also called K theory. By assuming that turbulent transport is analogous to molecular diffusion, it is stated that the flux is proportional to the negative gradient of the variable in question. For example, the turbulent heat flux is expressed as

$$\overline{w'\theta'} = -K\frac{\partial \bar{\theta}}{\partial z} \tag{2.5}$$

where $\frac{\partial \bar{\theta}}{\partial z}$ is the vertical gradient of the mean potential temperature and K is the eddy diffusivity. This is a complex parameter, and the main challenge is to determine

K in a good way.

A widely used 0th order closure is similarity theory, that will be discussed in more detail in Section 2.1.3.

2.1.2 Atmospheric stability

The level of stability governs how the air moves vertically in the atmosphere. A layer in the PBL is *statically stable* if the potential temperature for the air above is higher than for the air below. Because warm air is less dense than cold air, an air parcel will return to its initial position if exposed to a vertical perturbation. If the air below has higher potential temperature than the air above, the vertical perturbation will lead the parcel to continue the movement, which in turn can lead to generation of turbulence. This state is called *statically unstable*. The static stability is determined by the buoyancy of the air. A layer that is statically stable can still be *dynamically unstable*. The dynamic stability is connected to the shear term in Eq. (2.4). Wind shear with height can generate turbulence because of the stress that occurs between layers of different wind velocities.

Pasquill stability classes

A widely used theory to classify atmospheric stability, are the classes developed by Pasquill and Gifford, and improved by Turner. This classification, given in Table 2.1 is often called the Pasquill-Gifford-Turner (PGT) classification, that is originally based on wind speed, cloud cover and solar radiation. Most dispersion models need a measure of the stability in order to calculate the dispersion parameters. It has therefore been developed several schemes that tries to match different, more readily available, meteorological parameters to the PGT classes.The original range of classes were from A-F, but an additional class, G, has later been added to cover extremely stable conditions.[Mohan and Siddiqui, 1998].

PGT stability class	**Description**
A	Extremely unstable
B	Moderately unstable
C	Slightly unstable
D	Neutral
E	Slightly stable
F	Moderately stable
G	Extremely stable

Table 2.1: The table describes the Pasquill-Gifford-Turner stability classes.

The Richardson numbers

To help determine the stability of the atmosphere, the Richardson numbers are introduced. These dimensionless numbers gives the ratio between buoyant and shear production of TKE. The *flux* Richardson number, Ri_f, is simply the ratio between

the buoyancy term and the mechanical term in Eq. (2.4). For a horizontally homogeneous flow, Ri_f is given as

$$Ri_f = \frac{\frac{g}{\overline{\theta_v}}\overline{w'\theta'_v}}{\overline{u'w'}\frac{\partial \overline{U}}{\partial z} + \overline{v'w'}\frac{\partial \overline{V}}{\partial z}} \tag{2.6}$$

$\overline{U}$ and $\overline{V}$ are the mean wind speeds in the x- and y-direction, respectively. Because of its dependence on turbulent fluxes, Ri_f is only valid in turbulent flows. To overcome this problem, we use the same assumption as in K theory, that the turbulent fluxes are proportional to the vertical gradients. This gives the *gradient* Richardson number

$$Ri = \frac{\frac{g}{\overline{\theta_v}}\frac{\partial \overline{\theta'_v}}{\partial z}}{\left(\frac{\partial \overline{u}}{\partial z}\right)^2 + \left(\frac{\partial \overline{v}}{\partial z}\right)^2} \tag{2.7}$$

Standard meteorological observations rarely gives a good measure of the vertical gradients. Therfore, the *bulk* Richardson number, Ri_b is often used.

$$Ri_b = \frac{g\Delta\overline{\theta_v}\Delta z}{\overline{\theta_v}\left[(\Delta\overline{U})^2 + (\Delta\overline{V})^2\right]} \tag{2.8}$$

Here, the gradients are approximated by finite differences across a layer, $\Delta z = z_{top} - z_{bottom}$. When Δz becomes small, Ri_b approaches Ri. Throughout this study it is assumed that $Ri_b \approx Ri$.

The Richardson number is one of the parameters that has been used to classify conditions into the PGT stability classes in Table 2.1. In Table 2.2, limits for stability classification based on the Richardson number, as described by Mohan and Siddiqui [1998] are given.

PGT stability class	**Richarson number limits**
A	$Ri < -5.34$
B	$-5.34 \leq Ri < -2.26$
C	$-2.26 \leq Ri < -0.569$
D	$-0.569 \leq Ri < 0.083$
E	$0.083 \leq Ri < 0.196$
F	$0.196 \leq Ri < 0.49$
G	$Ri \geq 0.49$

Table 2.2: Stability classification limits for the Richardson number, as given in Mohan and Siddiqui [1998]. The limits are based on a roughness length of $z_0 = 0.1$.

Virtual potential temperature

In Eq. (2.7)-(2.8), the virtual potential temperature is used. This is the potential temperature of a dry air parcel if it had the same density as the moist air. Because we lack info about the air humidity in the area of interest for this thesis, it is assumed that $\theta_v \approx \theta$. With the cold temperatures in Oslo at wintertime, this is a reasonable assumption.

2.1.3 Similarity theory

As mentioned in Section 2.1.1, similarity theory provides 0th order closure of the equations of motion. Observational data together with dimensional analysis is used to find universal scaling sizes for the needed variables, such as horizontal and vertical wind speed, heat and moisture. These scaling sizes have proven to be useful for determining the dispersion parameters in Gaussian dispersion models, and can also be used to express the eddy diffusivities in K theory. The parts of the PBL in Fig. 2.1 have different scaling sizes. Therfore, separate similarity theories have been developed for different parts of the PBL. The theory that is most used to describe the constant-flux surface layer is the Monin-Obukhov similarity theory (MOST) [Monin and Obukhov, 1954]. This theory assumes that the gradients and turbulence depend on four parameters, namely

$$\underbrace{\frac{\tau_s}{\rho} = \overline{u'w'} + \overline{v'w'}}_{\text{Kinematic surface stress}} \qquad \underbrace{\overline{w'\theta'} = \frac{H_s}{\rho c_p}}_{\text{Kinematic heat flux}} \qquad \underbrace{\frac{g}{\overline{\theta}}}_{\text{Buoyancy variable}} \qquad \underbrace{z}_{\text{Height above ground}}$$

τ_s is the surface stress,ρ is the air density, H_s is turbulent surface heat flux and c_p the specific heat capacity of air. g is the gravitational acceleration. In addition to the height, z, the following scaling variables are:
The friction velocity

$$u_* = \left[\overline{u'w'}^2 + \overline{v'w'}^2\right]^{1/4} = \left|\frac{\tau_s}{\rho}\right|^{1/2} \tag{2.9}$$

the friction temperature

$$\theta_* = -\frac{\overline{w'\theta'}}{u_*} = -\frac{H_s}{\rho c_p u_*} \tag{2.10}$$

and the Monin Obukhov length scale (MO length),

$$L = -\frac{T_0 u_*^3}{gk(\overline{w'\theta'})} = \frac{u_*^2}{(g/T_0)\theta_*} \tag{2.11}$$

k is the empirical von Karman constant with a value of approximately 0.4. The absolute value of the MO length defines the depth of the layer where mechanical shear is significant, regardless of the stability conditions. At heights above L, the buoyancy term is dominating the vertical transport. L is positive (negative) when $\overline{w'\theta'}$ is negative (positive), indicating stable (unstable) conditions. In neutral conditions, when $\overline{w'\theta'}$ is close to zero, L approaches infinity. Because the MO length gives information of the stability of the atmosphere, a stability classification scheme relating MO length, surface roughness and the Pasquill classes was developed by Golder [1972]. The relationship is illustrated in Fig. 2.2. The roughness length, z_0 is more closely explained further down in the text.

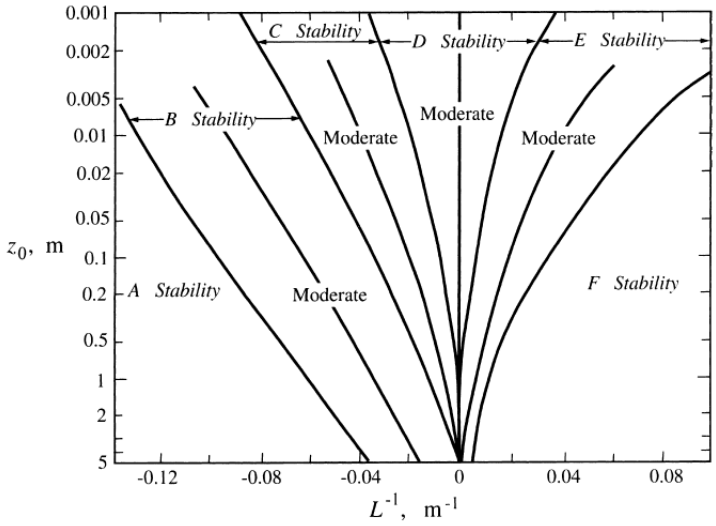

Figure 2.2: The relationship between MO length, surface roughness length and Pasquill stability classes based on Golder [1972]. Adopted from Seinfeld and Pandis [2016].

From L we can define the stability parameter

$$\zeta = \frac{z}{L} \tag{2.12}$$

Similarity Relations

Dimensionless wind and temperature gradients are defined by using the variables presented above as

$$\left(\frac{kz}{u_*}\right)\left(\frac{\partial \bar{u}}{\partial z}\right) = \phi_m(\zeta) \tag{2.13}$$

$$\left(\frac{kz}{\theta_*}\right)\left(\frac{\partial \bar{\theta}}{\partial z}\right) = \phi_h(\zeta) \tag{2.14}$$

where $\phi_m(\zeta)$ and $\phi_h(\zeta)$ are the MO similarity relations for momentum and heat, respectively. In this thesis, the similarity relation for heat will not be used, so further description of this will be omitted. In neutral cases, $\phi_M = 1$, and the wind profile is close to logarithmic. For non-neutral conditions, the effects of the stability conditions will alter the logaritmic wind profile. The most used similarity relations are the empirically determined Businger-Dyer relations [Businger et al., 1971, Dyer, 1974], given in Eq. (2.15).

$$\phi_m = \begin{cases} 1 + 4.7\zeta & \text{for } \zeta > 0 \text{ stable} \\ 1 & \text{for } \zeta = 0 \text{ neutral} \\ (1 - 15\zeta)^{-1/4} & \text{for } \zeta < 0 \text{ unstable} \end{cases} \tag{2.15}$$

If Eq. (2.13) is integrated from z_0 to z, we find a function for wind velocity with height,

$$\frac{\bar{u}(z)}{u_*} = \frac{1}{k}\left(ln\left(\frac{z}{z_0}\right) - \Psi_m(\zeta)\right) \tag{2.16}$$

The Ψ_m function is on the form

$$\Psi_m(\zeta) = \int_{z_0/L}^{z/L} [1 - \phi_m(\zeta)] \frac{d\zeta}{\zeta} \tag{2.17}$$

Following Businger-Dyer, we can express it as

$$\Psi_m(\zeta) = -\frac{5z}{L} \qquad \text{stable} \tag{2.18}$$

$$\Psi_m(\zeta) = 2ln\left(\frac{1+x}{2}\right) + ln\left(\frac{1+x^2}{2}\right) - 2tan^{-1}x + \frac{\pi}{2} \qquad \text{unstable} \tag{2.19}$$

where $x = (1 - 15\frac{z}{L})^{1/4}$.

The relationship between ζ and Richardson number

$\overline{w'\theta'}$ and u_* are rarely measured directly, which makes calculation of L directly from Eq. (2.11) difficult. L is often used to determine the spread of a plume in dispersion calculations, and it is therefore desirable to find it in an alternative way. One way of estimating the MO length with only wind and temperature observations is by its connection to the Richardson number, $Ri = Ri(\zeta) = Ri(z/L)$. According to MOST, the Richardson number can be expressed by the similarity relations as

$$Ri = \zeta \frac{\phi_h(\zeta)}{\phi_m^2(\zeta)} \tag{2.20}$$

Businger et al. [1971] found that the relationship between Ri and ζ follows the trend in Fig. 2.3.

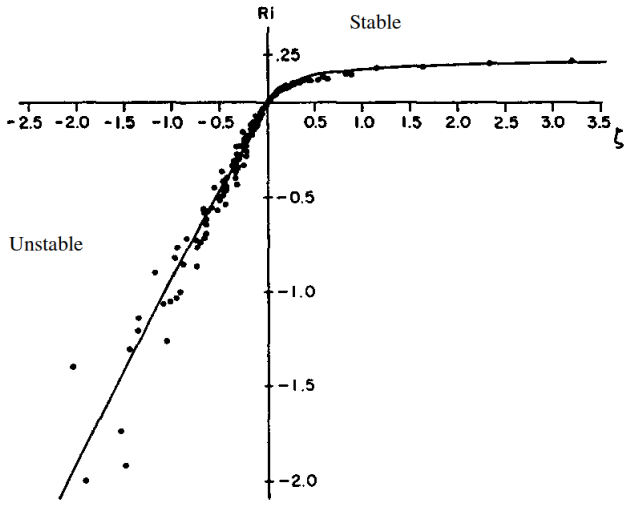

Figure 2.3: The Richardson number as a function of ζ. The dots represent observed values, and the line is the best fit function to these values. Adapted from Businger et al. [1971].

The functions best fitted to the observations in Fig. 2.3 are given in Eq. (2.21).

$$Ri \approx \begin{cases} \zeta & \text{unstable} \\ \frac{\zeta(0.74+4.7\zeta)}{(1+4.7\zeta)^2} & \text{stable} \end{cases} \tag{2.21}$$

As is evident from Fig. 2.3, the $Ri(\zeta)$ function is asymptotic for the stable case, and the Richardson number has a critical value around $Ri = 0.2$. This cause a problem when using the equation 'backwards' to find $\zeta = \zeta(Ri)$, as is done in this thesis. Richardson numbers calculated from observations in stable conditions can exceed 0.2, which make it impossible to find a value for ζ from Eq. (2.21). Delage [1997] presented several alternative formulations for the relationship, where there is no critical value for Ri. One of these formulations are the Modified Louis formulation, based on the work by Louis [1979]. In this formulation, the height dependence of the turbulent fluxes is considered to be non-negligible, as opposed to MOST.

Now, the similarity functions are related to the Richardson number through

$$\phi_m = \phi_h = 1 + \alpha Ri \tag{2.22}$$

with $\alpha = 12$. The wind profile follow Eq. (2.16) as before, but the Ψ functions are given as

$$\Psi_m = \Psi_h = \Psi = \frac{1}{2}\left[A - \frac{z}{h} - ln\left(1 + \frac{Bz}{2}\right) - \frac{B}{2\sqrt{C}} sin^{-1}\left(\frac{B - 2Cz}{D}\right)\right] \tag{2.23}$$

with

$$A = \sqrt{1 + Bz - Cz^2} \qquad B = D - \frac{2}{h}$$
$$C = \frac{D}{h} - \frac{1}{h^2} \qquad D = \frac{4\alpha}{L}$$

Notice how the function is dependent on the boundary layer height, h. To ensure that C is positive there is a restriction demanding that $h > L/4\alpha$. In this thesis the Businger-Dyer relationships will be used for calculating L and u_* in unstable conditions, while the Modified Louis formulation will be used for stable cases.

The Deardorff velocity scale

In convective situations, the shear determined friction velocity, u_*, may not be the best scale for the velocity. In convective conditions, the buoyant forces dominates over the shear forces, also close to the surface. The Deardorff velocity, also called the convective velocity is a better scaling size for velocity in this case. It is defined as

$$w_* = \left(\frac{g}{\overline{\theta_v}} z_i \overline{w'\theta'}\right)^{1/3} \tag{2.24}$$

Where $\overline{\theta_v}$ is the mean virtual temperature and z_i the mixed layer depth.

Surface Roughness Length

The surface roughness length is defined as the height above the ground where the wind speed becomes zero when following the logarithmic wind profile for neutral conditions. This height is determined by the size and amount of surface roughness elements, however, it is always lower than the disturbing elements. Often, z_0 is estimated by using a wind speed profile, but if this is not available, other methods have been developed. Kondo and Yamazawa [1986] proposed to sum up the N different roughness elements in area A_{tot}. The expression is

$$z_0 = \frac{0.25}{A_{tot}} \sum_{i=1}^{N} h_i s_i \tag{2.25}$$

with h_i and s_i as the height and surface area of element i, respectively.

2.1.4 PBL Heights

The PBL height is often defined as the middle of the of the inversion layer. Radiosonde observations can be used to determine the vertical profiles of for example temperature or humidity, which in turn can be used to determine the inversion height. Fig. 2.4 show typical vertical profiles of different variables. The sudden change in potential and absolute temperature is clearly seen for both the entrainment zone in daytime and for the capping inversion at night. Without data from radiosonde/lidar measurements the PBL height is challenging to estimate. The height changes with a number of dynamical and thermodynamical properties, in addition to time and location.

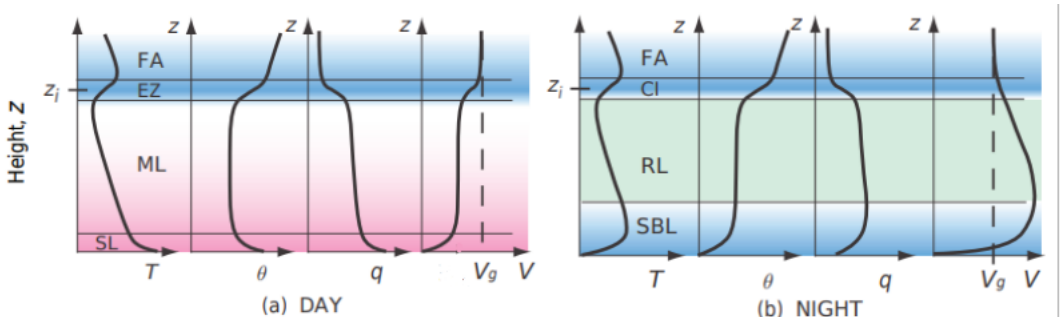

Figure 2.4: Typical vertical profiles for temperature T, potential temperature θ, specific humidity, q and wind speed, V, from the surface up to the free atmosphere (FA). V_g represent the geostrophic wind. z_i marks the height of the PBL, located in the entrainment zone (EZ) in daytime, and in the capping inversion (CI) at night. The mixed layer (ML) and surface layer (SL) are shown for daytime and for the nocturnal stable boundary layer (SBL) and residual layer (RL). Adapted from Wallace and Hobbs [2006]

Because the top of the PBL work as a lid that traps pollutants underneath it, knowledge of this height is important for dispersion calculations. A number of methods for estimating the PBL height from simpler meteorological observations

have been suggested. One of the most used relationships for stable conditions were proposed by Zilitinkevich [1972],

$$h \propto \left(\frac{Lu_*}{f}\right)^{1/2} \tag{2.26}$$

L is the Monin Obukhov length, u_* is the friction velocity and f is the Coriolis parameter.

Venkatram [1980] derived an empirical relationship between L and u_* based on data sets from several experiments. This relationship is $L = Au_*^2$, where A is an empirically determined constant. By combining this with Eq. (2.26), Venkatram found that $h \propto u_*^{3/2} f^{-1/2}$ and

$$h = 2400 u_*^{3/2} \tag{2.27}$$

It should be noted that even though these relationships are regarded as sufficient to use for dispersion calculations, the values are still highly uncertain and should be treated with caution.

2.1.5 Urban meteorology

The theory described above are largely based on ideal situations, and the empirical relationships are found based on field campaigns performed in rural environments. In an urban area like Bjørvika, the effect of the city will influence the meteorology. In this section, some of these effects will be addressed.

Surface elements, like buildings in a city, or trees in a forest can act like a displaced surface if they are placed closely together. The consequence of the displacement distance, d, is that the logarithmic wind profile is zero at height $d + z_0$ instead of at z_0. Under this height, the motions are greatly affected by local disturbances, which makes modeling and measurements very difficult, and the constant flux assumption may not hold.

The boundary layer structure over a city is also much more complex that the idealized case shown in Fig. 2.1. When air flows over areas with different surface roughness, one or more internal boundary layers may form, as illustrated in Fig. 2.5. This complicates the height profiles of meteorological parameters, which make the parameterization of surface variables in models extra challenging. It may also affect observed meteorology in an area. If, for example, the observations are made above the internal boundary layer, they may not be representative of the conditions inside the internal boundary layer.

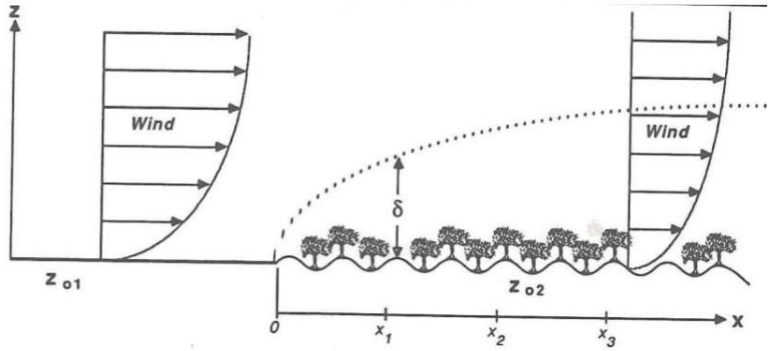

Figure 2.5: Illustration of the developement if an internal boundary layer. z_{01} and z_{02} are the upwind and downwind roughness lengths and δ represent the internal boundary layer depth. Adopted from Stull [1988].

Yet another complication of urban meteorology is the anthropogenic contribution to the energy balance. Human activities introduces an additional heat flux, which can change the energy budget significantly compared to a rural area [Fisher et al., 2006].

2.2 The Gaussian dispersion formulation

It is well known that the concentration distribution from a continuous point source can, in idealized cases, be modelled with a Gaussian function (e.g. Seinfeld and Pandis [2016], Arya [1999]). This is widely used in dispersion models, for example in RLINE and EPISODE, to simulate spread from different sources. To use the Gaussian plume equation, one must consider a stationary situation in an atmosphere with homogeneous turbulence, as mentioned in Section 2.1.1. In addition, a number of other assumptions has to be made in order for the equation to be valid [Lyons and Scott, 1990]. The emission rate and meteorological conditions must be assumed to be constant, at least for the time it takes for the pollutant to travel from the source to the receptor point.

For the criteria of conservation of mass to be satisfied, the pollutant must be assumed to be nonreactive. In addition, there can be no deposition or scavenging of the pollutant. In other words, all material that reaches the surface is assumed to be reflected back.

The concentration distribution in the plume is approximated to have a Gaussian shape, in both the vertical and cross-wind lateral direction.

Another important simplification is the slender-plume approximation, where the turbulent diffusion in the mean flow direction is neglected [Seinfeld and Pandis, 2016].

The Gaussian plume equation can be derived by using the mass conservation principle and the assumption that the concentration distributions downwind from a source are Gaussian in the vertical and lateral directions [Arya, 1999]. If we assume that the mean wind direction, $\bar{u}$ is along the x-axis, the concentration at a point

(x,y,z) downwind from a continuous point source can be written as

$$\overline{c}(x,y,z) = \frac{Q}{2\pi\overline{u}\sigma_y\sigma_z} exp\left(-\frac{y^2}{2\sigma_y^2} - \frac{z^2}{2\sigma_z^2}\right) \tag{2.28}$$

Here, Q is the emission rate, and σ_y and σ_z are dispersion parameters in the horizontal and vertical direction, respectively. These dispersion parameters are the standard deviations of the Gaussian curve, that is, they determine the spread of the plume. Usually the dispersion coefficients are expressed by similarity parameters like the ones discussed above, combined with empirically determined constants. This underlines the importance of the similarity parameters on pollution dispersion. Because the plume is parallel to the x-axis, there is no Gaussian distribution in this direction and therfore no σ_x in the equation. Fig. 2.6 shows a sketch of the plume described by Eq. (2.28).

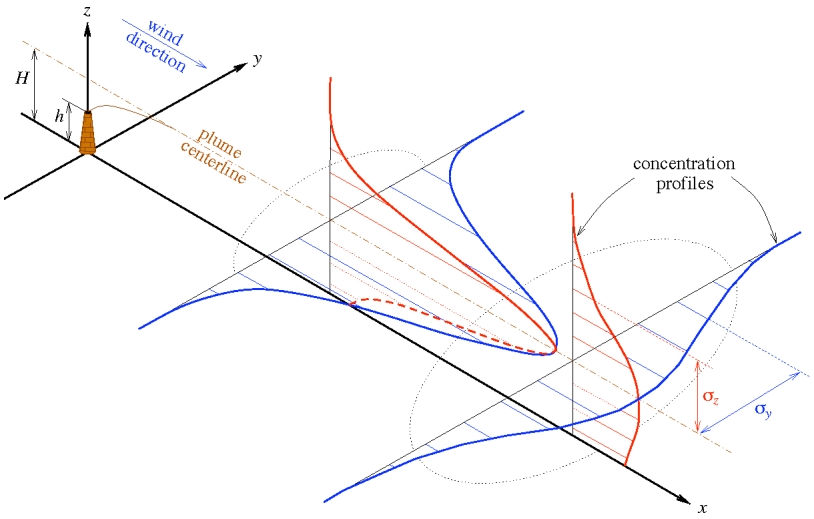

Figure 2.6: Sketch of the concentration profiles for the plume of a continous point source. H is the effective plume height, while h is the emission height. σ_z and σ_y are the dispersion parameters. Adopted from Stockie [2011].

For applications near the surface, the presence of the ground will act as a boundary condition. The second term in the exponential function in Eq. (2.28) can be altered to fit different idealized surfaces. Following Arya [1999], the case of a totally reflecting surface gives the equation

$$\overline{c}(x,y,z;H) = \frac{Q}{\overline{u}} F_y F_z \tag{2.29}$$

where F_y represent the cross-wind dispersion

$$F_y = \frac{1}{\sqrt{2\pi}\sigma_y} exp\left(-\frac{y^2}{2\sigma_y^2}\right) \tag{2.30}$$

and F_z represent the vertical dispersion

$$F_z = \frac{1}{\sqrt{2\pi}\sigma_z}\left[exp\left(-\frac{(z-H)^2}{2\sigma_z^2}\right) + exp\left(-\frac{(z+H)^2}{2\sigma_z^2}\right)\right] \tag{2.31}$$

H is the effective release height above the surface. Eq. (2.31) is found by using the method of images, in which an imaginary mirror source is introduced. This source is of equal magnitude and distance from the receptor as the original, but placed at a depth H below the surface. That way, the contribution from the image source represent the reflected part of the concentration. If longer downwind distances are examined, or in very turbulent conditions, the plume may stretch up to the top of the PBL. Hence, we also need to consider this as a reflecting boundary condition. The way to do this is to use several mirror sources that simulate reflection back and forth between the ground and the inversion lid. Then, Eq. (2.31) is replaced by

$$\begin{aligned} F_{z,mirror} = \frac{1}{\sqrt{2\pi}\sigma_z}\Big[&exp\Big(-\frac{(z-H)^2}{2\sigma_z^2}\Big) + exp\Big(-\frac{(z+H)^2}{2\sigma_z^2}\Big) \\ &+ \sum_{n=1}^{\infty} exp\Big(-\frac{(z-H-2nh)^2}{2\sigma_z^2}\Big) + exp\Big(-\frac{(z+H-2nh)^2}{2\sigma_z^2}\Big) \\ &+ exp\Big(-\frac{(z-H+2nh)^2}{2\sigma_z^2}\Big) + exp\Big(-\frac{(z+H+2nh)^2}{2\sigma_z^2}\Big)\Big] \end{aligned} \tag{2.32}$$

The method of images is more closely described in Arya [1999], p139-140.

The stability of the PBL is greatly affecting the dispersion parameters, which in turn determines the shape of the plume. In Fig. 2.7, the plumes reaction to different stability conditions is demonstrated. One can think of going from left to right in the figure, as going from PGT stability class G-A (see Table 2.1). It is clear that in stable conditions, the plume is trapped closer to the ground, which will yield higher concentrations in the lower part of the atmosphere. In unstable cases, the plume tend to loop up and down over a large vertical range, causing more vertical mixing, leading to lower concentrations near ground.

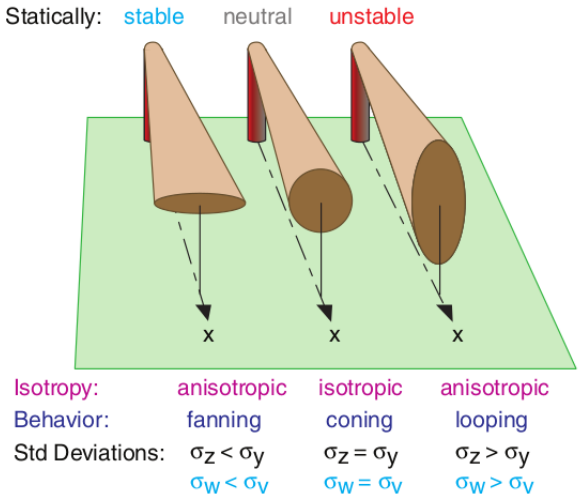

Figure 2.7: Dispersion from a continuous point source in different stability conditions. Adopted from Stull [2012]

2.2.1 Line source approximation

The case of a continuous point source can be the building block of several other types of sources, like line, area and volume sources. If we treat a line source as a sum infinitesimal point sources, the contribution from the whole line source can be found by numerical integration of the point sources. A problem with this approach is that the Gaussian formulation is only strictly valid when the wind direction is perpendicular to the road. When assuming that the direction is perpendicular for all the infinitesimal point sources, this introduces errors in the line source calculation, especially when the real wind is close to parallel to the road [Venkatram and Horst, 2006].

2.3 NO_2 as a pollutant

Although dispersion of a variety of pollutants are important in an urban area, we have in this study chosen to look at NO_2. Following is a short introduction of the gas and the challenges connected to its emissions.

2.3.1 Chemistry

The two species of nitrogen oxides, NO_2 and NO are both regarded as important air pollutants in the lower atmosphere. Due to the rapid cycling between them, it is common to refer to them combined, as NO_X.

NO_X in the PBL are mainly a result of anthropogenic emissions. Other sources are (de)nitrification in soils and oxidation of ammonia from the biosphere. Transport from the stratosphere is a minor contributor. At high temperatures, NO is produced from O_2 and N_2 in the air via the reactions R1-R3. Such high temperatures occurs naturally in lightnings, but more importantly for us, in combustion processes, like engines and biomass burning.

$$O_2 \xrightarrow{\text{heat}} O + O \tag{R1}$$

$$O + N_2 \longrightarrow NO + N \tag{R2}$$

$$N + O_2 \longrightarrow NO + O \tag{R3}$$

The conversion between NO_2 and NO happens through the null cycle, R4-R5. The time scale of this cycling is about one minute[Jacob, 1999].

$$NO + O_3 \longrightarrow NO_2 + O_2 \tag{R4}$$

$$NO_2 + h\nu \xrightarrow{O_2} NO + O_3 \tag{R5}$$

The term $h\nu$ is the photon energy from solar radiation, so reaction R5 is not happening at night. Thus, NO_2 will be produced at the expense of NO, presumed that there are enough O_3 to drive the reaction. The main sink of NO_X in the troposphere is oxidation to nitric acid, HNO_3. Nitric acid is highly soluble in water, and is usually scavenged by precipitation. It can also be absorbed by land or water

surface, i.e. dry deposited [Badr and Probert, 1993]. The typical lifetime before NO_X is oxidized is one day [Jacob, 1999]. Because of the rapid cycling, one can use NO_2 as a proxy for the whole NO_X family. However, the ratio between NO_2 and NO has been shown to vary significantly [Kimbrough et al., 2017]. This fact introduces a source of error in this study, where only NO_2 is measured.

2.3.2 Pollution and regulations

Studies indicate that exposure to NO_X have negative health effects on humans [Latza et al., 2009, Samoli et al., 2006].

Fig. 2.8 shows the percentage distribution of NO_X emissions from anthropogenic sources in Norway for the year 2016. The largest contribution comes from oil and gas extraction, but coastal navigation and road traffic are also significant contributors. In urban areas emissions from road traffic are the main concern. The total amount of pollution contributes to an ambient background concentration of NO_X. Close to a road the total exposure will be the sum of the background concentration and the emissions from the road. Background concentrations are generally higher in urban than in rural areas, and this needs to be considered when using models to estimate concentrations.

The emission rate from roads depends on the traffic volume and the composition of vehicles on the road. Vehicles running on diesel emit more NO_X than those running on petrol, and heavy vehicles emit more than light vehicles. Estimation of the vehicle fleet, and the emission rates from different vehicles are challenging, and this also introduces uncertainties in dispersion calculations.

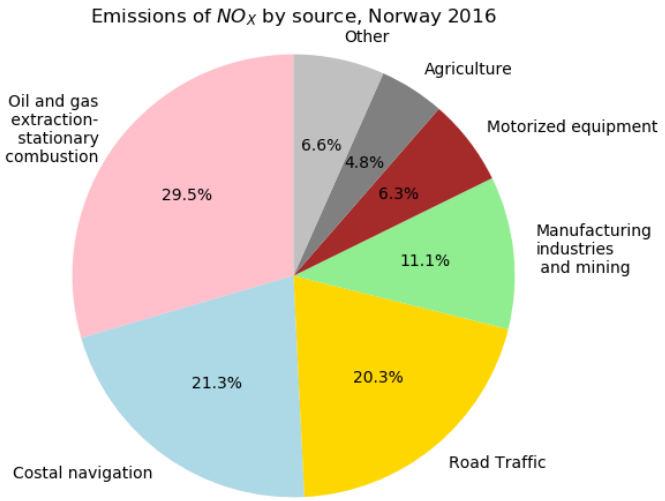

Figure 2.8: Percentage distribution of NO_X emissions to air from different anthropogenic sources. The data are collected from Statistisk Sentralbyrå (`https://www.ssb.no/en/natur-og-miljo/statistikker/agassn/aar-endelige`).

Because of the harmful effect on human health and the environment, it is important to limit the exposure to NO_X. According to Norwegian law there are limit values

for hourly and yearly mean concentration values of NO_X/NO_2. An overview over the limit values are given in Table 2.3.

Description	**Averaging period**	**Limit value**
Hourly limit value for protection of human health	1 hour	$200\mu g/m^3$ NO_2*
Yearly limit value for protection of human health	Calendar year	$40\mu g/m^3$ NO_2
Limit value for protection of vegetation (NO_X)	Calendar year	$30\mu g/m^3$ NO_X

Table 2.3: Excerpt from the table in Forurensningsforskriften §7-6 (`https://lovdata.no/forskrift/2004-06-01-931`). *This value can not be exeeded more than 18 times per year.

2.4 Air pollution dispersion models

Because of the great interest in modeling dispersion of different types of pollution, many models have been developed over the years. The majority uses the Gaussian plume formulation described in Section 2.2 to simulate dispersion from road traffic. For more general dispersion calculations, numerical solution of the advection/diffusion equation is often used. Based on meteorological and emission input data, the models can calculate concentration contributions from one or several sources.

2.4.1 RLINE

The Research LINE source model, RLINE, is a model developed for estimation of dispersion of pollutants from line sources near the surface [Snyder et al., 2013]. Although it is a relatively new and simple model, it has been shown to perform on the same level as more advanced models[Heist et al., 2013]. Each line source is regarded as the integral over a series of point sources, where the contribution from each source is calculated with the Gaussian Plume formulation, as described in Section 2.2. The integral is then solved numerically with Romberg integration to obtain the concentration at a receptor point [Press, 2007]. The configuration of both the receptors and the line sources are completely userdefined.

In the model we assume that the pollutants in question are primary and inert. Strictly, this is not true for NO_2, but as presented in Section 2.3, the transition between NO and NO_2 is rapid. In this study it is therefore assumed that all NO_X is present as NO_2. It is also assumed that the transport time from the source to the receptors are much smaller than the life time of NO_X of about one day, so that NO_X can be treated as an inert gas.

Meteorology

In addition to wind speed and direction, RLINE uses similarity scaling parameters, as discussed in Section 2.1.3, to determine the dispersion.

The effective wind speed that is used in the dispersion calculations are given as

$$U_e = \sqrt{\sigma_u^2 + \sigma_v^2 + U(\overline{z})^2} \tag{2.33}$$

where σ_u and σ_v represent wind variances in the eastward and northward direction, respectively. $U(\overline{z})$ is the wind speed at mean plume height. At low wind speeds it is assumed that $\sigma_u \simeq \sigma_v$, so that $\sigma_u^2 + \sigma_v^2 \simeq 2\sigma_v^2$. The expression for σ_v is taken from Cimorelli et al. [2005] as

$$\sigma_v = \sqrt{(0.6w_*)^2 + (1.9u_*)^2} \tag{2.34}$$

As is evident from Eq. (2.33), the effective wind speed will approach $\sqrt{2}\sigma_v$ when $U(\overline{z})$ becomes small. A minimum effective wind speed $U_{e,min} = \sqrt{2}\sigma_v \neq 0$ is necessary to avoid division by zero in the Gaussian plume formulation.

Line source approximation

The line source is placed along the Y axis in an (X,Y,Z)-coordinate system. The wind direction is given in an angle θ relative to the X-axis. To calculate the concentration at a receptor point, a rotated coordinate system, (x,y,z), is used, where the x-axis is parallel to the wind direction, and z=Z. A representation of the coordinate systems are given in Fig. 2.9.

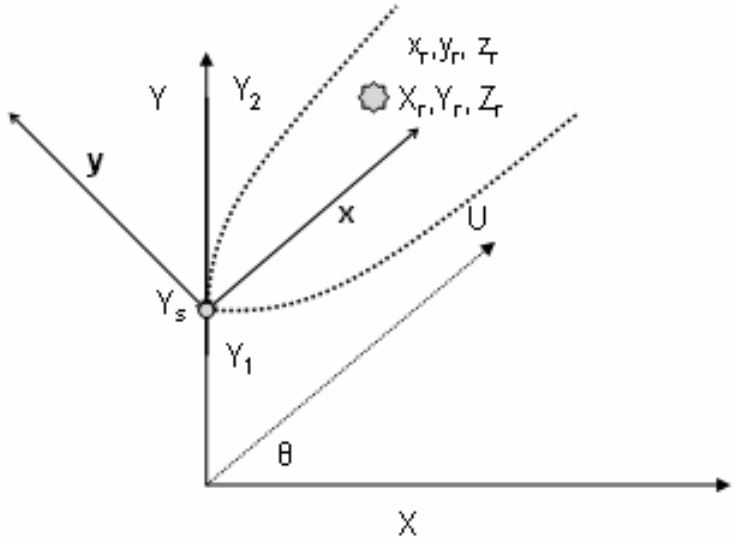

Figure 2.9: The figure shows the (X,Y,Z)-coordinate system with a line source from Y1 to Y2. Ys is a random point source and the star represents a receptor at $(x_r, y_r, z_r)/(X_r, Y_r, Z_r)$. The rotated (x,y,z)-system with the x-axis along the wind direction is used for concentration calculations in RLINE. The dotted lines represents the extent of the plume. Adapted from Snyder et al. [2013].

The concentration at a point (x_r, y_r) from a source that starts at Y1 and ends at Y2 is given by

$$C(x_r, y_r) = \int_{Y1}^{Y2} dC_{total} = \int_{Y1}^{Y2} (1-f)dC_{plume} + fdC_{meander} \tag{2.35}$$

The contribution from an elemental point source, dC_{total}, is divided into two parts, one plume component, dC_{plume}, and one meandering component, $dC_{meander}$. The meandering part is added to the model formulation to account for the random component of the wind, which will have most effect at low wind speeds. A weighting factor, $f = (2\sigma_v^2)/U_e^2$ is used to determine the relative importance of each component based on the magnitude of the wind and the lateral turbulence. The contributions are on the form

$$dC_i = \frac{qdY_s}{U_e}[VERT \times HORZ_i] \tag{2.36}$$

with emission rate, q, in units $[gs^{-1}m^{-1}]$. i represent the *plume* and *meander* parts. For both components, VERT is the vertical part of the Gaussian plume equation, (2.31). The plume component describes a regular Gaussian distribution, while the meandering part is expressed as

$$HORZ_{meander} = \frac{1}{2\pi R} \tag{2.37}$$

where R is the distance from the source point to the receptor point. In relatively strong winds, when $f \to 0$, the horizontal spread mainly follows the Gaussian plume distribution in Eq. (2.30). In light winds, when $f \to 1$, the meandering term dominates, and the horizontal spread is equal in all directions, even upwind from the source.

The plume dispersion parameters, σ_y and σ_z are calculated using expressions derived by Venkatram et al. [2013]. The equations for the vertical spread are based on a solution of the eddy diffusivity using the mass conservation equation. For the vertical parameter we have

$$\sigma_z = a\frac{u_*}{U_e}x\frac{1}{\left(1 + b_s\frac{u_*}{U_e}\left[\frac{x}{L}\right]^{2/3}\right)} \tag{2.38}$$

for stable cases, and

$$\sigma_z = a\frac{u_*}{U_e}x\left(1 + b_u\frac{u_*}{U_e}\frac{x}{L}\right) \tag{2.39}$$

for unstable cases. a, b_s and b_u are dimensionless, empirical constants with the values 0.57, 3 and 1.5, respectively. For the horizontal spread, the equations are

$$\sigma_y = c\frac{\sigma_v}{u_*}\sigma_z\left(1 + d_s\frac{\sigma_z}{|L|}\right) \tag{2.40}$$

for stable conditions, and

$$\sigma_y = c\frac{\sigma_v}{u_*}\sigma_z\left(1 + d_s\frac{\sigma_z}{|L|}\right)^{-1/2} \tag{2.41}$$

the empirical coefficients are here c=1.6, d_s=2.5 and d_u=1.0. In neutral conditions, when L is large, the two equations approach the same limit. Eq. (2.38)-(2.41) show that the parameters derived from similarity theory in Section 2.1.3, L, u_* and w_* (w_* is implicit in the expression for U_e) are essential for determining the shape of the Gaussian plume used to estimate the dispersion.

An initial vertical dispersion, σ_{z0}, caused by the vehicle induced turbulence is added to the vertical parameters.

2.4.2 EPISODE

The air pollution dispersion model EPISODE was developed by NILU. EPISODE is built as a Eulerian 3D grid model, with embedded subgrid models for point, line and area sources. The theory presented in this section is based on the technical description by Slørdal et al. [2003]. Some features have been changed since this description was released, and the added theory is provided by Gabriela Sousa Santos at NILU.

Meteorology

To run EPISODE, information about wind speed and direction, temperature and surface roughness are required. Cloud cover, relative humidity and precipitation data are optional input. All input can be based on either observations or modeled data.

If the meteorlogical input is based on observations, the MOST based Meteorological Preprocessor for Dispersion Modelling (MEPDIM) [Bøhler, 1996], is used to parameterize the relevant surface parameters. MEPDIM uses the profile method [Van Ulden et al., 1985] to parameterize the surface momentum flux, τ_s, the surface sensible heat flux, H_s, and the MO length, L.

The calculation of mixing height is determined by the stability conditions. For stable and neutral conditions, the mixing height is determined diagnostically by using the theory of Nieuwstadt [1984]. For unstable conditions, a differential equation derived by Batchvarova and Gryning [1991] is used.

If the meteorological input is based on modeled data, like from WRF, the surface parameters can be taken directly from this input.

Eulerian grid model

The main equation to be solved is the advection-diffusion equation,

$$\begin{aligned} &\frac{\partial c_i}{\partial t} + \frac{\partial}{\partial x}(uc_i) + \frac{\partial}{\partial y}(vc_i) + \frac{\partial}{\partial z}(wc_i) = \\ &\frac{\partial}{\partial x}\left(K_H \frac{\partial c_i}{\partial x}\right) + \frac{\partial}{\partial y}\left(K_H \frac{\partial c_i}{\partial y}\right) + \frac{\partial}{\partial z}\left(K_Z \frac{\partial c_i}{\partial z}\right) + R_i - S_i \end{aligned} \tag{2.42}$$

c_i is the mass concentration of species i. u, v, w represents the components of the wind vector, and R_i and S_i represent the sources and sinks of species i. The three first terms on the right hand side represent the turbulent diffusion, and is represented

by K-theory, so K_H and K_Z are the eddy diffusivities in the horizontal and vertical direction, respectively. It is assumed that the atmosphere is incompressible, i.e.

$$\frac{\partial u}{\partial x} + \frac{\partial v}{\partial y} + \frac{\partial w}{\partial z} = 0 \tag{2.43}$$

The vertical eddy diffusivity is defined as

$$K_Z = K^* + K_0(u_*, \Delta z_1) \tag{2.44}$$

Here, the first term is a standard parameterization based on stability conditions.

$$K^* = \begin{cases} ku_* z exp(-\frac{8fz}{u_*}) & \text{unstable and neutral conditions} \\ \frac{ku_* z}{0.74+4.7(z/L)} exp(-\frac{8fz}{u_*}) & \text{stable conditions} \end{cases} \tag{2.45}$$

Eq. (2.45) show that the vertical diffusivity is dependent on the surface friction velocity, and the stability, via L. In stable, low wind conditions, K^* has been found to give unrealistically low values. The empirical term $K_0(u_*, \Delta z_1)$ is introduced to reduce this problem.

The horizontal eddy diffusivity is calculated as a function of the horizontal grid resolution and turbulence intensity, σ_v. For grid cell (i,j,k) this is

$$K_H(k) = 0.1\text{min}(\Delta x, \Delta y) \times \text{max}_{i,j}\sigma_v(i,j,k) \tag{2.46}$$

Because K_H is a function of the grid resolution, the length scale of turbulence is proportional to the grid size.

Chemistry

The model is using an assumption of instantaneous equilibrium between the chemical reactions in the null cycle (R4-R5 in Section 2.3). Then, one assumes that the concentration of NO_X, as well as O_X=O_3+NO_2 is conserved. This way the concentrations of NO_X, NO and O_3 can be found by solving a quadratic equation for O_3, and use this in the NO_X and O_X equations. The model does not take wet and dry deposition into account.

The subgrid line source model

Similar to RLINE, the subgrid line source model is based on a steady-state integrated Gaussian plume model. The line source configuration is shown in Fig. 2.10. Each source is divided into two lanes, and the contribution at a receptor point is the sum of the two lanes. The wind velocity that is used in the Gaussian equation is taken from the lowermost grid box covering the center of the line source, point (X_0, Y_0, Z_0) in Fig. 2.10. The emission height is set to 1m for all line sources. Each line source has an influence zone, typically 500m. The contribution from a line source will only affect receptor points that lies within its influence zone.

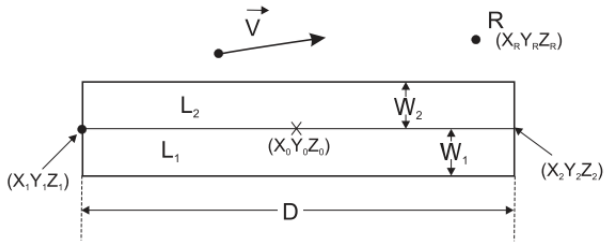

Figure 2.10: Representation of a line source with length D. Each line source is divided into two lanes, L_1 and L_2, with lane width W_1 and W_2. Point (X_0, Y_0, Z_0) marks the center of the line source. Adapted from Slørdal et al. [2003]

The concentration contribution to a point (x_r, y_r) from a lane i that starts at 0 and ends at D is given by

$$C(x_r, y_r) = \frac{q_i}{u} \int_0^D f dL \tag{2.47}$$

Here, q_i is the emission intensity of species i from the line source, u is wind speed, and f is a point source dispersion function with units $[m^{-2}]$. This dispersion function is defined in different ways, depending on the stability conditions. The stability is determined by a critical MO length, $L_{crit} = \frac{u_*}{4|f_{Cor}|}$, where f_{Cor} is the Coriolis parameter. If $|L|$ is larger than L_{crit}, the conditions are said to be neutral. If not, the stability is determined by the sign of L (positive=stable, negative=unstable). If the vertical dispersion parameter, σ_z is larger than $1.6h_{mix}$, the vertical dispersion is considered to be uniform with height, hence the dispersion function is independent of z. The different forms of f are listed below.

$$\begin{aligned}
&\text{Stable} && : \quad f = F_y F_z \\
&\text{Neutral/Unstable,} \quad \sigma_z < 1.6h_{mix} && : \quad f = F_y F_{z,mirror} \\
&\text{Neutral/Unstable,} \quad \sigma_z > 1.6h_{mix} && : \quad f = F_y \frac{1}{h_{mix}}
\end{aligned}$$

F_y, F_z, F_{mirror} are defined by Eq. (2.30), (2.31), (2.32), respectively.

The dispersion parameters, σ_y and σ_z are the sum of the ambient and initial spread. The initial spread is set to constant values of $\sigma_{y0} = 3m$ and $\sigma_{z0} = 1.5m$. The ambient, horizontal parameter is given as

$$\begin{aligned}
\sigma_{ya} &= \frac{1000x}{2.15 tan\theta_p} \\
\theta_p &= c - d \cdot ln(x/x_0)
\end{aligned} \tag{2.48}$$

where x is the downwind distance to the source, x_0 is a normalizing distance set to 1000km, and θ_p is the half angle of horizontal plume spread. c and d are stability determined constants. The ambient vertical dispersion is determined by a power law,

$$\sigma_{za} = ax^b \tag{2.49}$$

where a and b are stability determined constants.

The total concentration for a receptor point is calculated as the sum of the Eulerian grid concentration in the lowermost layer covering the receptor point, and the contributions from the line sources that lies within the influence zone of the receptor point. The Eulerian grid concentration is modified to avoid that contributions from the line sources are counted twice.

2.4.3 Main differences of the models

Some key differences between EPISODE and RLINE are briefly adressed here. While RLINE is a simple line source model only, EPISODE is actually a grid model, with an integrated line source model. The meteorology in EPISODE is therefore represented as a field, rather than just hourly values, like in RLINE. The Eulerian model is time dependent, so the history will affect the resulting concentrations. RLINE is independent of time, which mean that the concentrations are only determined diagnostically. EPISODE takes hourly measured background concentrations as input, while RLINE does not consider background at all.

The dispersion parameters for the Gaussian line source approximation are defined differently in the two models. In EPISODE, the surface parameters are not directly used in the equations (Eq. (2.48)-(2.49)), whereas in RLINE, both L, u_* and w_* affect the spread directly. However, the vertical, turbulent diffusion in the Eulerian model in EPISODE are directly dependent on u_* and L. Another difference is the treatment of chemistry. In RLINE, we assume that all NO_X are present as NO_2, while EPISODE assumes instant equilibrium between the reactions in the null cycle. However, in winter time with cold temperatures, the assumption of an instantaneous equilibrium is close to $NO_X \approx NO_2$.

2.5 The theory of passive samplers

To compare the model results with observational data, passive samplers, sometimes called diffusive samplers, were used. These are small, low cost, and easy-to-use samplers, based on the principle of molecular diffusion. Gas molecules from the ambient air diffuses into the sampler, which means that no mechanics or electricity is needed. A sketch of the type of sampler used in this study is given in Fig. 2.11. Ambient air enters through a metal prefilter, which reduces the turbulent transport. After passing the prefilter, the air is transported solely via molecular diffusion towards an impregnated filter, which adsorbs the gas of interest, in our case NO_2.

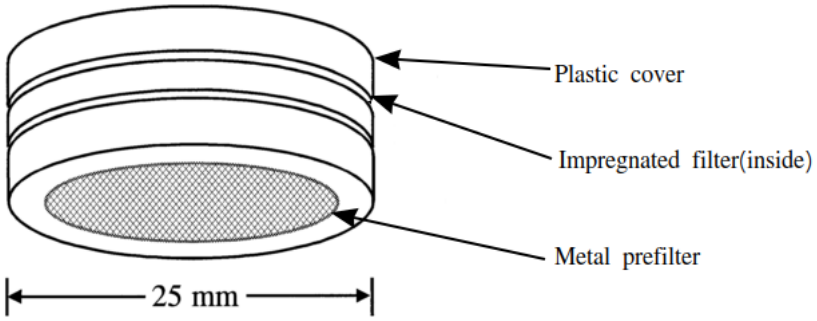

Figure 2.11: The figure shows a passive sampler. Adapted from [Ferm and Rohde, 1997]

A sampling period is typically between 1-4 weeks. Afterwards, the samplers are put in closed containers and sent to a laboratory for analysis. The concentration value found by the analysis is an integrated time concentration. By using Fick's law of diffusion to find the sampling rate for the gas in question, and the total sampling time, an integrated mean for the sampling period can be found. A disadvantage of this method is that the samplers do not catch weekly and hourly concentration variations, which means that they are unable to predict whether the hourly concentration limit is exceeded or not.

Chapter 3

Methods

3.1 Observations

21 passive samplers were ordered from NILU's laboratory and received by mail. The samplers are supplied to NILU from IVL- Svenska Miljöinstitutet [1]. The samplers were kept cool in a refrigerator until they were used. The procedure described below was repeated for three time intervals, hereafter referred to as Period1, Period2 and Period3. The duration of each period is given in Table 3.1. Based on weather forecasts, we tried to chose sampling periods favorable of higher pollution at the receptor site. In other words, we wanted periods with low winds and winds blowing from the road towards the receptors.

Period	**From-to-dates(dd.mm.yy)**
Period1	30.01.18-08.02.18
Period2	20.02.18-02.03.18
Period3	03.04.18-13.04.18

Table 3.1: The three periods of observations with passive sampling.

Seven passive samplers were placed along the street Sørengkaia, perpendicular to the road Kong Håkon 5. gate(KH5). This is a Norwegian national road, and one of the main approach roads to the city center of Oslo. An overview of the area is given in Fig. 3.1, and a more detailed view of the placement of the samplers are shown in Fig. 3.2.

[1] https://www.ivl.se/sidor/lab–analys/miljo/luft.html

Figure 3.1: Overview of the area of interest. The dot marks the location of the meteorological measurements by the new Munch Museum, the thick line marks the finite part of KH5 used for line source calculations. The thin line marks the part of Sørengkaia where the passive samplers were placed. Map from Statens Vegvesen's online service `www.vegvesen.no/vegkart`.

Figure 3.2: The blue dots mark the position and numbering of the passive samplers along Sørengkaia. Map from Statens Vegvesen's online service `www.vegvesen.no/vegkart`.

Samplers 1-4 were attached to lampposts along Sørengkaia, number 5 and 7 where placed on traffic lights on each side of KH5, and number 6 in the central reservation

of KH5. The samplers were attached to a plastic lid to protect against precipitation and wind. The lid was then fastened to the poles with cable ties at ca 2m height above the ground, as shown in Fig. 3.3.

Figure 3.3: The pictures show a passive sampler on a plastic lid, attached to a lamp post.

After each measurement period, the samplers were taken down and sent to NILUs laboratory for analysis. The results were then reported back as an average concentration of the period for each sampler.

3.2 Meteorology

To evaluate how model generated meteorology and observed meteorology affect the performance of the dispersion models, both types of data were used in the simulations. As mentioned in the introduction, the meteorological observations and the WRF model run were performed by Pernille Borander. A more detailed description of the procedure is given in her master thesis, but a short description of the methods will be given here.

3.2.1 Observed meteorology

Wind and temperature sensors were mounted at several heights on a tower crane located near the new Munch museum, see Fig. 3.1. The sensors collected data two times every minute. The Munch data set runs from 09.01.18-01.03.18 at 20.00. This means that for the last night in Period2, and the whole Period3, observational data is not available.

The missing hours for Period2 are replaced by the corresponding hours from the night before. We considered to replace the missing hours with hours from the WRF simulation, but the wind and temperature from WRF differed significantly from the Munch measurements. Because we needed wind observations at two heights to calculate the bulk Richardson number, it was also not possible to use observations from other meteorological stations in Oslo. However, observations from the two nights at the meteorological station at Hovin indicates that there was no significant change in weather conditions between the two nights in the area (see Appendix A. Based on this, it was therefore decided that the error when averaged over the whole period would be smallest when using data from the previous night. However, these hours will not be used for hourly comparisons. Period3 will only be compared with dispersion based on modeled meteorology.

In the work with this thesis, hourly averages was calculated for temperature, wind speed and wind direction at 10m and 30m height for the two first periods. The wind direction was calculated based on wind speeds higher than 0.5m/s only. Winds speeds below this value are assumed to be so small that the calculated direction would not be accurate. This data set will hereafter be referred to as "Munch data".

3.2.2 Modeled meteorology

The modeled data is produced by the mesoscale, numerical weather forecast model WRF-ARW(Weather Research and Forecasting Model, Advanced Research WRF). The four nested domains for the simulation is given in Fig. 3.4. The model was initialized with data from the European Center for Medium-Range Weather Forecast(ECMWF) with a $0.0625° \times 0.0625°$ horizontal resolution, with an update interval of 6 hours. In WRF, several parameterization schemes for describing the physics and different variables in the PBL are available. An overview of the schemes of most importance for PBL conditions are given in table 3.2, along with the chosen options for this simulation. More detailed descriptions of the schemes can be found in Skamarock et al. [2008]. The output from WRF is representing instantaneous values for each hour. In this thesis it is assumed that these instantaneous values are representative for the whole hour, and will be regarded as hourly averages. The data from the WRF simulations used in this study will hereafter be called "WRF data".

Scheme	**Option**
PBL scheme	Mellor-Yamada-Janic(MYJ)
Surface layer scheme	Eta Surface layer
Land-surface scheme	Noah LSM with the Urban Canopy Model option

Table 3.2: An overview of the the parameterization schemes in WRF that are most important for PBL meteorology.

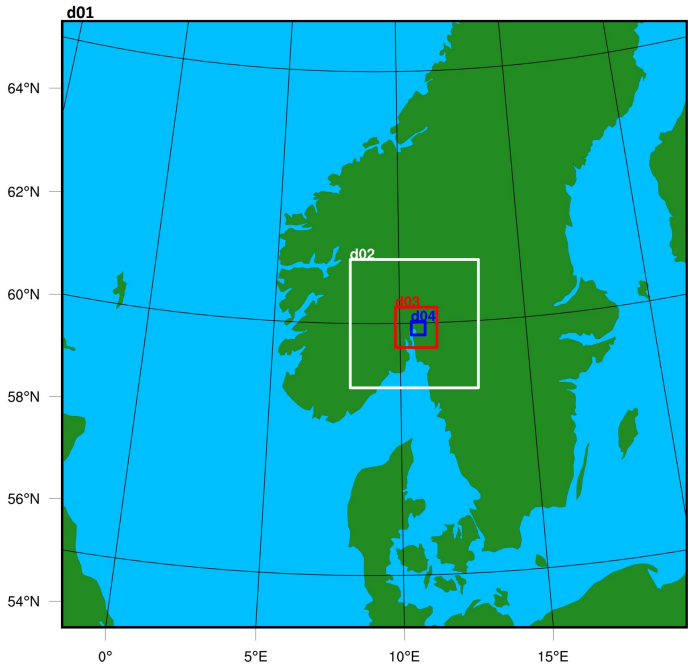

Figure 3.4: The four domains used for the WRF simulations. The horizontal resolution for each domain is d01: 13.5km×13.5km; d02: 2.7km×2.7km; d03: 0.9km×0.9km; d04: 0.3km×0.3km. Adopted from Borander's master thesis.

3.3 Model setup

3.3.1 RLINE configuration

RLINE version 1.2 was downloaded to my personal computer from the web page `www.cmascenter.org/r-line/`.

Emissions

The model was set up with two line sources, one to represent KH5 and one to represent Sørengkaia. Because the model is not coordinate based, the length of the roads was estimated based on Google Maps. Fig. 3.5 shows snapshots from Google maps, showing that the road segment of KH5 is approximately 450m, while Sørengkaia is approximately 115m. The receptors were placed every 20m in a 500x500m area, except along the KH5 line source, where receptors was placed closer to better capture the spread from the road. Receptor points to mirror the position of the passive samplers were placed along Sørengkaia. The configuration is shown in Fig. 3.6. The angle between the road and the north direction (0°/360°) is ca. 16°. The model is set up to use one average emission value ($g/m^{-1}s^{-1}$) per line source, for a longer time period. To be able to investigate hourly changes due to rush hours etc., it was decided to run each hour separately. The equations in the model are not dependent on the previous time step, so this will not affect the results.

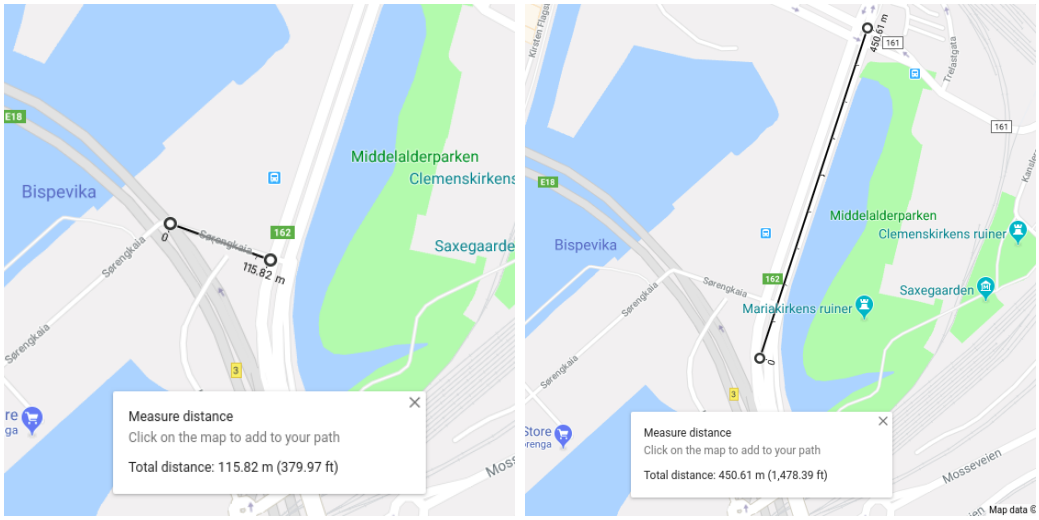

Figure 3.5: Snapshots from Google Maps, showing the length of the roads we want to model.

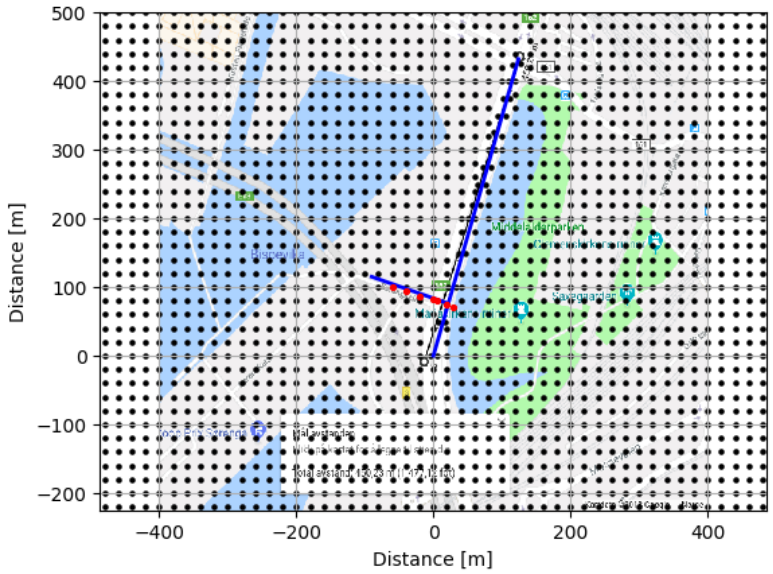

Figure 3.6: Figure showing the setup of the sources and receptors in the RLINE runs. Each dot represent a receptor point, the red dots are the receptor points that are compared to the observations.

The emission values were found as a function of Annual Average Daily Traffic(AADT), the vehicle fleet composition and temporal traffic variation. According to Statens Vegvesens data base, NVDB, the AADT for KH5 was 23 653 in 2017 [2]. To adjust the AADT to yearly, daily and hourly variations, a factor variation curve from the traffic data guide "Veileder i trafikkdata" [Gryteselv et al., 2014] was used. The curve named M2, which describes variations for "main roads in urban areas with commuting and transport"(In Norwegian: "Hovedveg i bystrøk med arbeidsreiser

[2]NVDB road reference: 0300 RV162 HP1 m470-1008

og gjennomgangstrafikk") was determined to be most suitable for KH5. The curves are given in Appendix B.

Because Sørengkaia is relatively new, we were unable to find AADT data for this street. Based on an assumption that ca 250 cars use the street when commuting from Sørenga, an estimated AADT of 500 is used. It is also assumed that the vehicle fleet composition is the same as for KH5. Because of ongoing construction work in the area, there may be a higher ratio of heavy vehicles connected to this road. However, the main contribution to pollution will be from KH5, so it is assumed that this deviation has minor effects.

By using emission factors for NO_X (in NO_2 equivalents) from Table 30 in the report Utslipp fra veitrafikken i Norge[Holmengen and Fedoryshyn, 2015], together with vehicle fleet data for Oslo Kommune from 2017, the hourly emission value was calculated as

$$\text{Hourly emission value} = \text{Emission factor} \times \text{Vehicle type fraction} \times \text{AADT}_{\text{corr}}$$

where $\text{AADT}_{\text{corr}}$ is AADT corrected for time variations.

Because RLINE only calculates concentrations from line sources, it was necessary to add a background concentration (BGC) to the output concentrations to compare the results to the observations. To account for the fact that the BGC in a city is higher than over water, it was decided to use two separate values for the BGC, depending on the wind direction. For hours with wind from the fjord side, a BGC value of 12 $\mu g/m^3$ was used. This value was chosen in agreement with my supervisor Erik Berge, and is mainly representing ship emissions. For wind direction from the city, a BGC value of 24 $\mu g/m^3$ was used. This is the yearly average for Oslo, calculated by the application "Bakgrunnsapplikasjonen" (`http://www.luftkvalitet.info/ModLUFT/Inngangsdata/Bakgrunnskonsentrasjoner/BAKGRUNNproj.aspx`).

Meteorology

Table 3.3 shows which meteorological and surface parameters that is needed as RLINE input. The model is facilitated to use surface files from the meteorological preprosessor AERMET [Cimorelli et al., 2005] for its meteorological input, but it can also take user defined input. We have chosen to use the data from Munch and WRF, and calculate the additional needed parameters from them. This allowed for more experimenting with different methods of calculation, which was useful for testing the model sensitivity to meteorology.

Parameter	Description
L	Monin-Obukhov length [m]
u_*	Surface friction velocity [m/s]
w_*	Convective velocity scale [m/s]
z_{im}	Mechanically generated boundary layer height [m]
z_{ic}	Convectively generated boundary layer height [m]
z_0	Roughness length [m]
W_s	Wind speed [m/s]
W_{dir}	Wind direction [deg]

Table 3.3: An overview of the meteorological parameters that are required to run Rline. The parameters represent hourly averaged values.

Meteorology from Munch data

L was found by first calculating the Bulk Richardson number from Eq. (2.8). It was decided to use 30m as the reference height for the calculations. This was done based on an assumption that the measurements at this height are less disturbed by surface elements and buildings than the values at 10m. The potential temperatures were calculated from the Munch data by using the equations given in Appendix C. L and u_* was derived from Eq. (2.16) and (2.19) or (2.23) depending on the stability condition. w_* was found from Eq. (2.24), with the heat flux found from Eq. (2.11). As discussed in Section 2.1.4, the boundary layer height is challenging to estimate from standard meteorological observations. In the model, the largest of z_{im} and z_{ic} are used to determine the vertical dispersion. During the periods of interest, we assume that the convectively generated boundary layer height almost always will be lower than the mechanically generated. It was therefore decided to set z_{ic} to zero for all the simulations. To investigate the importance of the PBL height, z_{im} was estimated in four different ways.

1. Use the Planetary Boundary Layer Height (PBLH) from the WRF simulations as z_{im}. This method is defining the PBL height as the point where the TKE profile decreases below a prescribed value[Banks et al., 2016].
2. Use Eq. (2.27), $z_{im} = 2400u_*^{3/2}$
3. Use $z_{im} = 500m$ constant
4. Use $z_{im} = 1000m$ constant

The surface roughness was estimated by Eq. (2.25). A circle with radius 500m was used as the total area of interest. The area and roughness elements used is shown in Fig. 3.7. Based on the wind direction, two different values were calculated. For wind directions between 135-315°,that is, from the fjord, Sørenga and Sukkerbiten were considered to be the most important roughness elements, yielding $z_{0,fjord} = 0.18$, otherwise a more urban value of $z_{0,urban} = 0.87$ was used. This was found by using the Opera House, the Barcode, estimations of the construction work in front of the Barcode, the Munch Museum and the buildings beside Mariakirken as roughness elements.

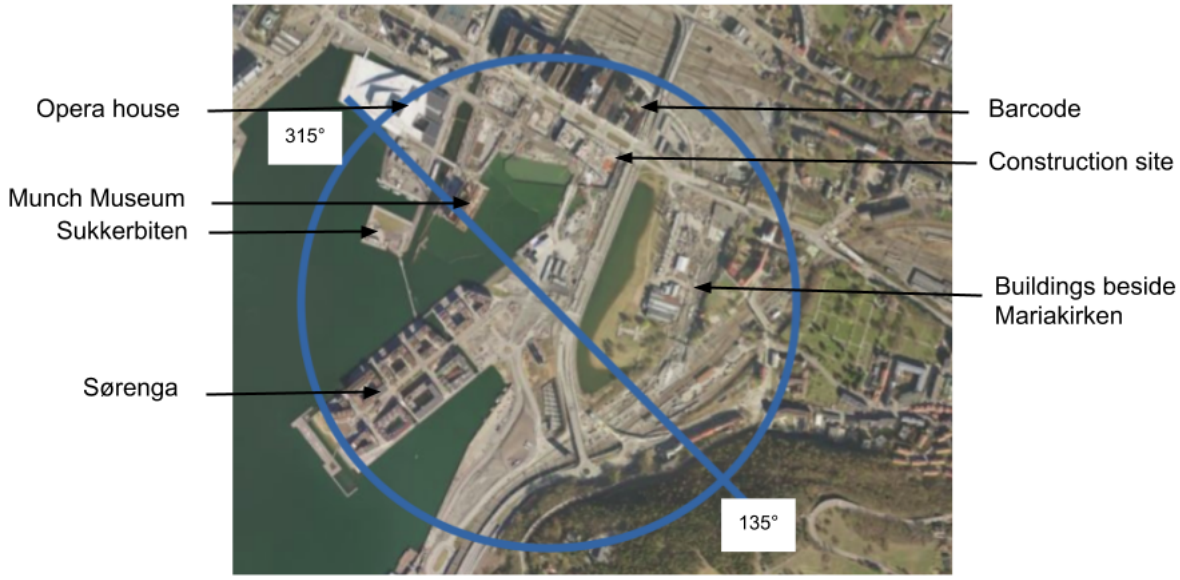

Figure 3.7: Sketch of the area included in the calculations of z_0. When the wind direction is between 135° and 315°, only the roughness elements on that side of the circle is included in the calculations. In the same way, only elements from the north- east part of the circle is included when the direction is from 315-135°.

Meteorology from WRF data

The input meteorology for RLINE was found by extracting data from the grid box covering the coordinates of Sørengkaia in the innermost domain, d04. Due to the limited resolution in the model, and because Sørengkaia is located close to the fjord, this grid box is defined as water in the WRF setup. This introduced an opportunity to investigate the effect of different land use definitions from the model. Therefore, data from the closest grid box defined as land was also extracted, so that they could be compared. Data from the two grid boxes will be referred to as the "WRF water grid box" and the "WRF land grid box".

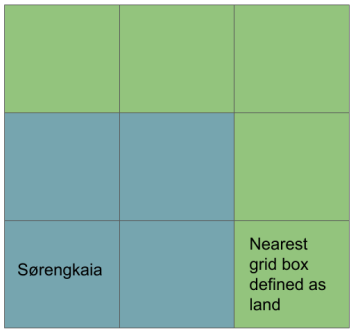

Figure 3.8: Sketch of the grid box containing the coordinates of Sørengkaia in relation to the grid box used to represent land conditions.

From the WRF data, the variables listed in Table 3.4 was collected from the grid boxes in Fig. 3.8. The data was extracted by using NCL (NCAR Command Language) scripts. With the help of NCL functions, the wind and temperature data was interpolated to find the potential temperature and wind speed and direction at 10m and 30m. z_{im} and u_* was found directly from PBLH and UST, respectively. L was found as 1/RMOL, and w_* by using HFX/ρc_p, PBLH and the potential temperature in Eq. (2.24). There is only one value for z_0 for each grid box, $z_{0,water} = 0.0001$ and $z_{0,land} = 0.14$. Following the theory in Section 2.1.3, both of these are too low to represent the urban location we are interested in. However, because variables such as u_* depend on z_0, it was not possible to change the roughness without introducing an inconsistency in the WRF data. It was therefore decided to run with the constant values of each box.

Variable name	**Description**
T	Temperature [K]
U	x-wind component [m/s]
V	y-wind component [m/s]
HFX	upward heat flux at the surface [W/m^2
PBLH	PBL height [m]
Z0	Background roughness length [m]
RMOL	1./Monin Ob. Length [m^{-1}
UST	u_* in similarity theory [m/s]

Table 3.4: The table gives an overview of the WRF variables that was used to find the parameters needed to run RLINE

3.3.2 EPISODE configuration

With great help from Gabriela Sousa Santos and Torleif Weydahl at NILU, EPISODE version 8.0.1 was set up and run on my personal computer.

Emissions

The emissions in EPISODE are divided into several categories; emissions from line sources, upper, lower and ground area sources, and point sources. The files containing the emission data for NO_2 and NO were prepared by Henrik Grythe at NILU. Roads with an AADT above 1500 were defined as line sources, while smaller roads were defined as area sources. Fig. 3.9 shows the road network used to represent road emissions in Oslo. In addition to the emissions, hourly background concentration data from the measurement station at Grønland was used. This station measure NO_2 and O_3 concentrations hourly at ca. 25m above ground. For NO a constant value of 0.2 $\mu g/cm^3$ was used. The Grønland station measures background concentrations in an urban environment, while ideally we should have used regional background concentrations. Therefore, it was decided to leave out the area sources that represent small roads, shipping, residential burning and off road sources, under the assumption that these contributions to a large extent are measured at the Grønland station.

Figure 3.9: The lines represent the line sources used to model the emissions from roads with AADT > 1500 in the EPISODE runs.

Because RLINE was set up with only KH5 and Sørengkaia as line sources, it was decided to do EPISODE runs with only KH5, in addition to runs with all roads included. The two emission setups will be referred to as "all-roads" and "KH5-only". It is assumed that Sørengkaia has an AADT of less than 1500, and therefore no line source to represent this road is used in the EPISODE configuration. It should be noted that because all roads are represented by straight line segments, there are some deviations from the EPISODE setup and the real roads they represent. This may be a source of error in the calculated concentrations. Seven receptors were placed to represent the positions of the passive samplers along Sørengkaia. Because of the deviation of the EPISODE line sources and the actual roads, some extra receptor points were added, to better capture the gradient outwards from the road.

Munch data meteorology

The Eularian model in EPISODE needs a 3D wind field. This field was calculated by using a Mass Consistent Wind field model, MC-WIND. This model is designed at NILU to create the wind field, and to create other meteorology files to be used in EPISODE. The wind field was created by using wind data from the meteorological observation sites Blindern, Hovin and Tryvannshøgda, in addition to the Munch data. The data from the observational sites were collected from the online service delivered by the Norwegian Meteorological institute, `www.eklima.no`.

Table 3.5 gives an overview of the meteorological data used as input to the EPISODE runs based on observations.

Location	Variable
Munch data	Wind 10m, 30m Air temp 10 m
Blindern	Wind 10m Precipitation Cloud cover fraction
Hovin	Wind 10m Vertical temperature difference Relative humidity
Tryvannshøgda	Wind 10m

Table 3.5: Meteorological data used as input in EPISODE.

For Period1, Gabriela Sousa Santos at NILU created the meteorology files based on the data given in Table 3.5. I used this file as a template, and made similar files for Period2. The resolution in these simulations are 1km×1km, and there are 38×27 grid boxes in the horizontal, and 10 in the vertical. The domain in the Munch data runs are shown in Fig. 3.10.

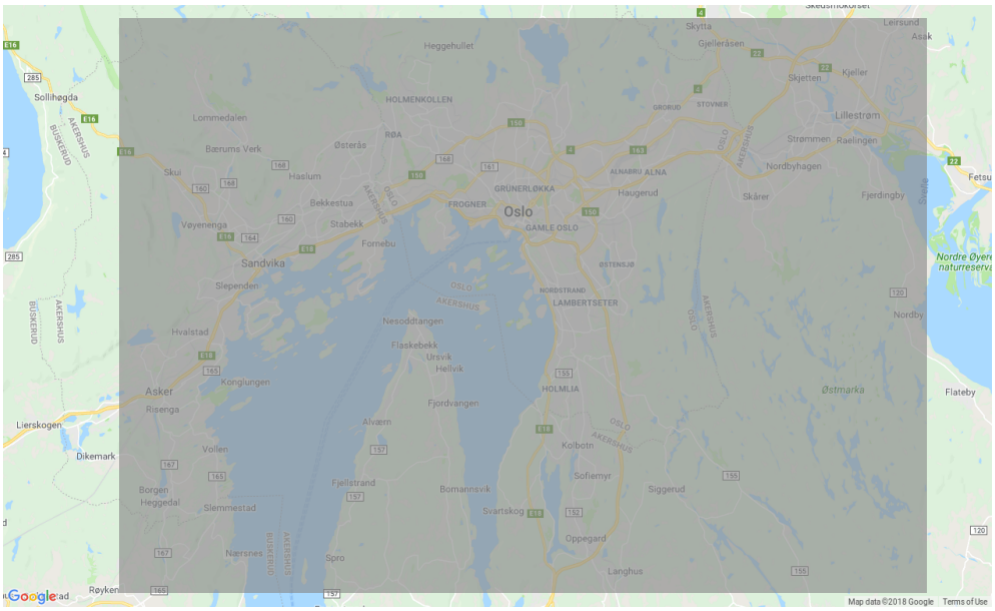

Figure 3.10: The gray shaded area on the map marks the EPISODE domain for the WRF data based simulations.

WRF data meteorology

WRF data for domain d03 (see Fig. 3.4) was post-processed by Gabriela Sousa Santos at NILU to be used as the meteorological input for EPISODE. This data has a resolution of 900m×900m.

The domain for the WRF data simulations are shown in Fig. 3.11. There are 32 grid boxes in the vertical, and 18x18 grid boxes in the horizontal, with the Munch mast located in the center of the domain.

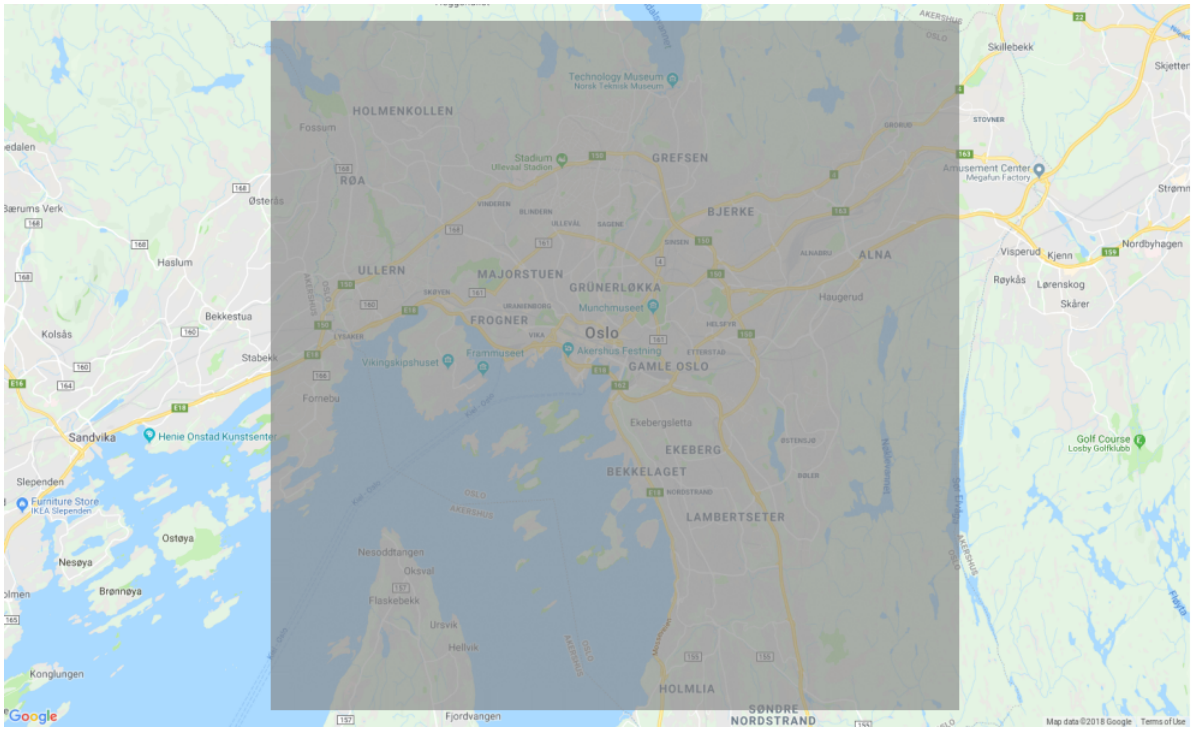

Figure 3.11: The gray shaded area on the map marks the EPISODE domain for the WRF data based simulations.

Chapter 4

Results and discussion

The structure in this chapter is as follows: First, an overview of the weather situations for the three periods is presented. This is followed by the results from the passive sampler measurements. Then, the results from the model runs will be presented and discussed, period by period. For the RLINE simulations with Munch data, only the results based on the PBL height alternative number 2), the Venkatram formulation will be presented. This is based on the sensitivity test in Section 4.7.1. The differences of modeled and observed meteorological input will be discussed, and cases of special interest will be commented. A comparison between the EPISODE simulations and measurements from the air quality station at Åkebergveien is presented to compare the hourly modeled concentrations with hourly observed concentrations. Sensitivity tests and discussions for specific meteorological variables will be given towards the end, in an attempt to quantify the relative importance of the meteorological parameters.

4.1 Weather patterns for the three periods

Here, an overview of the weather conditions in Oslo for the three periods is presented. The geopotential maps shown in this section are downloaded from `http://www.wetterzentrale.de/en/reanalysis.php?map=1&model=cfsr&var=1`. The weather information from Blindern are downloaded from `www.eklima.no`.

4.1.1 Weather situation for Period1

The first days of Period1, 30.02.18-02.02.18 were dominated by the passing of a low pressure system from west to east. Fig. 4.1 shows that these days had the highest temperatures in the period, around 0°C, and winds mainly from south-west to south-east. The remains of the low pressure can be seen north of Italy in Fig. 4.2. The situation in Fig. 4.2 gave the strongest winds in the period, with wind direction from north to north-east. At the end of the period, from ca 05.02.18-08.02.18 winds were calm, between 0-2 m/s.

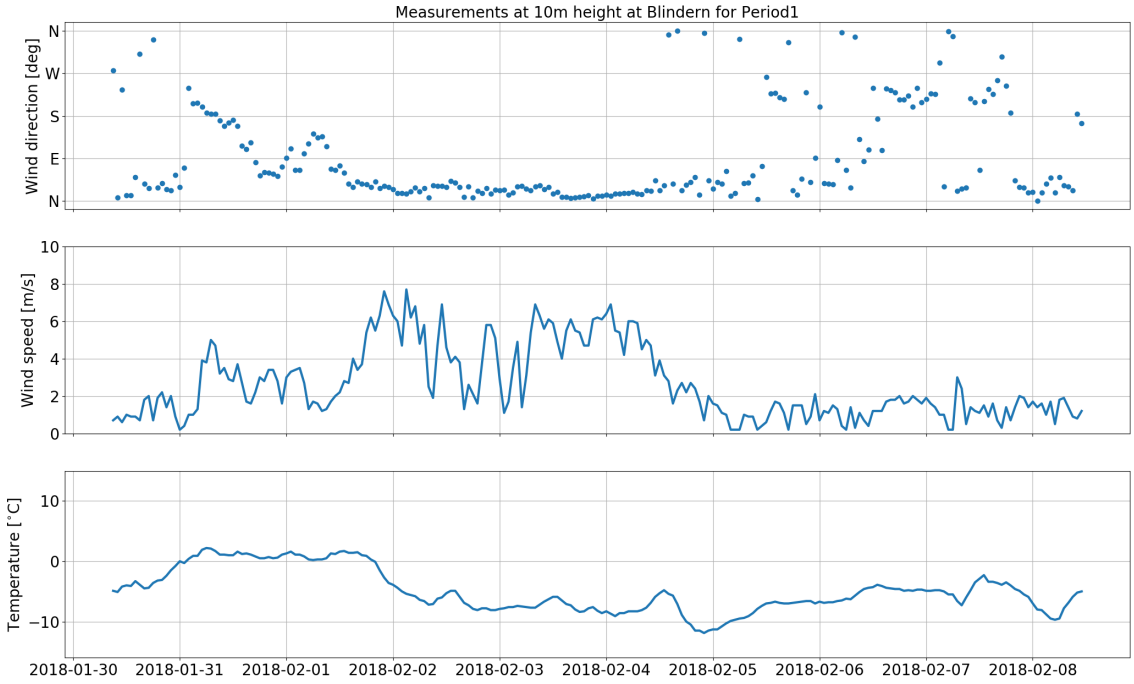

Figure 4.1: Wind direction and temperature at 10m at Blindern meteorological station for Period1.

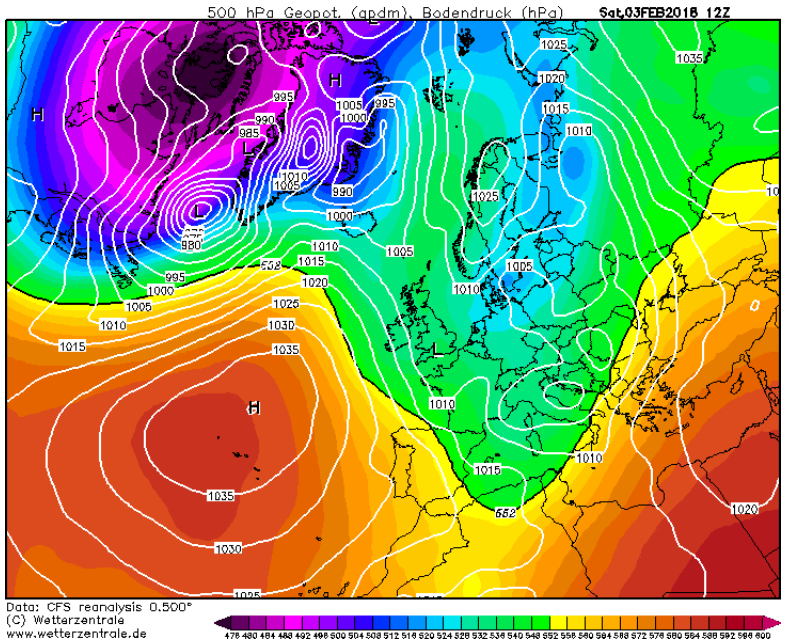

Figure 4.2: 500hPa geopotential height map for 03.02.18 at 12:00 UTC. The white lines denotes mean sea level pressure.

4.1.2 Weather situation for Period2

The wind speeds were generally low for the first six days in Period2, ca 0-3m/s, see Fig. 4.3. During 26.02.18, the high pressure seen in Fig. 4.4, moved down from the

north of Norway, and stayed approximately at the location in the figure for the rest of the period. This gave stronger winds from north-east and colder temperatures for the remaining days in the period.

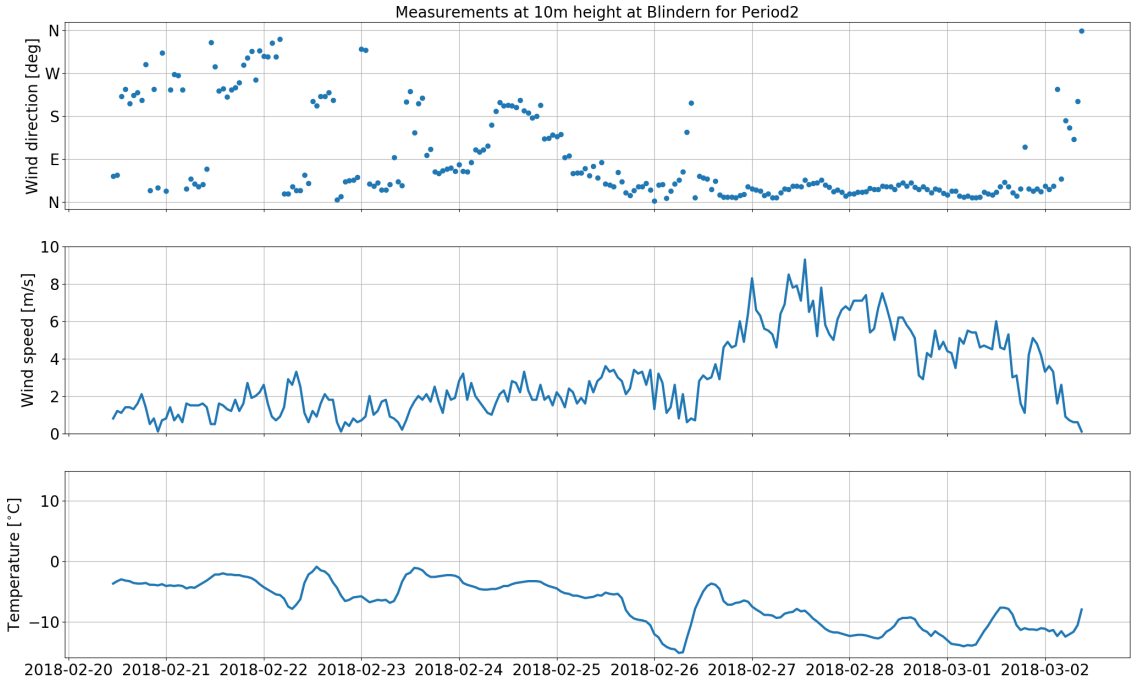

Figure 4.3: Wind direction and temperature at 10m at Blindern meteorological station for Period2.

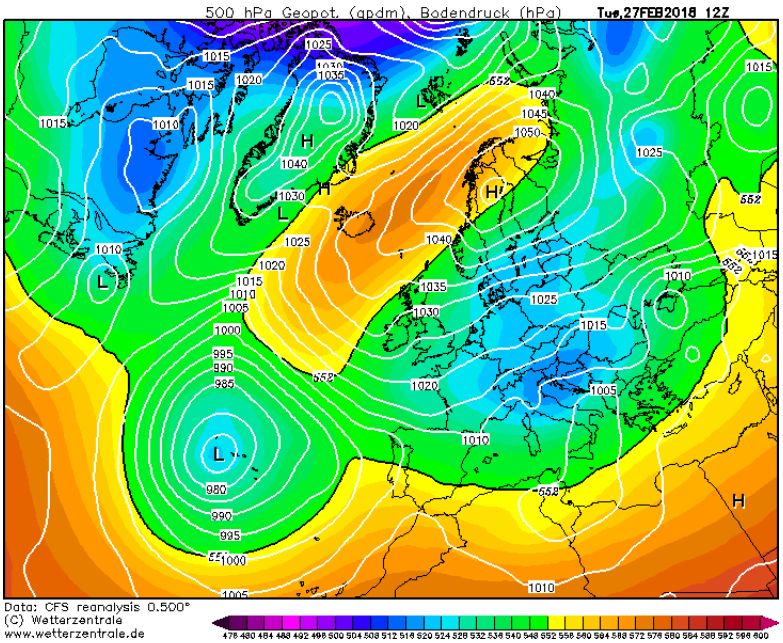

Figure 4.4: 500hPa geopotential height map for 27.02.18 at 12:00 UTC. The white lines denotes the mean sea level pressure.

4.1.3 Weather situation for Period3

From Fig. 4.5, we see that the first days of the period, from 03.04.18-07.04.18 were dominated by winds with an average speed around 2 m/s. The direction vary significantly from day to day. From 08.04.18-13.04.18 the direction is stable from north-east, and the average speed around 3 m/s. The overall pattern is similar to Period2, but the changes in wind speed between the first and last half of the period is not as significant as for Period2. The temperature is significantly higher than the two first periods. Fig. 4.6 shows a geopotential map for 08.04.18 at 12.00 UTC.

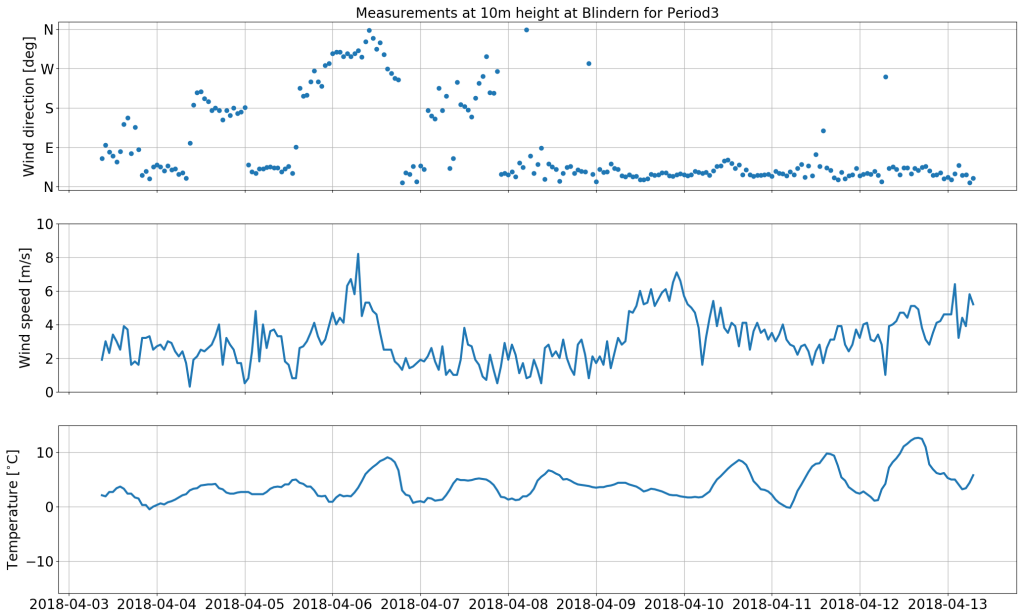

Figure 4.5: Wind direction and temperature at 10m at Blindern meteorological station for Period3.

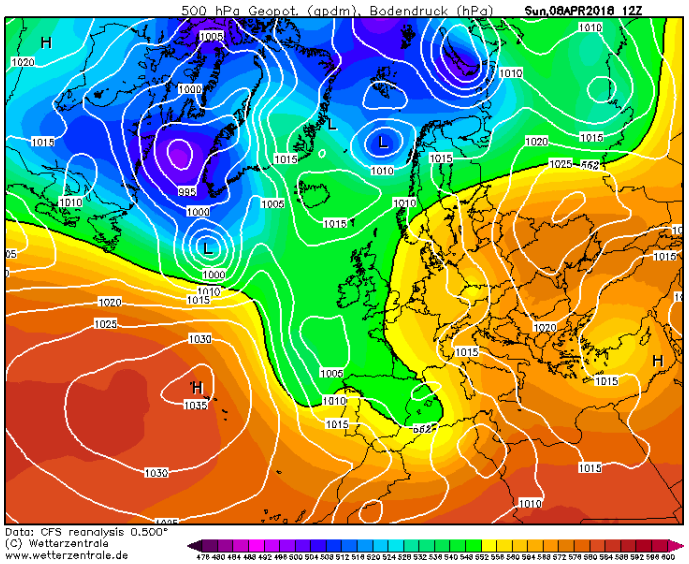

Figure 4.6: 500hPa geopotential height map for 08.04.18 at 12:00 UTC. The white lines denotes the mean sea level pressure.

4.2 NO_2 concentrations from passive samplers

Table 4.1 holds the results from the passive samplers in the three periods. The values from the table are plotted in Fig. 4.7. The error bars are showing the 10% uncertainty of the samplers. In this figure, and all other plots of average results in this chapter, the values at 0m represent sampler nr. 1, i.e. furthest away from KH5, while the rightmost values represent sampler nr. 7, on the opposite side of KH5 (see Fig. 3.2).

Sampler Number	**Period1** $[\mu g/m^3]$	**Period2** $[\mu g/m^3]$	**Period3** $[\mu g/m^3]$
1	33	28	27
2	32	24	27
3	34	26	31
4	35	28	32
5	37	28	33
6	39	31	34
7	61	25	23

Table 4.1: NO_2 concentrations from each passive sampler for the three periods. The values are integrated averages for the sampling periods.

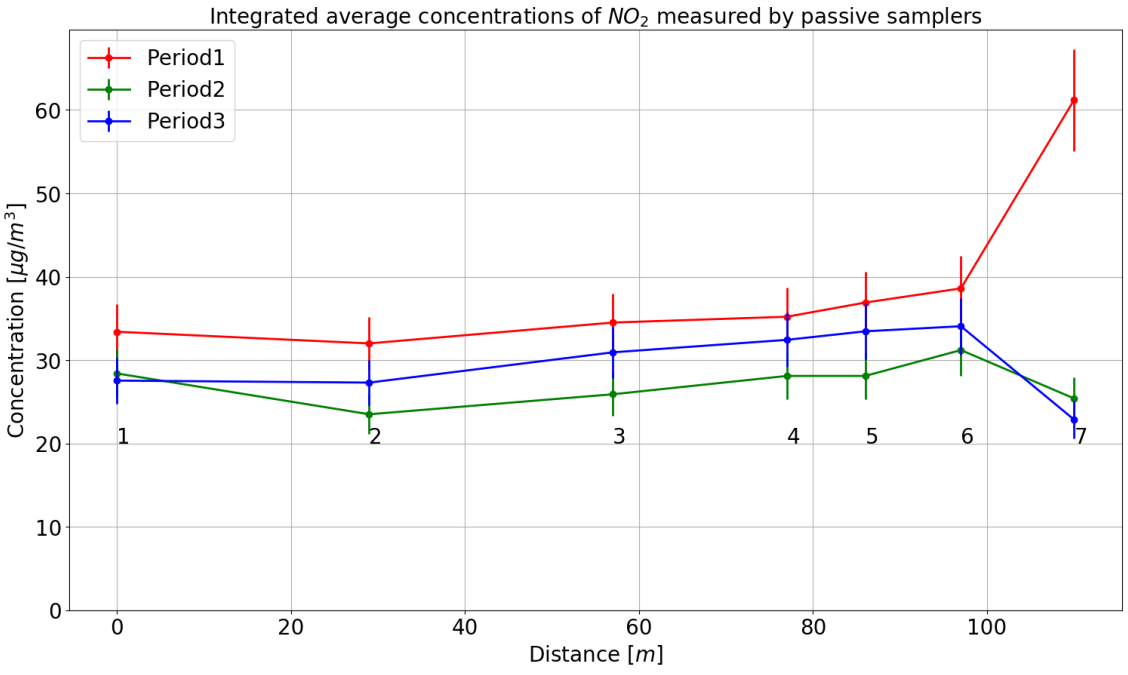

Figure 4.7: Integrated average concentrations of NO_2 measured by each of the seven samplers for the three sampling periods. The error bars represent the 10% uncertainty in the passive samplers. The numbers denote the name of the sampler.

Except for sampler 7 in period 1, all samplers yield concentrations in the range between 20-40 $\mu g/m^3$. Sampler 7 in Period1 have an average concentration of $61 \mu g/m^3$,

which is more than twice as high as the sampler 7 values for the two other periods. An experiment setup with two passive samplers at each location would have made it possible to rule out contamination of the sampler. Hourly measurements would also have made it easier to detect exactly when the high concentrations occurred, and then possibly why. Because the sampler location is very close to the road side, the high concentration may have been caused by one or several episodes of idling vehicles close to the sampler. Another possible cause could be that the wind was directed more from the road towards the sampler during this period. However, it is not possible to conclude on this based on either the data observed at the Munch mast or the Blindern data in Fig. 4.1. As we will see, the model simulations do not indicate any significant differences for sampler 7 between the periods. Therefore, with the available data, it is not possible to conclude on a specific explanation for the value. The decrease in concentration from sampler 6 to sampler 2 is $7\mu g/m^3$ for all three periods. The slight increase in concentration for sampler 1 seen for the first two periods may be explained by the crossing road (see Fig. 3.1).

If we compare the values in Table 4.1, with the limit values in Table 2.3, we see that except for the value for sampler 7 in Period1, all values are below the yearly limit. However, the results tell nothing about the hourly concentrations at the location. As we will see in the results presented below, the models predict large hourly variations, and several hours above both the yearly and hourly limit values.

4.3 Modeled results for Period1

In this section, the hourly results from the model simulations are presented first, before the averages of the simulations for Period1 are compared to the measurements, and to each other. In the presentation of the hourly results, specific topics of interest will be discussed in more detail.

4.3.1 Hourly modeled results, Period1

Hourly results from RLINE, Period1

Fig. 4.8 shows the hourly results for three receptor points from the RLINE simulation. The receptor points represent the sampler location 1,5 and 7, and will hereafter be referred to as receptor 1, receptor 5 and receptor 7. The points have been chosen to represent the concentration gradient outwards from the road.

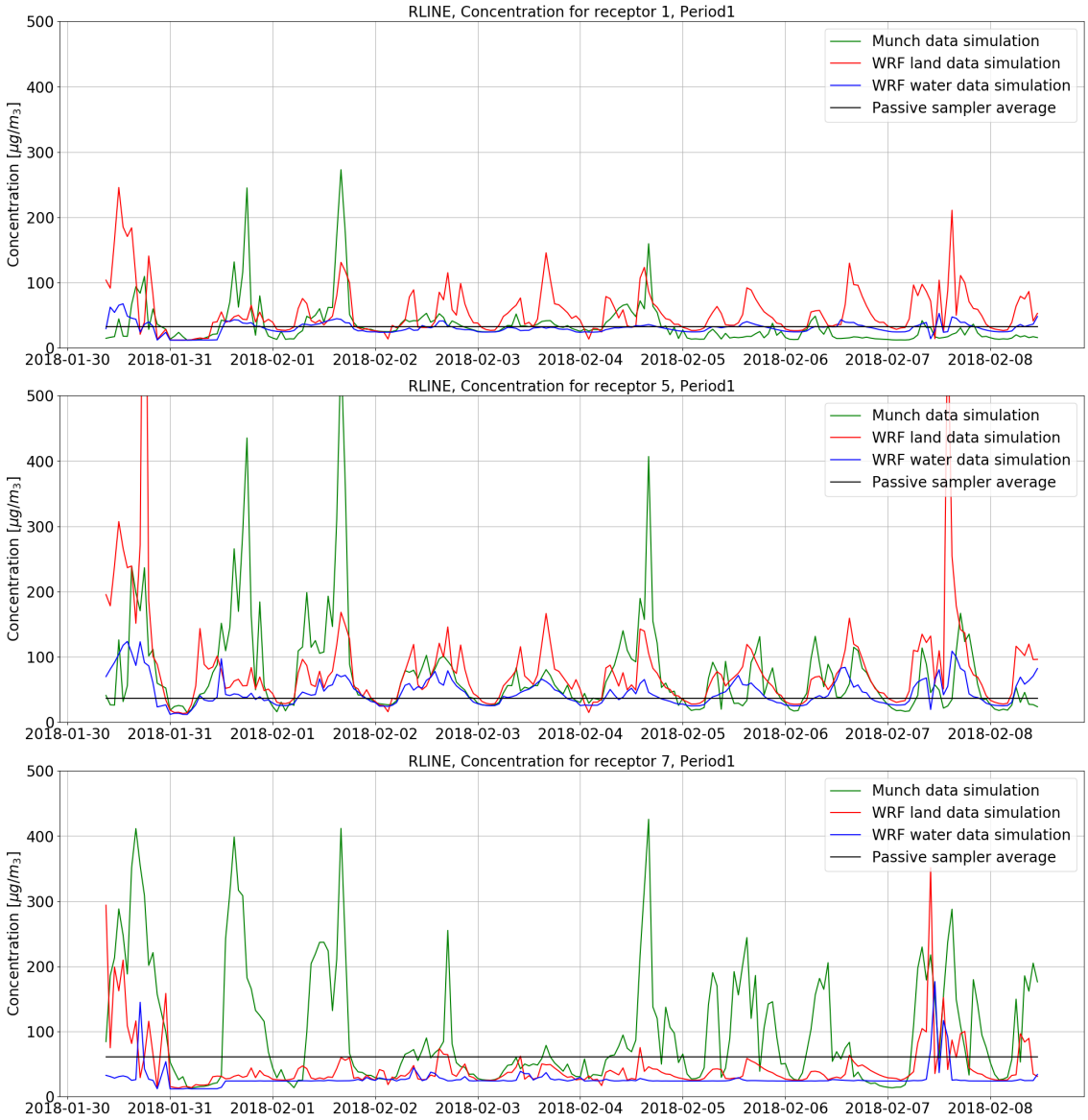

Figure 4.8: The plots show the hourly calculated NO_2 concentrations from the RLINE simulations for receptor 1(top), 5(middle), and 7(bottom) for Period1. The spikes that exceed the plot for receptor 5 for the land grid box have a value of $1074\mu g/m^3$(leftmost) and $633\mu g/m^3$ (rightmost). The exceeding value for the Munch data simulation are $573\mu g/m^3$. The black line marks the average concentration measured by the corresponding passive sampler.

The black lines in Fig. 4.8 represent the period average concentration from the corresponding passive samplers. For receptor 1, the simulation based on Munch data and WRF water grid box data are generally in the same range as this average, except for some concentrations spikes in the Munch simulation. The WRF land data simulation is generally too high compared to the sampler. For receptor 5, the diurnal emission variation is evident for all simulations. For receptor 7 the two WRF based simulations generally give concentrations well below the average, while several large spikes in the Munch simulation will affect the calculated average

significantly. The simulations based on Munch data and WRF land data show several high concentration spikes for certain hours. The simulation based on data from the WRF water grid box shows least variation, and for receptor 7, the values are almost background concentration only for the whole period ($12\mu g/m^3$ and $24\mu g/m^3$). This may be explained by a combination of the wind direction and the stability conditions in the WRF water grid box meteorology. Fig. 4.9 shows the wind speed and direction for Period1, as modeled by WRF and measured at the Munch site. The modeled wind speeds are significantly higher than the measured Munch data. The average wind speed for Period1 is ca 1.5 m/s for Munch data, and ca. 4.0 m/s for the WRF land grid box, and 4.5m/s for the WRF water grid box. Between 01.02.18 and 04.02.18 all data sets show north-easterly winds. For the other days in the period, there are larger deviations. While the Munch data has no wind from east, the majority of the wind from WRF are easterly. The consequences of these wind values for the WRF water grid box seems to be that the relatively strong winds transport the pollution away from receptor 7, but giving higher concentrations at receptor 5. The diurnal variation in emissions is clearly seen at receptor 5. For receptor point 1, the diurnal variation is not as evident, and the average concentration has fallen from $46\mu g/m^3$ for receptor 5 to $30.7\mu g/m^3$ for receptor 1.

The wind speed for the land grid box is slightly lower than for the water grid box. This may explain some of the concentration difference between the two simulations, but other factors may also have an impact. As mentioned in Section 3, the surface roughness for the two boxes are $z_{0,water} = 0.0001m$ and $z_{0,land} = 0.14m$. From Eq. 2.16, we know that higher surface roughness generally leads to lower concentrations, due to an increase in friction velocity. However, the opposite is the case here, and another mechanism seems to be dominating. Fig. 4.10 shows the MO lengths from the WRF and Munch data sets. Values above |L|=100m are assumed to be neutral, and a limit of |L|=100m is applied in the figures to better see the variations for the lower values. The MO length for the water grid box is almost always negative, corresponding to unstable conditions. The land grid box show more variation, but is mostly positive, meaning mainly stable conditions. From Fig. 2.7 we know that the dispersion capability of the atmosphere is smaller in stable conditions, while unstable conditions gives more mixing, and therefore more dispersion. This is in line with the concentration pattern of the simulations with the two WRF grid boxes. This indicates that the stability conditions are affecting the dispersion to a greater extent than the surface roughness value. The importance of the stability and surface roughness is further discussed in Section 4.8 and 4.7.3, respectively. The MO length calculated based on Munch data also tend to vary, but the majority falls within the neutral regime. Until ca. 02.02.18, there are more stable cases (on the positive side of the graph), while from ca. 05.02.18, the conditions are more unstable. This may explain why we see more spikes in the first period for the Munch simulations in Fig. 4.8.

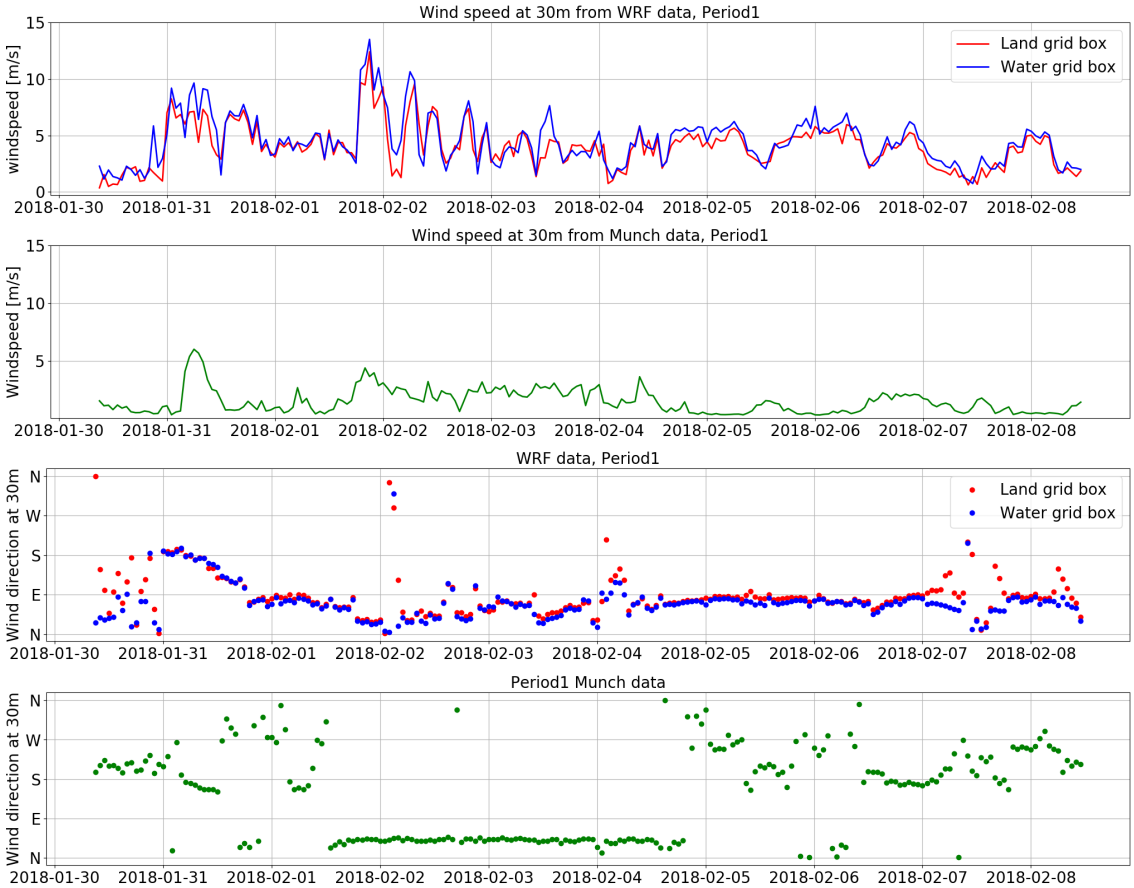

Figure 4.9: Wind speed and direction at 30m for Period1 from the Munch and WRF data sets.

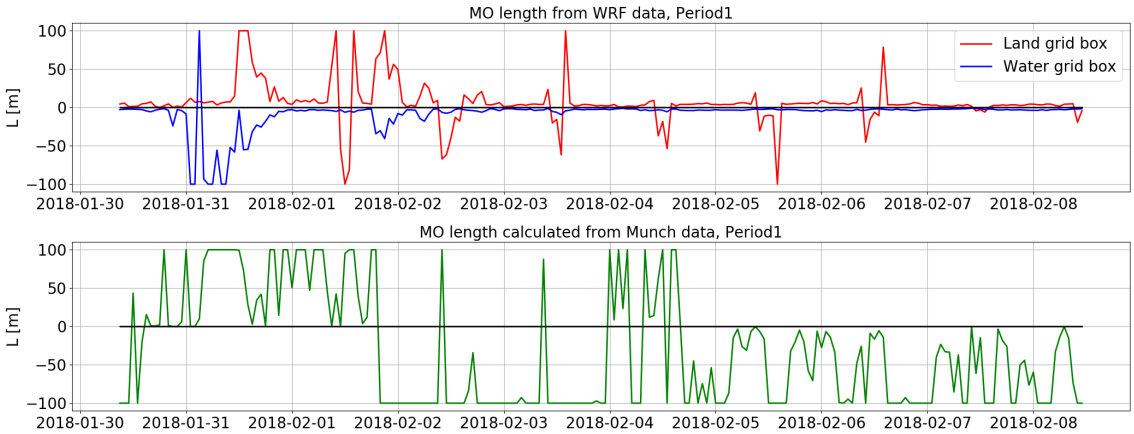

Figure 4.10: The top plot show the MO length, L, as calculated by WRF, while the bottom plot show the MO length values calculated based on the Munch data. Values above |L|=100m are set to L=± 100m, to better visualize the lower values. Hours with |L| above 100m is assumed to be neutral.

The concentration spikes for the WRF land grid box and the Munch data simulations all occur in the afternoon, when the emissions are highest (see the diurnal factor

curve in Appendix B). However, the calculated concentrations are assumed to be unrealistically high, even for rush hours. Observations from the high-traffic air quality stations at Hjortnes and Manglerud never exceeds $200\mu g/m^3$ during any of the periods (see scatter plots in D). It is unlikely that the concentrations in our area of interest would be higher than this. Therefore, we turn to the meteorology for an explanation. In Table 4.2, meteorological data for two hours are presented. The chosen hours are the ones that give the largest spikes for the WRF land data simulation, hour 19 at 30.01.18 and hour 15 at 07.02.18. The data from the other data sets are included for comparison.

Date	**Hour**	**Data set**	$\mathbf{u_*}$	**L**	$\mathbf{W_{dir}}$	$\mathbf{W_s}$
30.01.18	19	Land	0.064m/s	0.013m	21°	0.93m/s
		Water	0.097m/s	-2.274m	26°	1.96m/s
		Munch	0.010m/s	1.9709m	199°	0.53m/s
07.02.18	15	Land	0.079m/s	0.490m	26°	1.28m/s
		Water	0.107m/s	-1.98m	15°	2.49m/s
		Munch	0.117m/s	-983m	220°	1.46m/s

Table 4.2: Selected meteorological values for hours with large calculated concentrations in the RLINE land water grid box simulation for Period1

For the land grid box, L is very low and positive, with $1/L=76.9m^{-1}$ for the first hour and $1/L=2.04m^{-1}$ for the second hour. This correspond to the most stable class, F, in the Pasquill classification in Fig. 2.2. The wind speed is also low. In addition, the wind direction is close to parallel to KH5. As mentioned in Section 2.2 the line source model formulation looses validity the further away from perpendicular the wind direction turns. The problem is also discussed in the paper describing the model, by Snyder et al. [2013]. In a comparison of the model performance with an SF_6 tracer experiment, the model tended to overpredict by a little less than a factor 2 for hours with close to parallel winds. In the same paper it is also found that the model performance were poorest in light wind conditions. Contour plots of the concentration distribution for the two hours are shown in Fig. 4.11. The shape of the area with the highest concentrations in the contour plots explain why the concentration spike is not visible for receptor 1, and much lower for receptor 7. The overestimation for stable hours with close to parallel wind directions can affect the averaged concentrations, especially for the receptors closest to the road. The effect of this issue is further investigated in Section 4.7.4. The Munch data for 30.01.18 are also giving stable conditions, low wind speeds and close to parallel wind direction. However, with the wind direction 199° most of the line source lies downwind from the receptors, and the effect will therefore not be seen in our receptor points. The wind direction in the water grid box is also close to parallel to the source, but conditions are unstable, and the wind speed higher. The calculated concentration from this grid box is also elevated, but not to the same degree as for the land grid box.

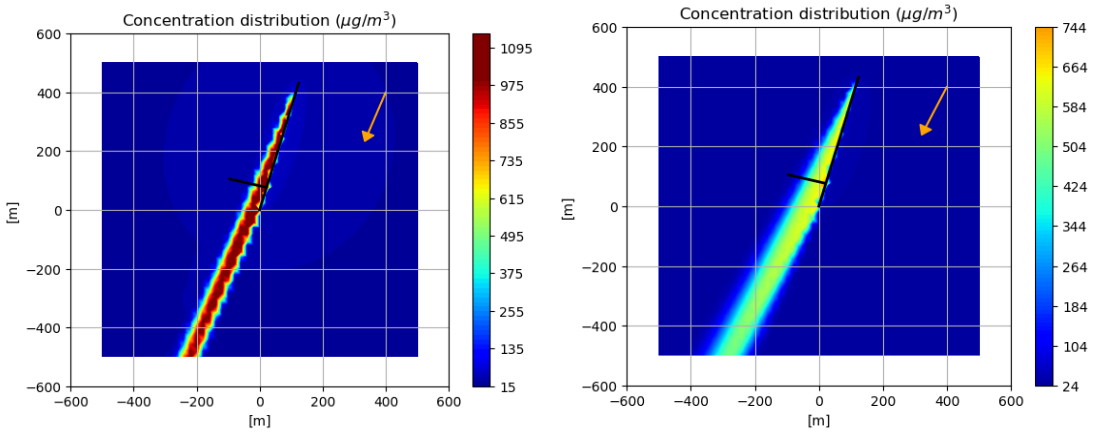

(a) **(b)**

Figure 4.11: Contour plots of the calculated hourly mean concentrations of NO_2 for (a) 30.01.18, hour 19 and (b) 07.02.18, hour 15, for the RLINE WRF land grid box simulation. The arrows are indicating the wind direction. the black lines represent the roads KH5 and Sørenkaia.

Hourly results from EPISODE, Period1

Fig. 4.12 shows the hourly concentration for receptor 1,5 and 7 from the EPISODE all-roads simulations of Period1. Note that the concentration range (y-axis) is significantly lower than for the RLINE simulations. There is also no high concentration spikes, as there was for the RLINE results. This may to be explained by the definition of the dispersion parameters in the Gaussian plume equations for the line source models. The fact that RLINE uses the surface parameters directly in the dispersion parameters makes the model more sensitive to the specific values of the meteorological input, which may cause high values in certain conditions. It may also seem like EPISODE is less sensitive to the parallel wind problem.

Note that the "Munch simulation" here refers to the simulation using the meteorological field based on the data listed in Table 3.5, not only data from the Munch mast. To extract the exact meteorological data for the area from EPISODE would require significant time and work, and has therfore not been done. However, we may assume that the wind field is similar to the conditions at the Munch mast (Fig. 4.9), and also to some extent to the Blindern data (Fig. 4.1). The conditions in the WRF simulations (which is using WRF output from domain 3, see Fig. 3.11) is assumed to be most similar to the water grid box data, as the domain 3 grid box that covers the Munch and Sørenga area is defined as water.

For the first half of the period, it is the Munch data simulation that generally gives the highest concentrations, while for the second half, the Munch simulation tend to give lower concentrations. This trend is visible for all receptors. This trend may to some degree be seen for receptor 1 in the RLINE simulations in Fig. 4.8, but with the large variation between the receptors it is not possible to say if this is a coincidence or not.

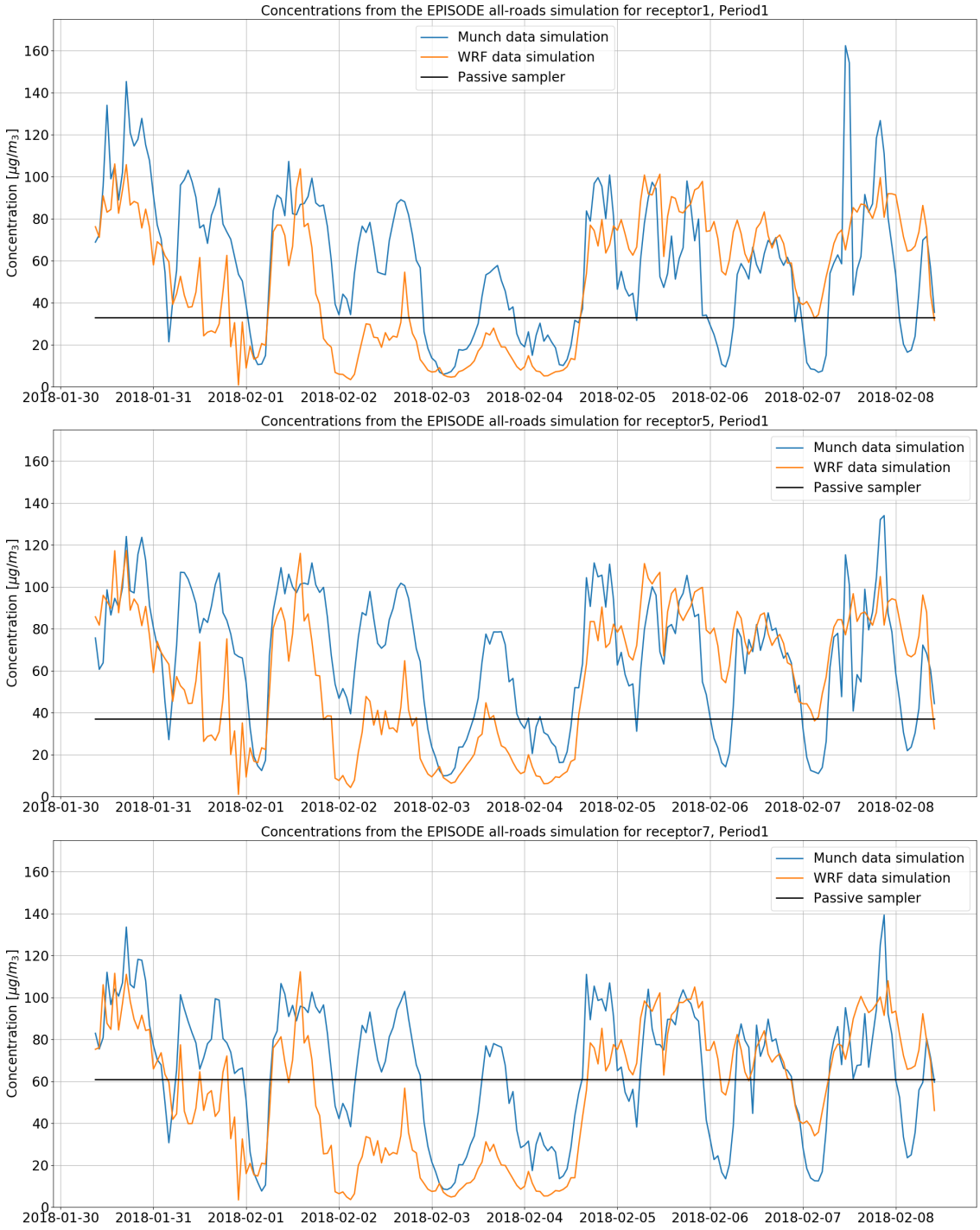

Figure 4.12: The plots show the hourly mean calculated concentrations from the EPISODE simulations for receptor 1(top), 5(middle), and 7(bottom) for Period1. The black line marks the average concentration measured by the corresponding passive sampler.

4.3.2 Comparions with passive samplers, Period1

In Fig. 4.13, the resulting averages based on the hourly calculated values from the dispersion simulations are presented, along with the result from the passive samplers.

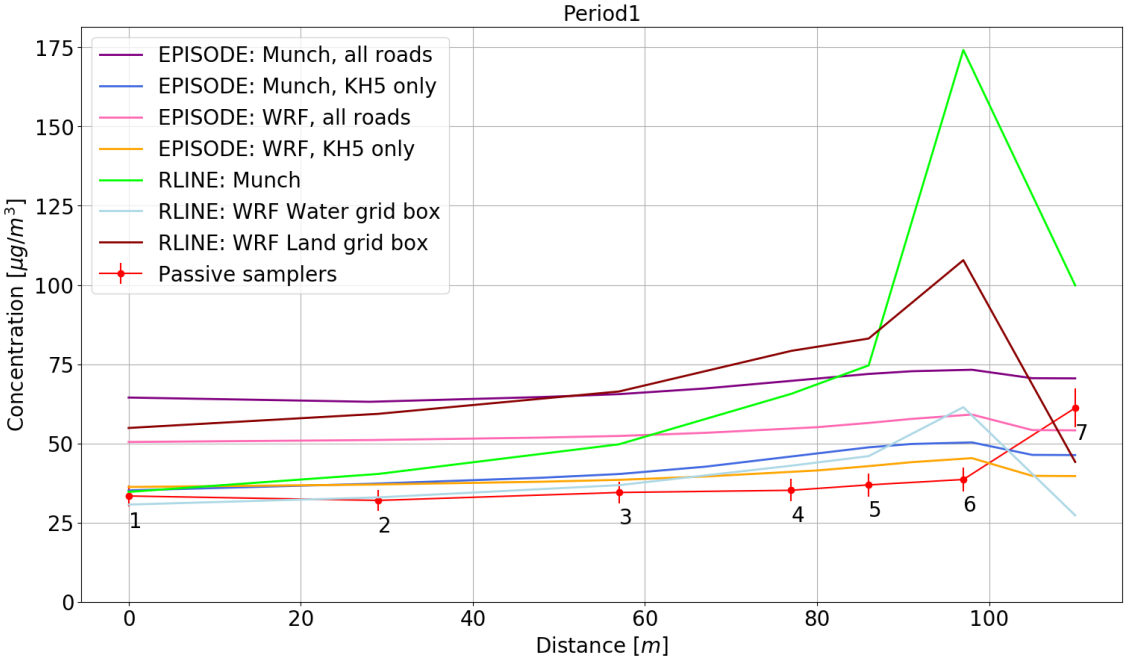

Figure 4.13: Averages based on the hourly calculated NO_2 concentrations for Period1. The figure shows the results from both the RLINE and EPISODE simulations, together with the observed result from the passive samplers. The numbers denote the different receptor points.

The slope of the gradients outwards from the road are generally similar to the observations. However, the RLINE simulations show greater deviations closer to the road. The general tendency of all the simulations is overestimation, but some simulations show good correspondence for the receptors furthest from the source. The WRF water grid box simulation show the best fit with the observations at receptor 1,2, and 3. However, this is not enough to say that this data set is the closest to the actual meteorological conditions. The $z_{0,water}$ value of 0.0001m is unrealistically low for the area around Sørengkaia, and the big difference in wind speed between modeled and observed data indicates that the winds from the data set may not be reliable. It is also questionable if the stability conditions are representative, this is discussed more in Section 4.8.

Both EPISODE KH5-only runs and the RLINE Munch simulations show a good match at receptor point 1. The EPISODE all-road simulation with WRF data overestimates the concentrations with about 20μg/m^3, except for at receptor 7, while the Munch data simulation overestimates concentration with 31-35μg/m^3, except for at receptor 7. The fact that the KH5-only runs have a better match with the observations suggests that KH5 is the main contributor to the measurement area, in addition to the urban background concentrations.

The greatest overestimation is done by RLINE at receptor point 6. This may be explained by the spatial dependence of the dispersion parameters, Eq. (2.38)-(2.41). When x becomes small, that is, the receptor is close to the source, the dispersion coefficients tends to zero, hence, the concentration tends to infinity. To account for this, the model automatically moves a receptor point to 1m away from the source

if it is too close, but in this case, this might not be enough to avoid the problem. Another contributing factor may be that the mechanical turbulence induced by vehicles is not represented well enough. The overestimation is much larger for the simulation with Munch data (green), than the simulations with WRF data(light blue and dark red). The reason for this must lie in the meteorological input, since the emission data for the runs are identical. This issue is further discussed in Section 4.7.2. In EPISODE, the minimum distance between the road and receptor is set to 5m, which may explain why we do not see the same, large overestimation in the EPISODE results.

In the EPISODE simulations, the WRF based meteorology are closest to the observed meteorology, but there is still significant overestimation for the all-road simulations. In the RLINE simulations, the WRF water grid box simulation are closest to the observed, while the WRF land grid box simulation has the largest overall overestimation. The Munch based simulation are in between the modeled simulations, except for close to the source. Based on these results, it is hard to make a statement about the performance of the modeled meteorology relative to the observed meteorology.

4.4 Results for Period2

Here, the hourly results from the model simulations are presented first, before the averages of the simulations for Period2 are compared to the measurements, and to each other.

4.4.1 Hourly modeled results, Period2

Hourly RLINE results, Period2

Fig. 4.14 shows the hourly calculated concentrations for receptor 1,5 and 7 from the RLINE simulations for Period2. Again, it is the simulation with meteorology from the WRF water grid box that give the lowest concentrations, with almost only background concentrations at receptor 7. The general pattern of the WRF land data simulation is similar to Period1, however, none of the spikes are as high as for Period1. Fig 4.15 shows the wind speed and direction for Period2. The same pattern as in Period1 is seen here, with significantly higher winds modeled with WRF than measured at the Munch mast. For the last half of the period, the wind directions are similar, north-east, for the WRF and Munch data. For the first half, the Munch data have mostly wind from south to south-west. This may explain why the concentration at receptor 7 are lower for these days. Fig. 4.16 shows the values of L for the data sets for Period2. As for Period1, the conditions in the WRF water grid box are always unstable, while the WRF land data set is more variable, but mostly stable. The MO length calculated from the Munch data indicates mostly neutral conditions, but vary more with time than for Period1. All simulations tend to overestimate, compared to the passive sampler average concentration.

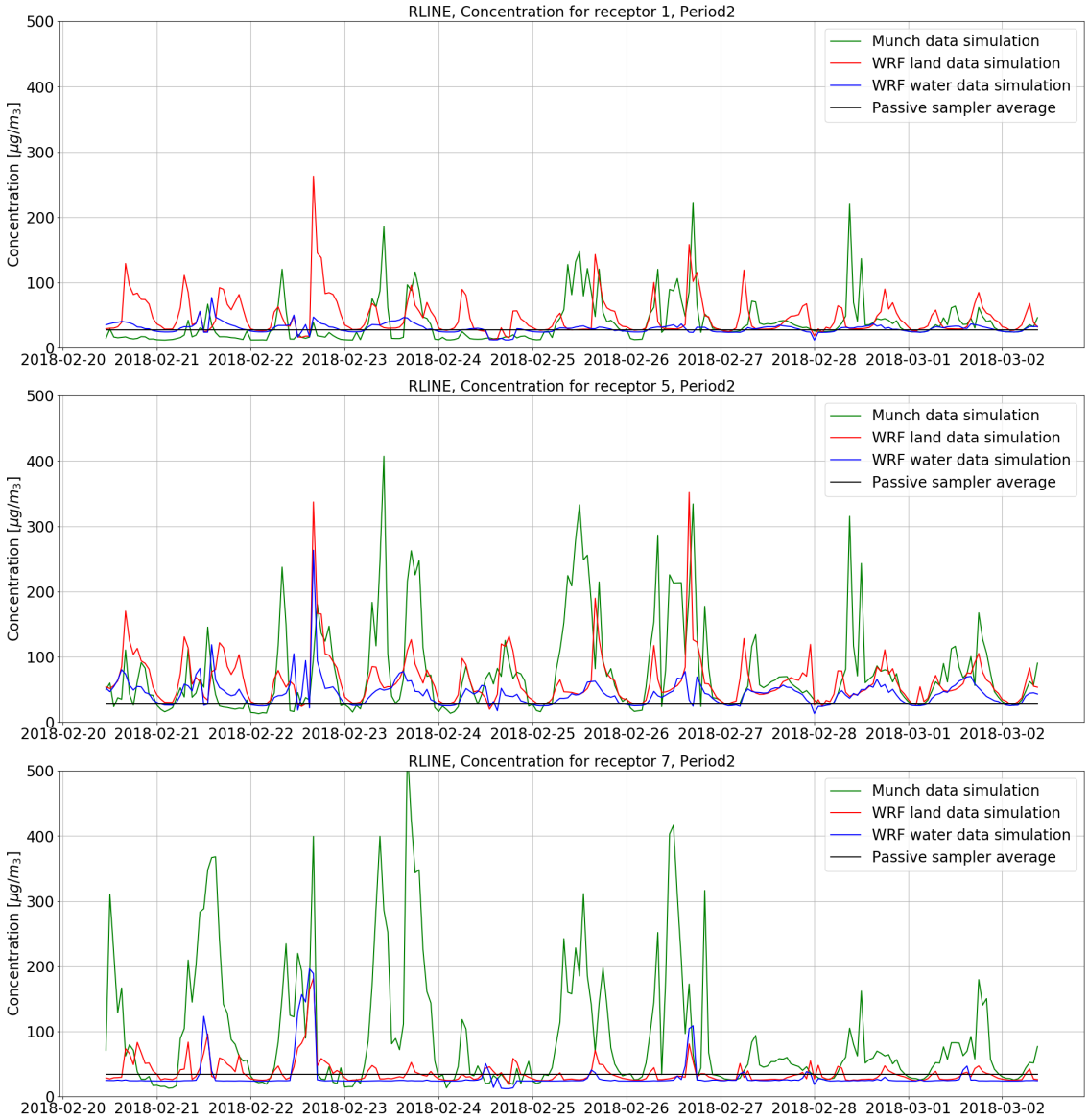

Figure 4.14: The plots show the hourly mean calculated concentrations from the RLINE simulations for receptor 1(top), 5(middle), and 7(bottom) for Period2. The concentration at the spike that exceeds the plot limit for receptor 7 is $535 \mu g/m^3$. The black line marks the average concentration measured by the corresponding passive sampler.

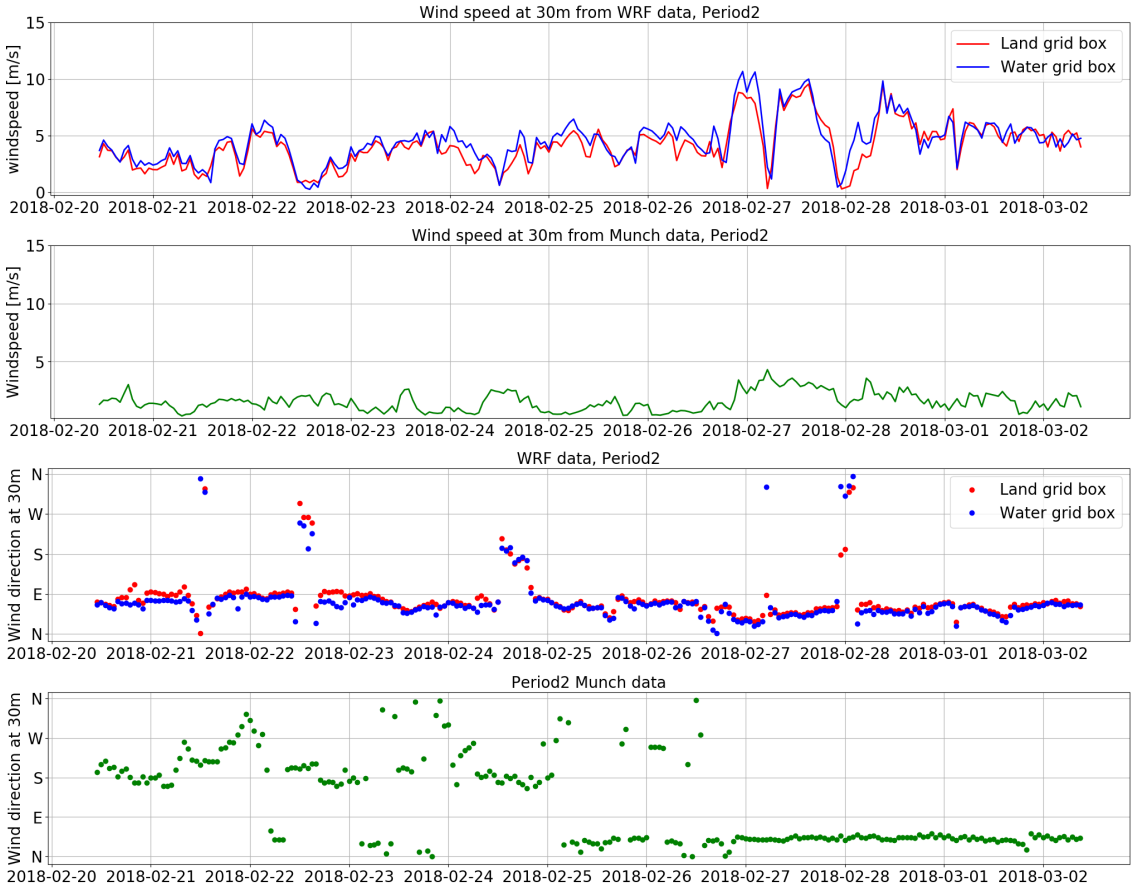

Figure 4.15: Wind speed and direction at 30m for Period2 from the Munch and WRF data sets.

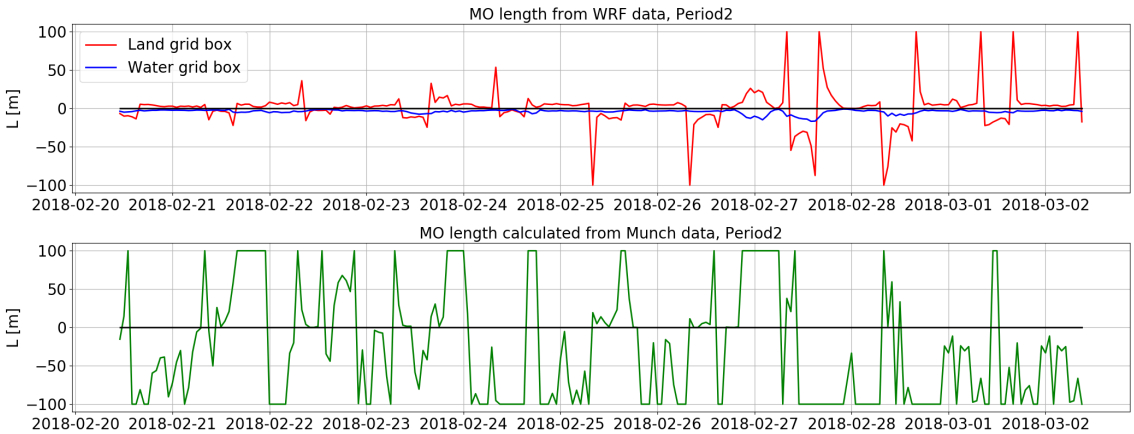

Figure 4.16: The top plot show the MO length, L, as calculated by WRF, while the bottom plot show the MO length values calculated based on the Munch data for Period2. Values above |L|=100m are set to L=± 100m, to better visualize the lower values. Hours with |L| above 100m is assumed to be neutral.

Hourly EPISODE results, Period2

Fig. 4.17 show the hourly results for Period2 for the receptor points 1,5 and 7 in the EPISODE simulation. Compared to Period1, there is less deviations between the two simulations. From 20.02.18-24.02.18 the WRF data simulation tend to give the highest concentrations, while for the remaining time the two simulations follow each other closely. This may be explained by the differences in wind speed and direction between the WRF data and the observed data. The WRF modeled wind from east will transport pollution towards the samplers. The wind speeds are lower for the observed meteorology, which often is connected to higher concentrations. However, these results indicate that the effect of the south to south-west winds are dominating over the wind speed effect in this case. Between 25.02.18 and 26.02.18, the winds measured at Blindern (Fig. 4.3) and Munch (Fig. 4.15) turns from south to north-east. The measured wind speed at Blindern also increases to magnitudes comparable to the modeled wind speed. Even if the same increase is not seen in the Munch data, it is likely that the calculated wind field for the simulation will catch some of the increase. The simulation result for these last days indicate that when the measured and modeled wind speed and direction and match, the calculated concentrations also tend to match each other. The largest difference between the two simulations is on the order of $60\mu g/m^3$. Following the above analysis, it is likely that this is mainly caused by the differences in wind direction. This illustrates the possible errors that can occur when using inaccurate wind data. Without information about the surface parameters for the Munch based simulation it is not possible to determine whether they are similar to the parameters from WRF. Such a comparison would have made it possible to evaluate the relative importance of the wind speed and direction compared to the surface parameters in the model.

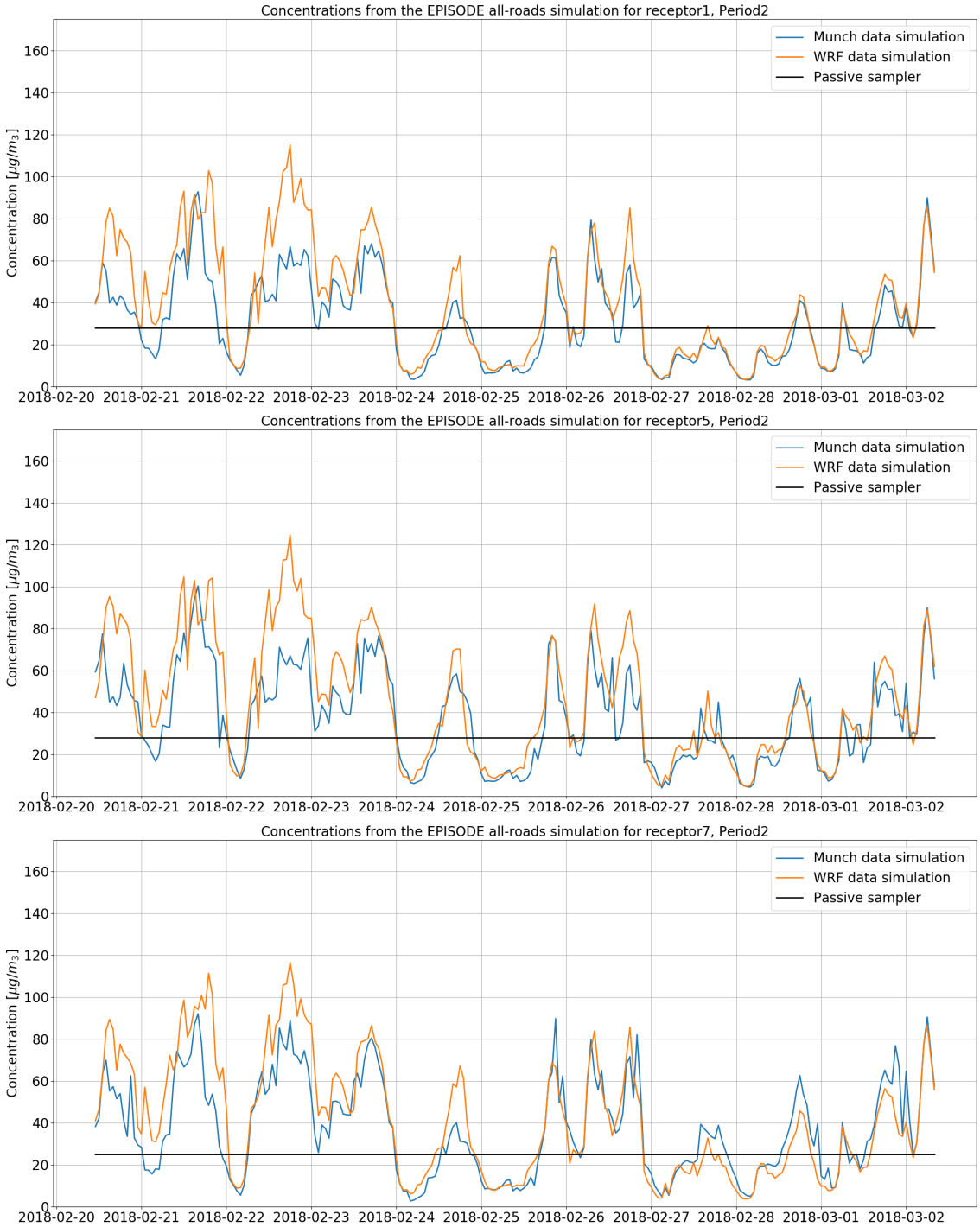

Figure 4.17: The plots show the hourly mean calculated concentrations from the EPISODE all-roads simulations for receptor 1(top), 5(middle), and 7(bottom) for Period2. The black line marks the average concentration measured by the corresponding passive sampler.

4.4.2 Comparisons with passive samplers, Period2

Fig. 4.18 shows the average concentrations of NO_2 from the simulations of Period2, together with the observed concentrations. Again, the slope of the gradient is in

good correspondence with the observations. The exception is the RLINE simulations, which tend to give a too steep gradient close to the road. The pattern of overestimation by the models is also seen here. Several simulations show good correspondence with sampler nr. 1. The RLINE water grid box simulation, the EPISODE all-roads Munch simulation and the two EPISODE KH5-only simulations give good estimations for this sampler. The deviation from the EPISODE KH5-only simulations and the passive sampler results are max $4\mu g/m^3$, and between 1-$2\mu g/m^3$ for receptor 2-6. This again indicates that it is KH5 and the background concentration that is influencing the area the most.

The EPISODE all-road simulations overestimates also in this period, but not as much as for Period1. The WRF based simulation gives concentrations of 10-$18\mu g/m^3$ above the observed, whereas the Munch based simulation is overestimating in the range 7-$12\mu g/m^3$, except for receptor 1, with only $2.3\mu g/m^3$ above the observed value. As opposed to for Period1, it is now the WRF based simulation that gives the highest concentrations of the EPISODE simulations. This is likely due to the wind effects discussed above.

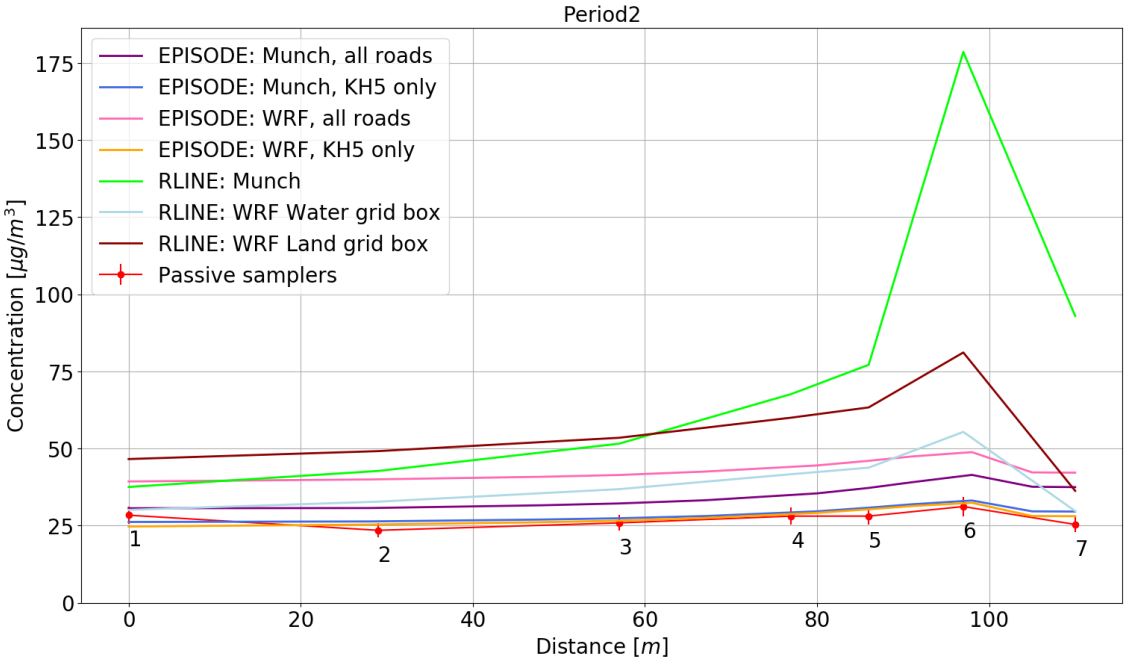

Figure 4.18: Averages based on the hourly calculated NO_2 concentrations for Period2, together with the observed result from the passive samplers. The figure shows the results from both the RLINE and EPISODE simulations.

4.5 Results for Period3

For Period3 no observations from the Munch mast was available. Hourly results for EPISODE are omitted, as there is no possibility of comparing simulations with modeled and observed meteorology input for this period. From the RLINE simulations, we can compare the results from the two grid boxes.

4.5.1 Hourly modeled results, Period3

Fig. 4.19 shows the hourly concentrations for receptor points 1,5 and 7 from the RLINE simulations for Period3. The pattern in these plots are significantly different from the first two periods. There are now several high concentrations calculated by the simulation based on the water grid box, while the land grid box simulation is generally predicting lower concentrations. For receptor 7, the concentrations are mostly just the background concentration for the last half of the period, but between 04.04.18-08.04.18, the winds from south to north-west, leads the transport from the road towards receptor 7. The wind direction and speed is plotted in Fig. 4.20. If we compare the wind speed plot with the receptor concentration plot, we see that the spikes in concentration often correspond to cases of low wind speed. The difference in wind speed and direction between the two grid boxes is about the same as for the two previous periods. This means that the reason for the switched pattern must lie somewhere else. Fig. 4.21 show the MO length for Period3 from the two data sets. Compared to the two previous periods, these values differ considerably. The stability in both boxes seems to follow a diurnal pattern. The land grid box stability seems to follow the more ideal, diurnal cycle presented in Section 2.1, while the water grid box stability is more or less opposite of this. The consequence of the increase of stable conditions for the water grid box are considerably higher concentrations, and that the diurnal emission variation is seen clearer also for receptor 1. The effect of stability is more discussed in Section 4.8.

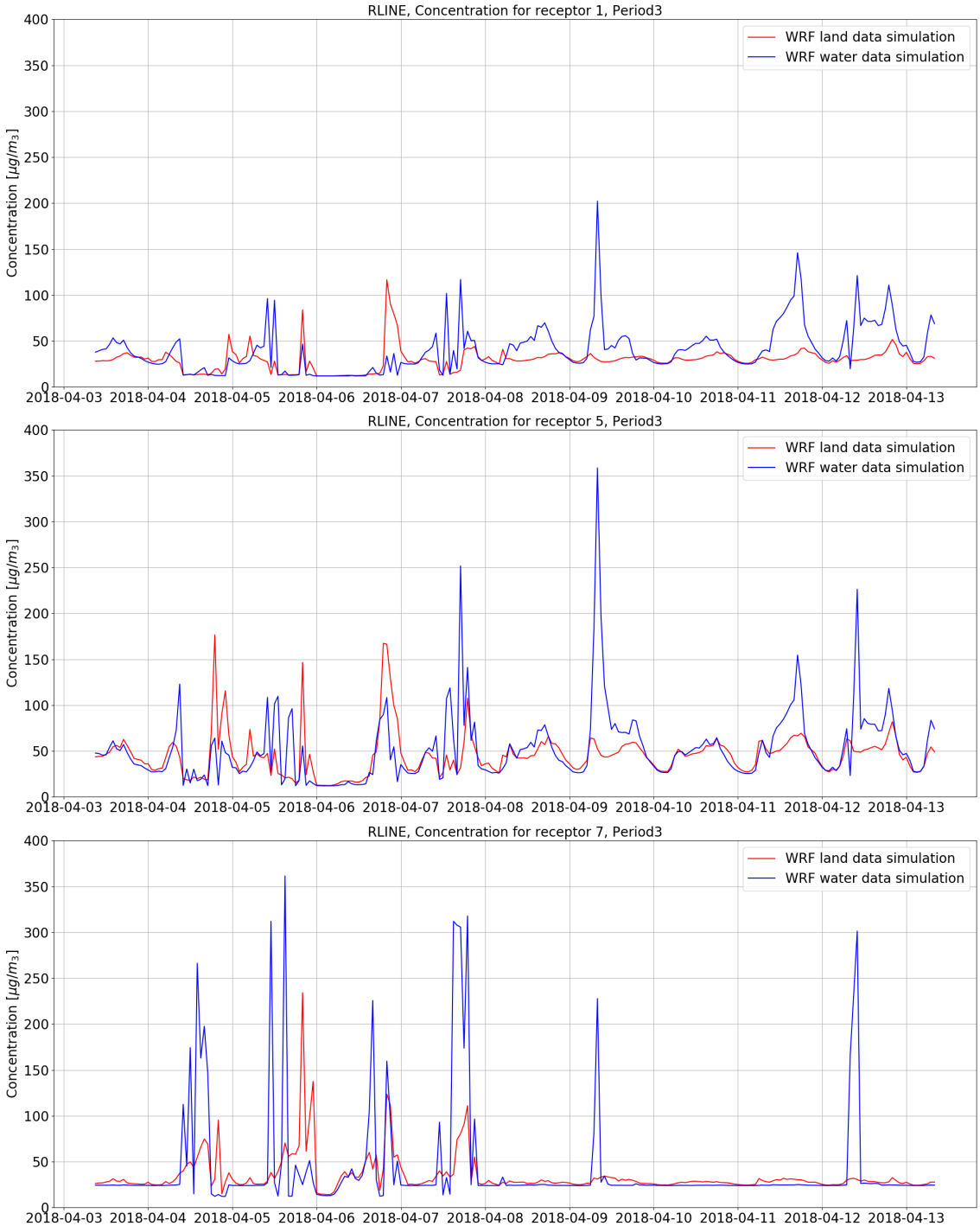

Figure 4.19: The plots show the hourly calculated concentrations from the RLINE simulations for receptor 1(top), 5(middle), and 7(bottom) for Period2.

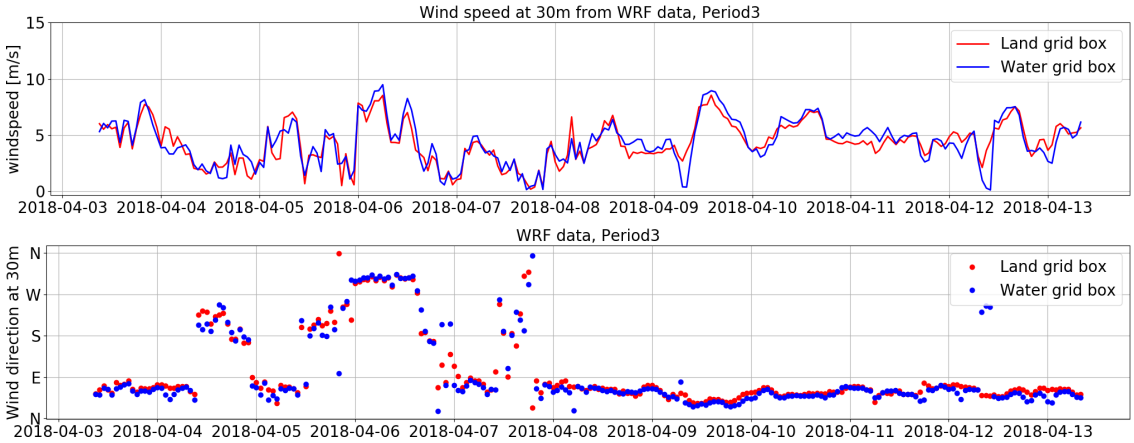

Figure 4.20: Wind speed and direction at 30m for Period1 from the WRF data sets.

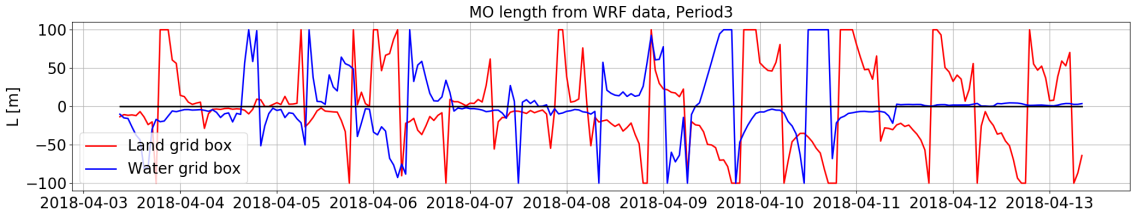

Figure 4.21: MO length, L, from the WRF data for Period3. Values above |L|=100m is set to L=± 100m, to better visualize the lower values. Hours with |L| above 100m is assumed to be neutral.

4.5.2 Comparisons with passive samplers, Period3

Fig. 4.22 shows the average concentrations calculated by EPISODE and RLINE compared to the result from the passive samplers. Both RLINE simulations are overestimating, but unlike the two previous periods, it is now the water grid box simulation that gives the highest concentrations. The KH5-only EPISODE simulation is underestimating with 4-6μg/m^3, except for at receptor 7, where it overestimates with 4μg/m^3. The EPISODE all-roads simulation is overestimating with 14-17μg/m^3, except for at receptor 7, where the overestimation is 24μg/m^3.

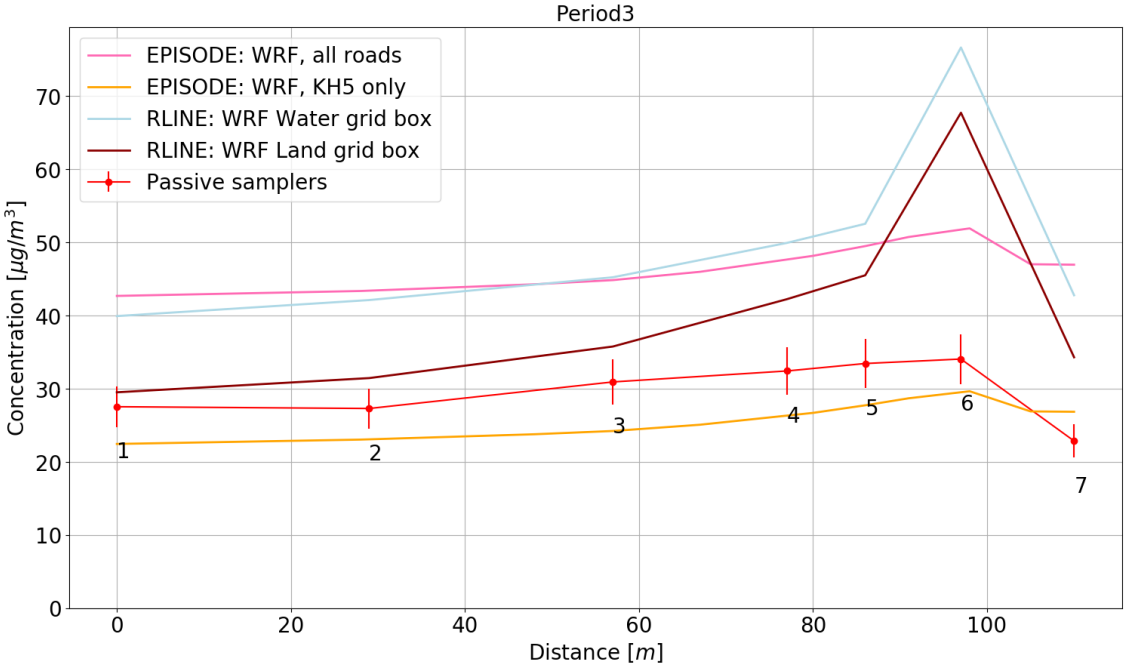

Figure 4.22: The figure shows the calculated average results for Period3 from the simulations from RLINE and EPISODE, together with the observed result from the passive samplers.

4.6 EPISODE results compared to hourly observations

Because the EPISODE domain covers a larger area than RLINE, and in addition is grid based, it is possible to compare the hourly EPISODE results to hourly measurements by air quality (AQ) stations in Oslo. Because Åkebergveien is closest to Bjørvika, it is assumed that the meteorological conditions here are most representative for our area of interest. The location of the Åkebergveien station is shown in Fig. 4.23. Scatter plots from the AQ stations at Manglerud and Hjortnes can be found in Appendix D. It should be noted that some of these results show a significantly lower correlation than Åkebergveien. An explanation may be that the station at Åkebergveien is close to the station at Grønland, where the urban background data is measured. It is likely that the concentration variations at Åkebergveien will follow the variation at Grønland to a greater degree than the other stations. In addition, at AQ stations further away, the area sources that was omitted in our simulations is likely to be a larger contribution.

The aim of this comparison is to investigate the performance of the model forced with observed or modeled meteorology on an hourly basis.

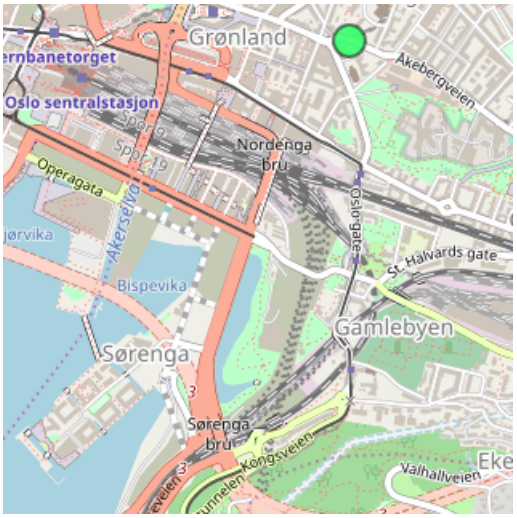

Figure 4.23: The green dot is showing the location of the air quality station at Åkebergveien in relation to Sørengkaia.

In the figures presented below, the statistical parameters Mean Bias (MB), Root Mean Square Error (RMSE) and the correlation coefficient are given. The equations defining these parameters are given in Appendix C. A positive MB means that the model tend to overestimate the concentrations. The larger the value, the larger the overestimation. The RMSE is the standard deviation of the prediction error, and is so a measure on the mean distance from the scatter points to the regression line. The correlation coefficient indicates the strength of the linear relationship between the modeled and observed data.

Fig. 4.24 shows comparisons of the hourly concentrations estimated by EPISODE, and the measured concentrations at Åkebergveien for Period1. Both simulations tend to overestimate the concentrations, with mean biases of 16.8μg/m^3, and 18.6μg/m^3, respectively. Both the RMSE and correlation coefficient show that the WRF data simulation is performing better than the observation based simulation. The same tendency was observed in the comparison with the passive samplers in Fig. 4.13, where the WRF simulations gave the smallest overestimation compared to the observations.

Fig. 4.25 shows comparisons of the hourly concentrations simulated by EPISODE, and the measured concentrations at Åkebergveien in Period2. Except for the correlation coefficient for the WRF based simulation, the statistics are better than for Period1 for both the simulations. However, as opposed to Period1, the simulation based on observed meteorology show the best correspondence with the observations. This is also the same tendency as was observed in comparison with the passive samplers in Fig. 4.18.

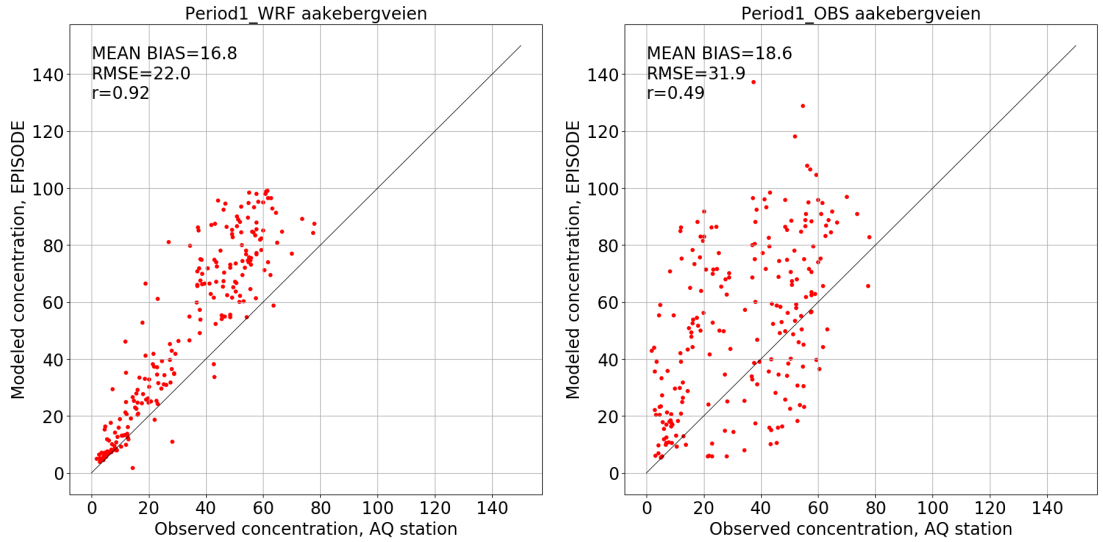

(a) **(b)**

Figure 4.24: Scatter plots of the correspondance between the EPISODE all-roads simulations and the observed concentration at the air quality measurement station at Åkebergveien for Period1. In panel (a) WRF meteorology is used, panel (b) uses observed meteorology from the Munch mast and the other meteorological stations described in Table 3.5.

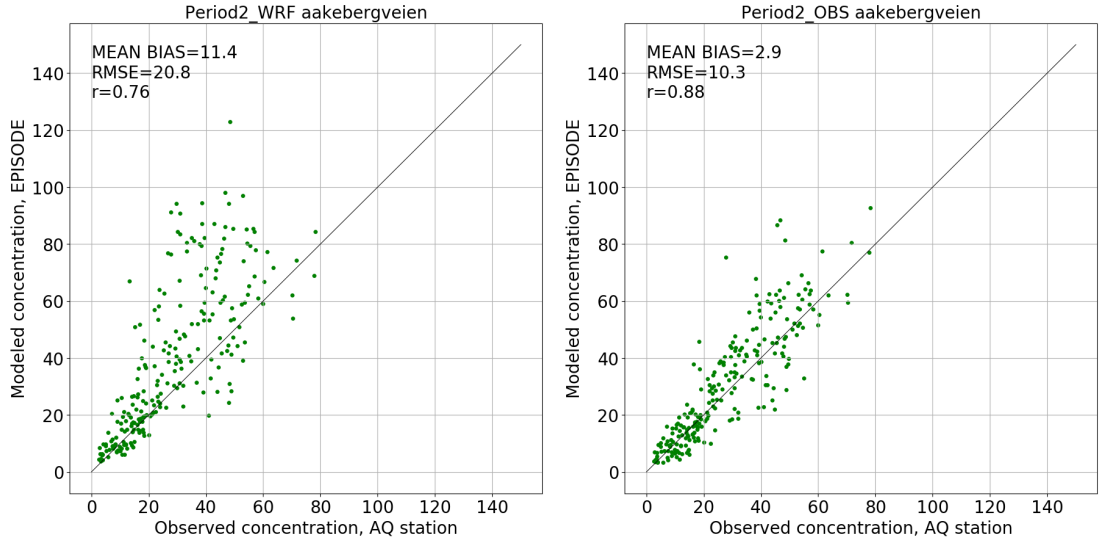

(a) **(b)**

Figure 4.25: Scatter plots of the correspondance between the EPISODE all-roads simulations and the observed concentration at the air quality measurement station at Åkebergveien for Period2. In panel (a) WRF meteorology is used, panel (b) uses observed meteorology from the Munch mast and the other meteorological stations described in Table 3.5.

Fig. 4.26 shows the correspondence between the EPISODE WRF simulation and observations at Åkebergveien for Period3. The RMSE is about the same as for the two other periods, but the correlation coefficient is the lowest of the three.

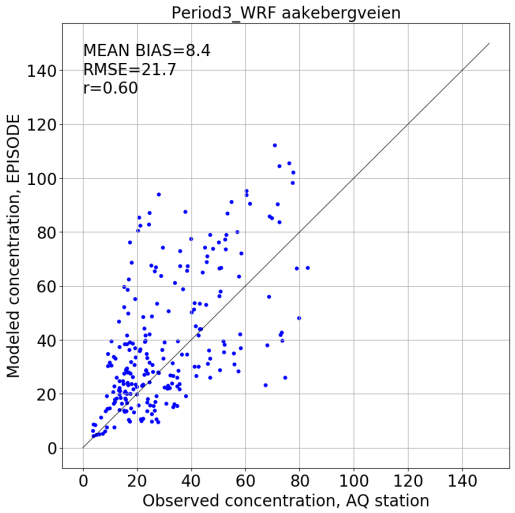

Figure 4.26: Scatter plot of the correspondance between the EPISODE all-roads simulation with WRF meteorology and the observed concentration at the air quality measurement station at Åkebergveien for Period3.

Based on the results in Fig. 4.24-4.26 it is not possible to make a general conclusion on weather that modeled or observed meteorology was better at predicting the NO_2 concentrations. As we have seen, the modeled and observed wind speed and direction often differ significantly in the data used in this study. This is likely to explain some of the deviations between the simulations based on modeled and observed meteorology. All simulations show positive biases, which might indicate that there are more mixing in reality, than what is captured by the meteorological input. The initial turbulence caused by the vehicles are a factor of uncertainty here, and it is possible that the values of σ_{y0} and σ_{z0} are not representing the actual mixing accurately. It might also be that the emissions used in the models are too high compared to reality.

4.7 Sensitivity tests

In this section sensitivity tests for some of the most important meteorological and surface parameters will be presented. The parameters were challenging to estimate and measure, and it was therefore of interest to investigate their relative importance in the calculations. The sensitivity tests has been performed with RLINE only, as it is easier to manipulate the input data for this model than for EPISODE. It should be noted that the dispersion equations used in RLINE are only one alternative of many. This means that the results found in this section not necessarily will match the findings based on the same type of tests with another model. The tests have been performed for Period1, as this is the only period for which full data sets for

both WRF and Munch data are available. The aim is to quantify the effect of the different meteorological parameters on the dispersion calculations.

4.7.1 Sensitivity test for PBL heights

As described in Section 3, RLINE was run with several different parameterizations of the planetary boundary layer height with the Munch data. The different alternatives are plotted against time for Period1 in Fig. 4.27. The Venkatram formulation and the PBLH from WRF show a similar pattern, with the PBLH tending to give some higher values on average.

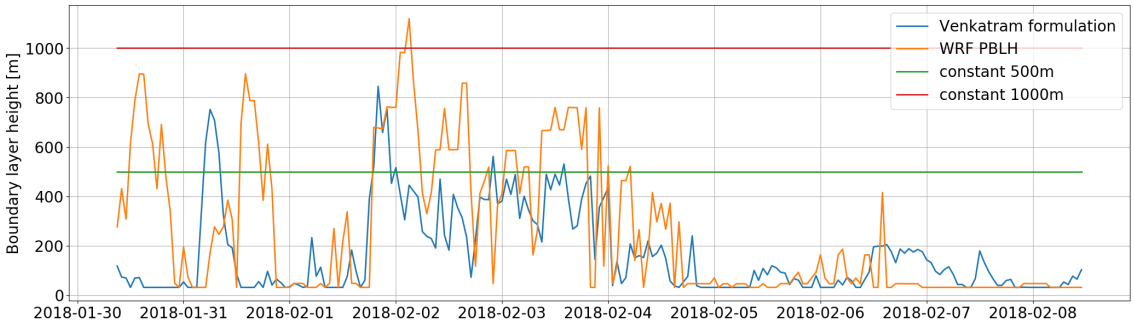

Figure 4.27: Variation of the planetary boundary layer with time for Period1, with different alternatives for estimating the height.

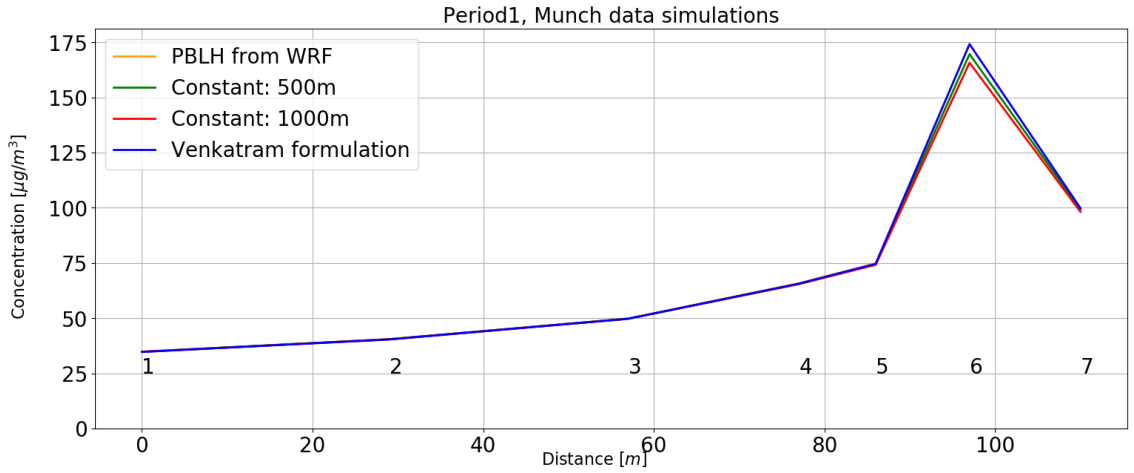

Figure 4.28: The average NO_2 concentration gradient calculated from RLINE simulations for Period1, with different methods of defining the PBLH height. The numbers indicate the location of receptors 1-7. The yellow "PBLH from WRF" line is completely covered by the blue "Venkatram formulation" line.

Fig. 4.28 shows the average concentrations for Sørengkaia from the RLINE simulations for Period1. As is evident from this plot, the definition of the PBL height does not have a big influence on the result, except for when the concentrations are very high, closest to the road. At receptor point 6, the lowest concentration (Constant

1000m) is only 5% lower than the highest concentration (Venkatram formulation). In the model, the PBL height is used as a limit to the vertical dispersion parameter, σ_z. If the vertical dispersion parameter calculated from Eq. (2.38) and (2.39) is larger than $\sigma_{z,max} = \sqrt{\frac{2}{\pi}} z_{mixed}$, the latter is used instead of σ_z. The results of the runs shown here, indicate that the calculated dispersion parameter generally is smaller than $\sigma_{z,max}$, so that the height of the boundary layer is of minor importance in these simulations, where the receptor points are located close to the road. The small difference we see close to the road reveals an expected pattern, where the highest PBL height yields the lowest concentrations. This is expected because there is more room for mixing when the boundary layer is higher. However, it is unclear why the difference is only evident close to the source. Following Eq. (2.38) and (2.38), $\sigma_z \propto x$. It would therefore be expected that $\sigma_z > \sigma_{z,max}$ is more likely to happen further away from the road.

For simplicity, based on the relatively small difference between the simulations, only the results based on the Venkatram formulation have been presented in the previous sections. This formulation was chosen because it is also used in AERMET surface files, which, as mentioned earlier, is the input RLINE was designed for.

4.7.2 Sensitivity test for wind speed

As we have seen in the previous sections, the wind speed modeled by WRF is generally higher than the wind speeds measured at the Munch mast. Based on this, it was decided to run a simulation where the wind speed from the Munch data was multiplied with a factor 3, so it would be of the same magnitude as the WRF water data. Due to the dependence in the equations, this increase also affect L and u_*, which in turn affect w_* and z_{im} in the calculations. The average result from the simulations is compared to the original runs in Fig. 4.29. We see that instead of overestimating for all receptors, the model underestimates at receptor point 1 with ca. $11\mu g/m^3$, and at receptor point 2 and 3 with ca. $8\mu g/m^3$. The modeled result match well with receptor 4 and 5. The overestimation of receptor point 6 is significantly lower than for the original simulation. Instead of an overestimation of $135\mu g/m^3$, it is now $36\mu g/m^3$ which is in between the concentrations from the WRF runs. The gradient outwards from the road is also less steep than for the original runs. By increasing the wind with a factor 3, the reduction in concentration for the seven samplers are in the range 38%-57%.

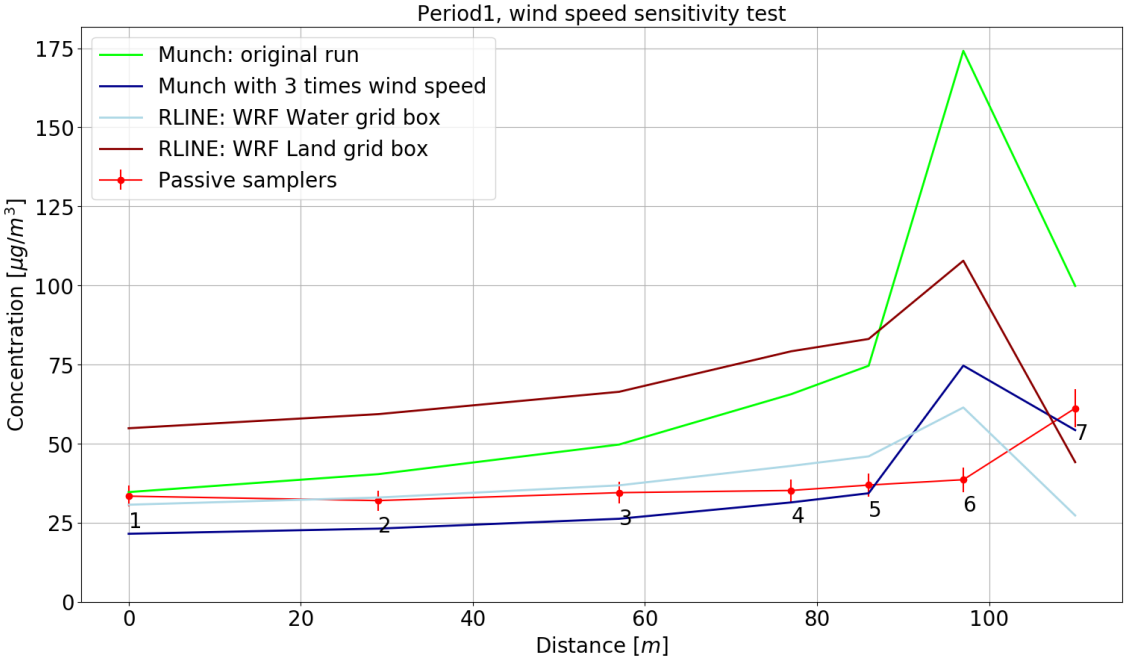

Figure 4.29: The average NO_2 concentration gradient calculated from RLINE simulations for Period1. The dark blue line represent the simulation with 3x the wind speed. The original simulation, the WRF based simulations and the sampler observations have been added for easier comparisons. The numbers indicate the location of receptors 1-7.

The large difference in wind speed between the observed and modeled meteorology illustrates the challenges of obtaining trustworthy values of wind near the surface in an urban boundary layer. As discussed in Section 2.1.5, the wind profile below $d + z_0$ is often affected by very local factors, like the placement of buildings and the spacing between them. It is also likely that formation of internal boundary layers will occur when air flows from the fjord with lower roughness, towards the city with higher roughness which will also alter the wind profiles in the area.

The Munch mast is located within a radius of 400m from the sampler location, but due to local disturbances, the observations may not be representative of the conditions at Sørengkaia. Especially the proximity between the meteorological sensors and the Munch museum is suspected to disturb the measurements when the wind blows from the east. This is problematic in relation to the passive sampler measurements, for which easterly winds will place the samplers downwind from KH5. If these wind conditions are not captured well in the measurements, it can lead to possible large errors in the dispersion calculations.

In a model like WRF, the challenge is to resolve the effects of the city in a satisfactory manner. Based on the high wind speeds predicted by the model, it is likely that the drag effects of the city are not represented properly with the model setup used in this study.

4.7.3 Sensitivity test for surface roughness length

The surface roughness length for the Munch data set was determined from Eq. (2.25), using the roughness elements from the area in Fig. 3.7. However, the wind and temperatures were measured at the Munch mast. This area might be more affected by the surrounding buildings, and a higher surface roughness value may be more appropriate. It was therefore decided to increase $z_{0,urban} = 0.87m$ with a factor 1.5, so that $z_{0,urban,new} = 1.305m$. The result of this simulation is shown in Fig. 4.30. The difference between the original run and the one with increased z_0 is between 4%-8%, and the shape of the two gradients are similar. This indicates that the choice of z_0 have some impact on dispersion calculations in this study. However, as was pointed out in Section 4.3, and will be further discussed in Section 4.8, the effects of the stability conditions seems to dominate over the effect of the roughness length.

In the modeled meteorological data from WRF it was not possible to change the assigned surface roughness for the grid boxes. A model setup in which it is possible to prescribe the surface roughness for the area of interest would have been useful to better represent the area where the dispersion happens.

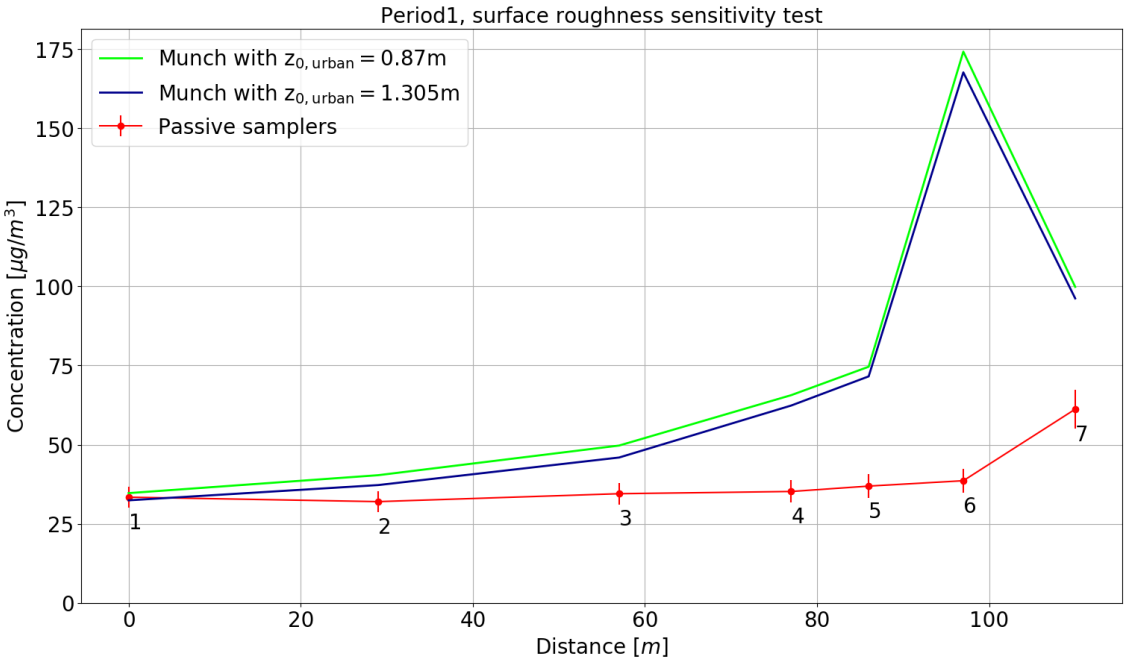

Figure 4.30: Average NO_2 concentrations for Period1. The results for the original RLINE simulation and the simulation with increased $z_{0,urban}$ is plotted, along with the results from the passive samplers.

4.7.4 Sensitivity test for near-parallel wind directions

As we saw in Fig. 4.11, RLINE tend to overestimate concentrations when the wind direction is close to parallel to the road, especially for stable conditions. Therefore, a simple test of the impact of near-parallel wind direction was done. Averages were calculated after all hours with wind directions within 20° of the line source were

removed, regardless of the wind speed and stability conditions. 64 of 218 hours were removed. The result is plotted in Fig. 4.31. As expected, the largest decrease is seen for the receptors close to the road, as these are most affected by the effect of the parallel winds. At receptor 1, the concentration based on all hours is ca. 10% higher than the modified average. At receptor point 5, 6 and 7, the difference is 15%, 32% and 23%, respectively. The examples presented in Table 4.2, indicate that the problem is most evident in stable conditions. The problem with parallel winds in the approximation of line sources with Gaussian point sources is an issue regardless of what meteorological input that is used. However, the simulations in EPISODE do not show the same sensitivity to wind direction as RLINE.

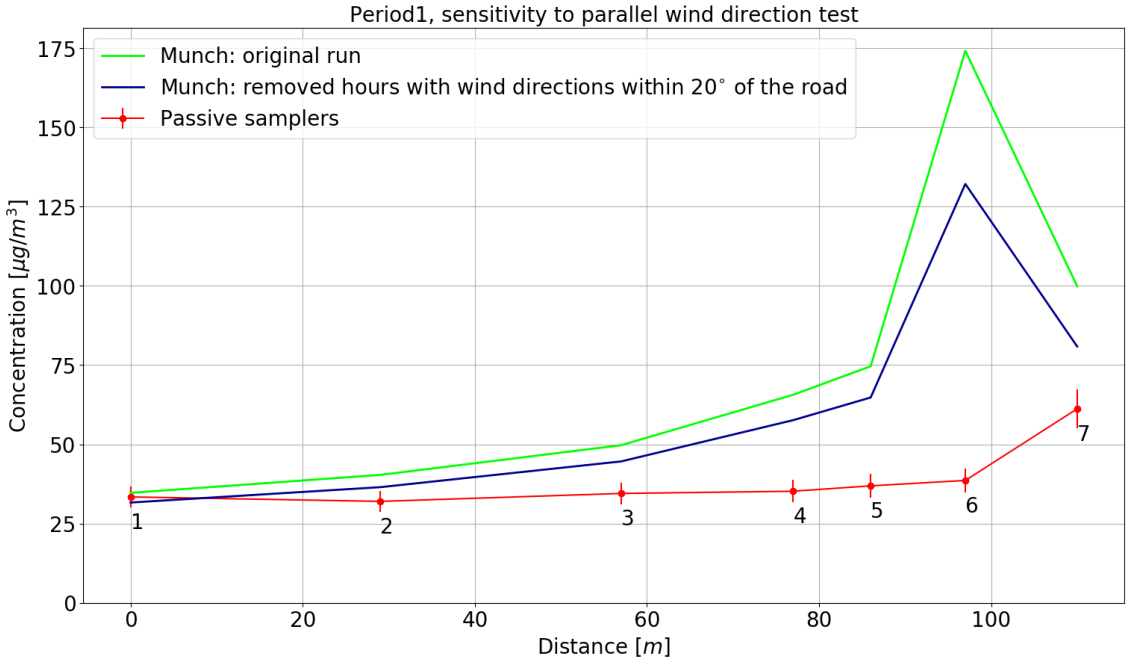

Figure 4.31: Average calculated concentrations of NO_2 for receptor 1-7, along with the measured averages of the passive samplers. The green line represents the original simulation. The green is the average based on the remaining hours, after hours with close to parallel winds are removed.

4.8 The importance of atmospheric stability

In this section a discussion on the importance of stability will be presented. The discussion is based on stability parameters for Period1 and Period3 for the RLINE simulations, as the meteorological data sets show significantly different conditions. As discussed in the theory chapter, the stability of the atmosphere is a key factor in dispersion calculations. In the below discussion, the PGT stability classification is used as a tool to illustrate the stability conditions in the different data sets. It should be kept in mind that the actual dispersion formulation is a continuous function of L (through the dispersion parameters), and are not determined by discrete stability classes. Below, the meteorology from the Munch data, WRF water data and WRF land data have been classified based on the limits for the Richardson number in

Table 2.2 and for 1/L in Fig. 2.2. For the 1/L classification, the limits were found based on the respective surface roughness of the data. Because we were unable to find Ri limits for other roughness lengths, the values from Mohan and Siddiqui [1998], for a $z_0 = 0.1m$ were used. This introduces some uncertainty, but the result still give an indication of how the stability distribution will be, based on the Richardson number. The Richardson numbers are calculated from Eq. 2.8 by using the differences between the wind speed and potential temperature at 10m and 30m height. Fig. 4.32 shows the stability classifications for Period1.

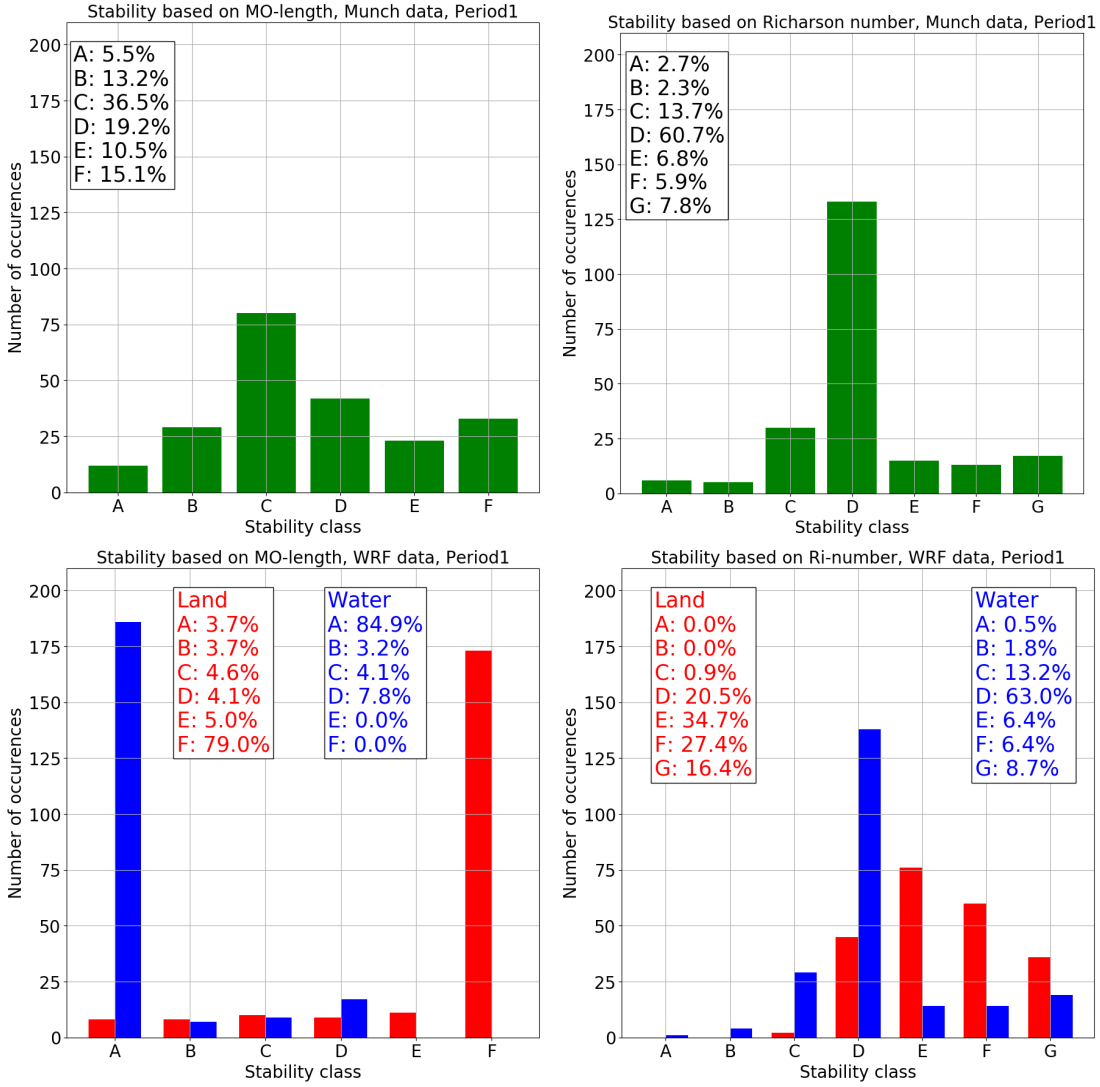

Figure 4.32: Stability classifications based on MO length (left) and Ri number (right) for Period1. The top figures are based on the Munch data, and the bottom figures are based on WRF data.

The MO length for Munch data are calculated based on the Richardson number (with the equations from Section 2.1.3). Therefore, it is expected that the two methods of classification will give a similar stability distribution.

The MO lengths in WRF is calculated directly from the definition, Eq. (2.11) with surface variables that are parameterized by the PBL and surface layer schemes

in the model. When the stability is classified based on MO length, the two WRF grid boxes show almost completely opposite distributions, the land grid box is almost always stable, while the water grid box is almost always unstable. In the WRF simulations, the sea surface temperature (SST) is constant, SST=276K (see Borander's master thesis). The modeled air temperatures were generally colder than 276K in Period1, leading to heating from below (positive $\overline{w'\theta'}$) and therefore probably contributing to the unstable conditions in the water grid box.

The average results from the RLINE simulations have been plotted again in Fig. 4.33 for convenience. Except for receptors 6 and 7, the Munch data simulation, which are mainly neutral to slightly unstable (stability class C and D), calculates concentrations in between the more extreme cases of the WRF data. The deviation from this pattern for receptor 6 and 7 may be explained by the sensitivity to wind speed close to the source, as discussed in Section 4.29. The concentrations calculated based on the stable land grid box data is ca. 80% higher than the concentrations calculated with the unstable water grid box data.

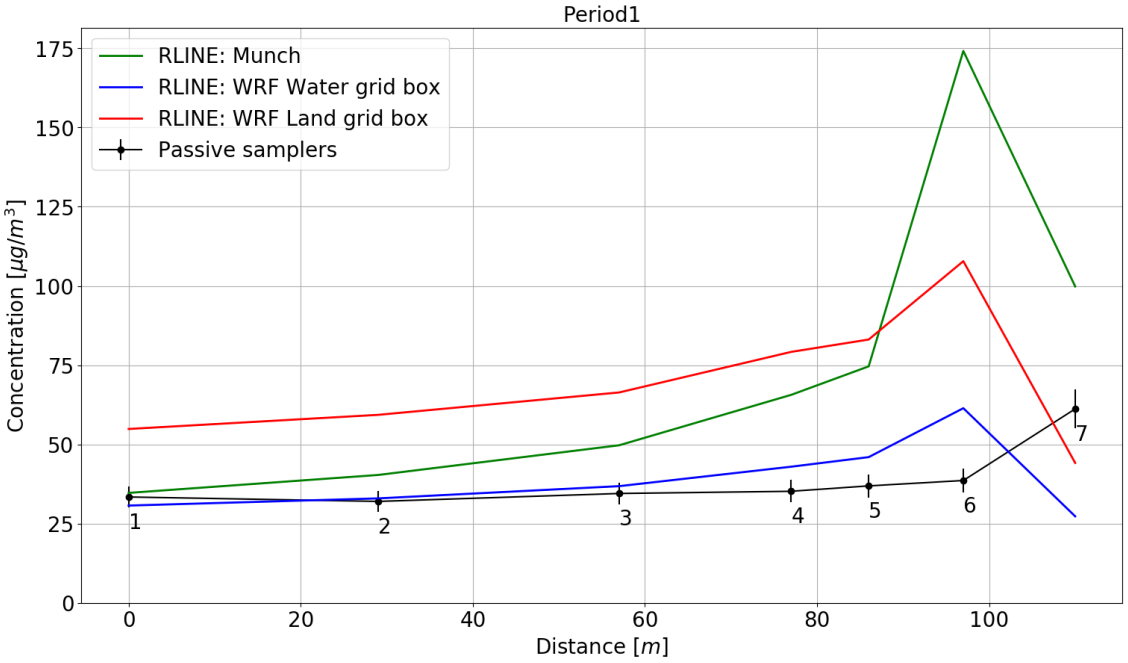

Figure 4.33: Calculated average results for Period1 from the simulations from RLINE, together with the observed result from the passive samplers.

Fig. 4.34 show the stability classification based on MO length and Richardson number for the WRF data for Period3. These distributions are significantly different from the ones in Fig. 4.32. For the classification based on MO length, both grid boxes now have a significant amount of hours in each class, with a slight overweight in class D for the water grid box. This change is probably caused by the the warmer air temperatures in April than in January/February. The heat flux is now more affected by the diurnal heating and cooling of the terrestrial surface, which leads to a more even distribution over the stability classes. For the classification based on Richardson numbers, the distribution for the land grid box now has more unstable cases, while the water grid box distribution is similar to Period1. The RLINE

simulations for Period3 are plotted again in Fig. 4.35. For Period3 it is the water grid box simulation that gives the highest concentrations, while the land grid box simulation calculates concentrations within 15% of the observations for the first three samplers. The concentrations based on the WRF water grid box is now ca. 30% higher than the simulation based on the land grid box, except for receptor 5 and 6, where it is ca. 15% higher.

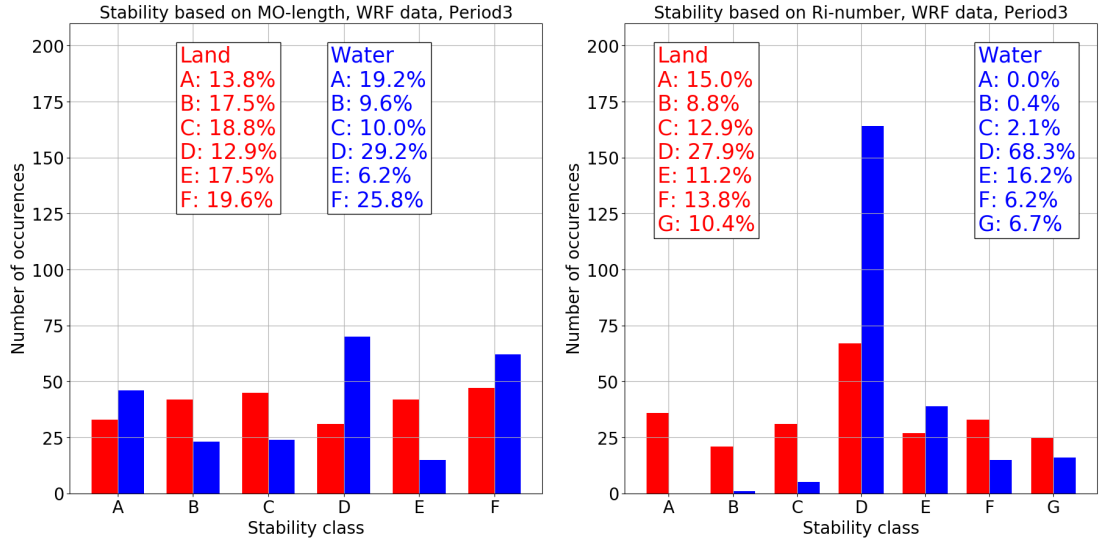

Figure 4.34: Stability classifications based on MO length (left) and Ri number (right) for Period3.

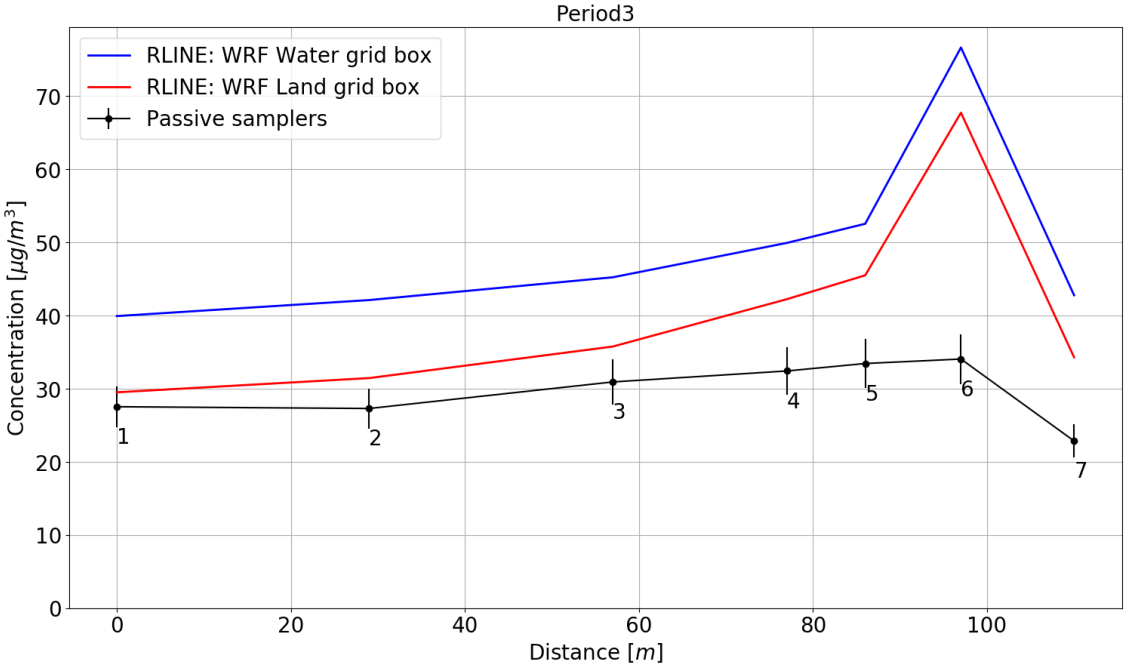

Figure 4.35: Calculated average results for Period3 from the simulations from RLINE, together with the observed result from the passive samplers.

The comparison of the stability and the concentrations of the two periods indicates the importance of considering the stability in the dispersion calculations.

The differences among the data sets also illustrates the challenges of determining stability, both from observed data, and from modeled data. The data from the two WRF grid boxes gave significantly different stability conditions. This reflects the extra challenge when modeling an area close to the waterfront, like in Bjørvika.

The determination of L from the Bulk Richardson number is an approximation. The Ri number was calculated based on wind and temperature differences at 10m and 30m. This gives an indication of the stability in this layer, but this may not be representative of the conditions closer to the ground. A better experimental approach would be to measure the surface heat flux and friction velocity directly, which would give a more realistic view on the near ground stability conditions. This would also make it possible to validate modeled surface fluxes, which would help when evaluating if modeled meteorology is a good alternative in dispersion calculations. The findings in this section indicates that thermal instability,determined by the surface heat flux, have a larger impact on the dispersion calculation than mechanically induced turbulence connected to surface roughness and frictional velocity. This suggests that accurate knowledge about the stability conditions are important for good results in the dispersion calculations.

4.9 General discussion of the results

The slope of the averaged concentration gradients from the EPISODE simulations matches the slope of the observed concentration gradients well for all periods, regardless of the meteorological input data. This is indicating that the actual spread from KH5 are well simulated by the model.

In cases with close to parallel winds and calm conditions, RLINE tend to overestimate the concentrations at the receptor points close to the source significantly. This contributes to the steeper gradient we see for the period averages. The model generally performs better for the receptors furthest away from the source.

It is difficult to point to specific reasons for the general overestimation in the simulations, as it is probably a consequence of several of the uncertainties present in this study. Some may be explained by the meteorology. As has been shown in the sensitivity tests, the alterations of different variables have generally decreased the calculated concentrations in RLINE. This suggests that with more accurate meteorological data, we may obtain better results with the model.

Other factors than meteorology are also likely to have an impact. In a study by Briant et al. [2013], two Gaussian plume models were compared to NO_2 concentrations measured with passive diffusion tubes in Paris. Here, the models tended to underestimate the concentrations, for both summer and winter conditions. They mention uncertainties in emission factors, NO_X chemistry and uncertainties in the passive samplers as possible explanations. Although the effect is reversed in this study, some of the reasons for the overestimation may lie in the same factors. As we have seen from the EPISODE simulations, the results with the closest fit to the sampler observations were the ones using only line sources that represent KH5, and not the whole road network, in addition to the background concentration. Also the

comparison with Åkebergveien showed positive model bias. This may indicate that the emission setup may overestimate the contribution from other line sources.

The estimation of background data is also an uncertain factor, in both models. For EPISODE, it is difficult to know how much impact the assumtion of including the area sources in the background emissions have for the resulting concentrations.

Also the chemistry may play a role. Both models use simplifying assumptions for the chemistry, which is likely to give errors in the concentrations. The assumption that $NO_2 \approx NO_X$ is likely to contribute to the overestimation. From Section 2.3, we know that most NO_X is emitted as NO. The conversion time for NO is longer in cold temperatures. A calculation based on conditions typical of Oslo in winter time, indicate a conversion time of ca. 2.8min (see Appendix C). It is therefore likely that the conversion to NO_2 is not completed close to the road in reality, while in the models we have assumed that the conversion happens instantly.

To arrive at the results presented in this chapter, many assumptions have been made along the way. This needs to be kept in mind when drawing conclusions from the findings. Uncertainties in everything from equations to measurement techniques introduces errors in the calculations. When evaluating results that are based on data with various sources of error, there is a possibility of compensating errors. For example, if one error source leads to overestimation, and another leads to underestimation the output can look correct, but is really the effect of the compensating errors.

4.10 Suggestions for future studies

Based on the lessons learned from this study, some suggestions for future work are presented.

To better isolate the effect of meteorology on dispersion, it is suggested to observe the dispersion of an inert tracer not naturally present in the area. This will remove the uncertainties linked to background concentrations and chemical reactions. Controlled emissions of a tracer will also remove the uncertainties of emission rates from the roads.

The passive sampling method that was used for observations in this thesis is a good alternative for monitoring concentrations over time. But as we have seen, both the concentrations and meteorological conditions change rapidly, and hourly observations would be better to capture the effect of these changes. This would also have made it easier to extract data for certain conditions, like low wind speeds and stable conditions, from the simulations. That would have made it possible to compare the performance of the modeled and observed meteorology runs for specific conditions.

Based on the findings in this study, the wind speed and direction, and the stability conditions seems to be most influential on the dispersion calculations. Therefore, it is suggested that extra care is taken when obtaining these data. Instead of calculating L based on parameterizations, like has been done here, direct measurements of the surface fluxes is desirable. That way, the MO length, which is used in both models to determine the stability could be determined more exact. Comparison of

these fluxes to those parameterized in a model would also give useful information about the accuracy of the model meteorology for these purposes.

Modeling wind in an urban area will always be a challenge, but using a model set up with finer resolution, and possibly a more refined urban scheme is likely to give better results than what was obtained here. Measuring wind in an urban area is also a challenge, and measurements from a more undisturbed site would probably give better results. In addition, it would be interesting to perform the meteorological measurements as close to the pollution measurements as possible. This is to minimize the chance of local factors affecting one of the measurements, but not the other.

Chapter 5

Summary and conclusions

In this study, observations of NO_2 concentrations with passive samplers have been performed along Sørengkaia in Oslo, for three different periods in the winter and spring of 2018. The samplers were placed perpendicular to the road Kong Haakon 5. gate (KH5). The results of these measurements have been compared to simulations by the air pollution dispersion models RLINE and EPISODE. The models have been run both with observed meteorological data, and meteorology modeled by the numerical mesoscale model, WRF (Observational data was not available for the last sampling period).

The EPISODE model was run with two types of emission setups. One which included urban background concentrations and a road network covering the entire Oslo region, and one with background concentration and only emissions from KH5. All simulations with EPISODE were able to estimate the concentration gradient outwards from the road well. The simulations based on the whole road network tended to overestimate the concentrations, while the ones with only KH5 generally had a good match with the observations. This indicate that KH5 is the main contributor to NO_2 in this area, in addition to the background concentrations. For the all-road simulations, the WRF based run performed best in the first period, while the observation based simulation performed best in the second period. The same pattern was also seen when comparing the hourly simulated concentrations to measured concentrations at the AQ station at Åkebergveien. Based on this, it was not possible to conclude on whether the use of observed or modeled meteorology lead to better performance of the model.

The RLINE simulations were run with three types of meteorological input; WRF data from a grid box defined as land, WRF data from a grid box defined as water, and locally observed meteorological data. The simulations based on the three data sets deviated considerably from each other which is reflecting both the differences in the meteorological data sets, and also the model's sensitivity to input data. The model performed best for the receptors furthest away from the road. For Period1 and Period2, the simulation with data from the WRF water grid box was the closest match to the observations, while the simulation with WRF land data gave the largest overestimation furthest from the road. Close to the road, the simulation with observed meteorology gave the highest overestimation. For Period3, simulation with data from the WRF water grid box gave the largest overestimation, while the

WRF land grid box gave fairly good results for the three receptors furthest from the road. Due to these large variations between the data sets, it was not possible to make a general conclusion on which meteorological data set that lead to the best performance.

Sensitivity tests were performed in RLINE to investigate the importance of different parameters. The wind speed in the Munch data set was increased by a factor 3, to match the magnitude of the modeled winds from WRF. This lead to a 38%-57% decrease in concentrations for the different receptors. This indicates large impact of wind speed on dispersion calculations, and emphasizes the need for good quality wind data when modeling dispersion.

A comparison of the stability conditions from the data sets for Period1 and Period3 indicates that the thermal instabilities caused by heating and cooling of the surface is of greater importance than mechanically generated turbulence in the area. This emphasizes the need for more accurate determination of the stability parameters.

The planetary boundary layer height was defined in four different ways, to test the importance for these dispersion calculations. The largest difference between the runs was 5%, which indicates that the height of the boundary was of minor importance in these simulations. To test the impact of surface roughness, we chose to increase the urban surface roughness with a factor 1.5 This lead to a 4%-8% decrease in concentrations from the original simulation, which indicates that the surface roughness also is of minor importance.

As described in the theory chapter, more or less every surface layer parameter are challenging to either measure or parameterize. Therefore, it is valuable to know what is affecting the dispersion the most. Based on the results of the sensitivity tests, it is suggested that focus on increasing the quality of wind and stability data will be most rewarding in terms of increased model performance, compared to focus on PBL height and characterizing the surface roughness. Based on the findings in this study, several improvements to the experimental setup have been suggested. Some of these suggestions are both resource demanding and expensive, and will therefore require a willingness to further invest in this area of research.

Appendix A

Hovin comparison, last night of Period2

The plots show data from the meterorological station at Hovin from the night between 28.02.18 – 01.03.18 (Night1) and 01.03.18 – 02.03.18 (Night2) The data are downloaded from `www.eklima.no`.

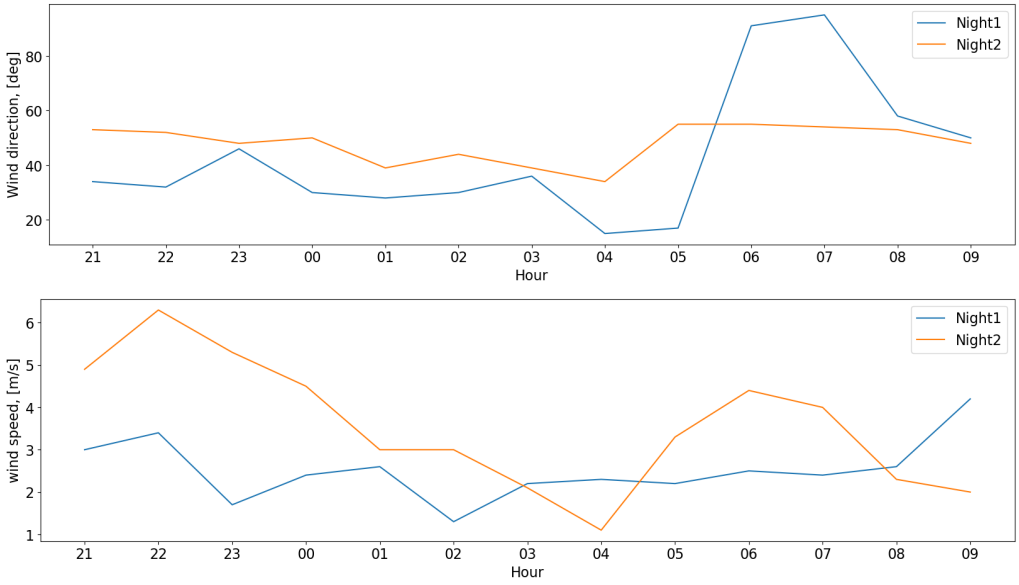

Appendix B

Factor curves

M2 Hovedveg i bystrøk med arbeidsreiser og gjennomgangstrafikk

Årsvariasjon

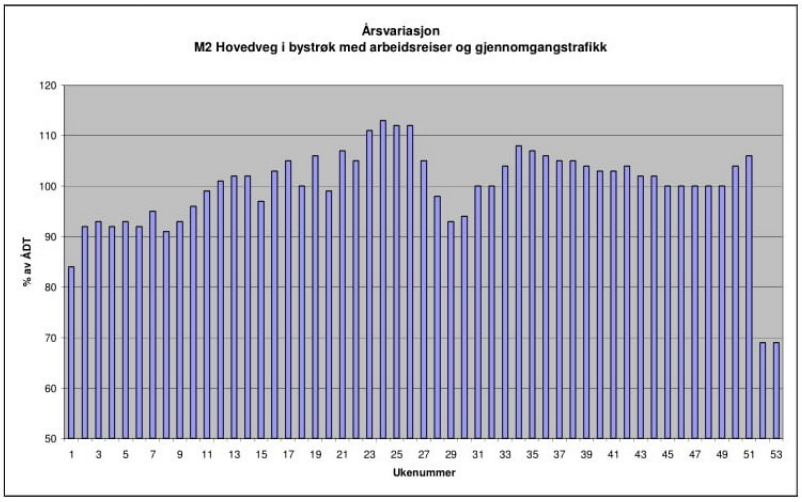

Ukevariasjon

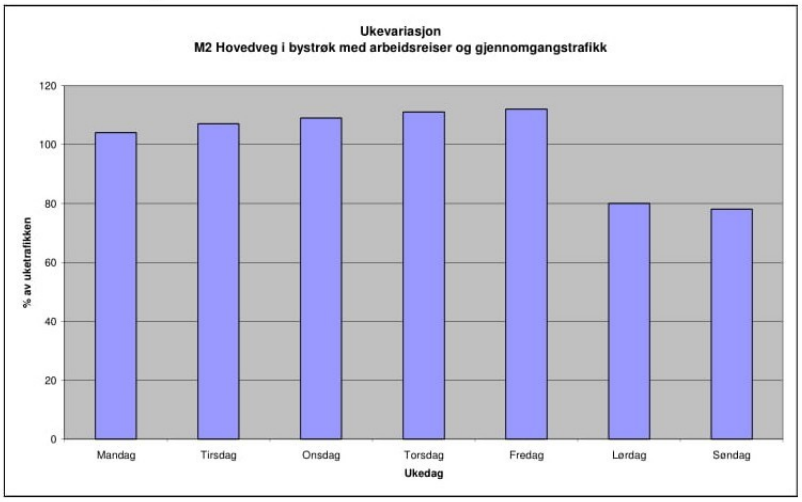

Døgnvariasjon

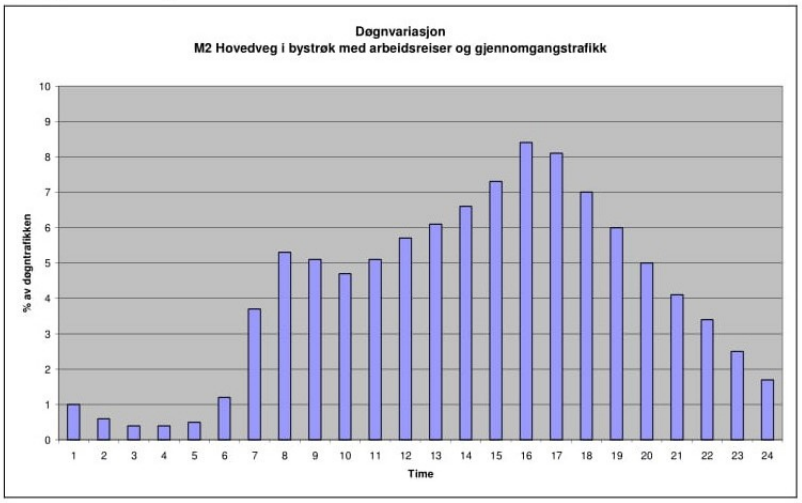

Source: [Gryteselv et al., 2014]

Appendix C

Additional equations

Potential temperature

From Wallace and Hobbs [2006]

$$\theta(z) = T(z)\left(\frac{p_0}{p(z)}\right)^{R/c_p}$$

with

$$p(z) = p_0 exp(-z/H)$$

p_0 is surface pressure, R the universal gas constant, c_p heat capacity of air. An estimated scale height of H=8000m was used.

Statistics

Root mean square error:

$$RMSE = \sqrt{\frac{1}{N}\sum_{i=1}^{N}(M_i - O_i)^2}$$

Mean bias:

$$MB = \frac{1}{N}\sum_{i=1}^{N}(M_i - O_i)$$

Correlation coefficient:

$$r = \frac{\sum_{i=1}^{N}(O_i - \overline{O})(M_i - \overline{M})}{\sqrt{\sum_{i=1}^{N}(O_i - \overline{O})^2}\sqrt{\sum_{i=1}^{N}(M_i - \overline{M})^2}}$$

M denotes Modeled, O denotes Observed and the overbar indicates the mean value.

Lifetime for NO

$$\tau_{NO} = \frac{1}{k[O_3]} = \frac{1}{1.5 \cdot 10^{-14} cm^3/s \cdot molec \cdot 5.2 \cdot 10^{11} molec/cm^3} = 167s \approx 2.8min$$

where $[O_3]$ = 20ppb and T=273K

Appendix D

Air Quality stations

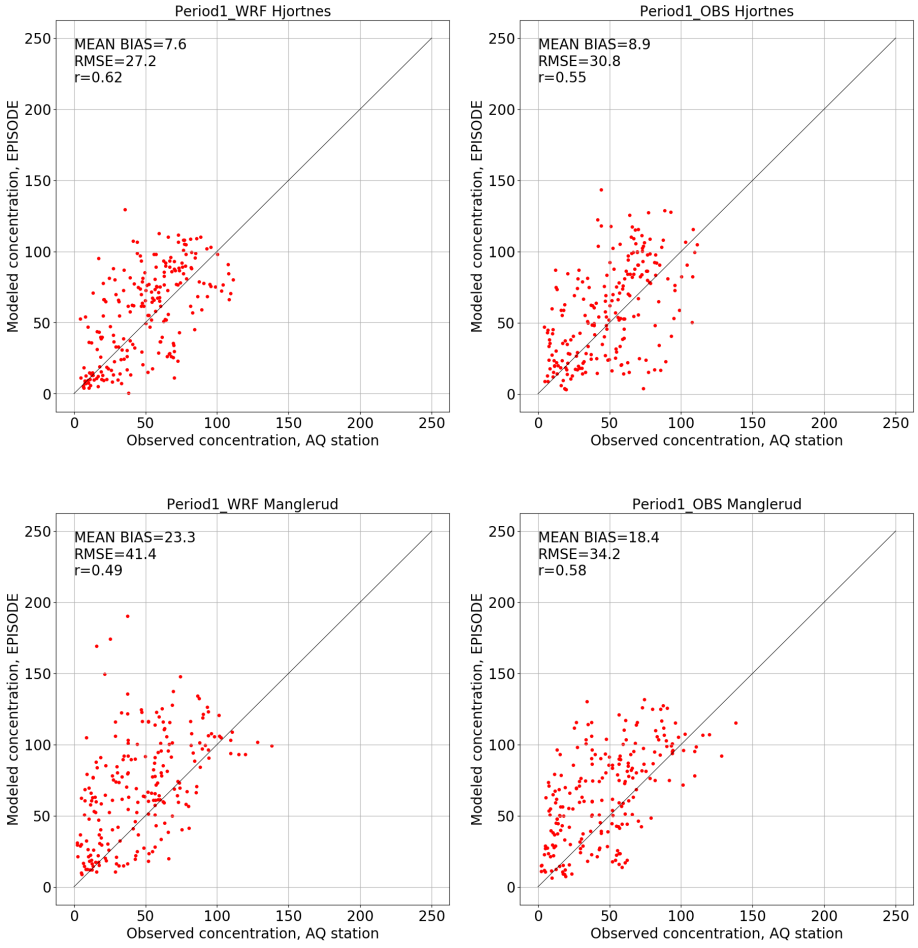

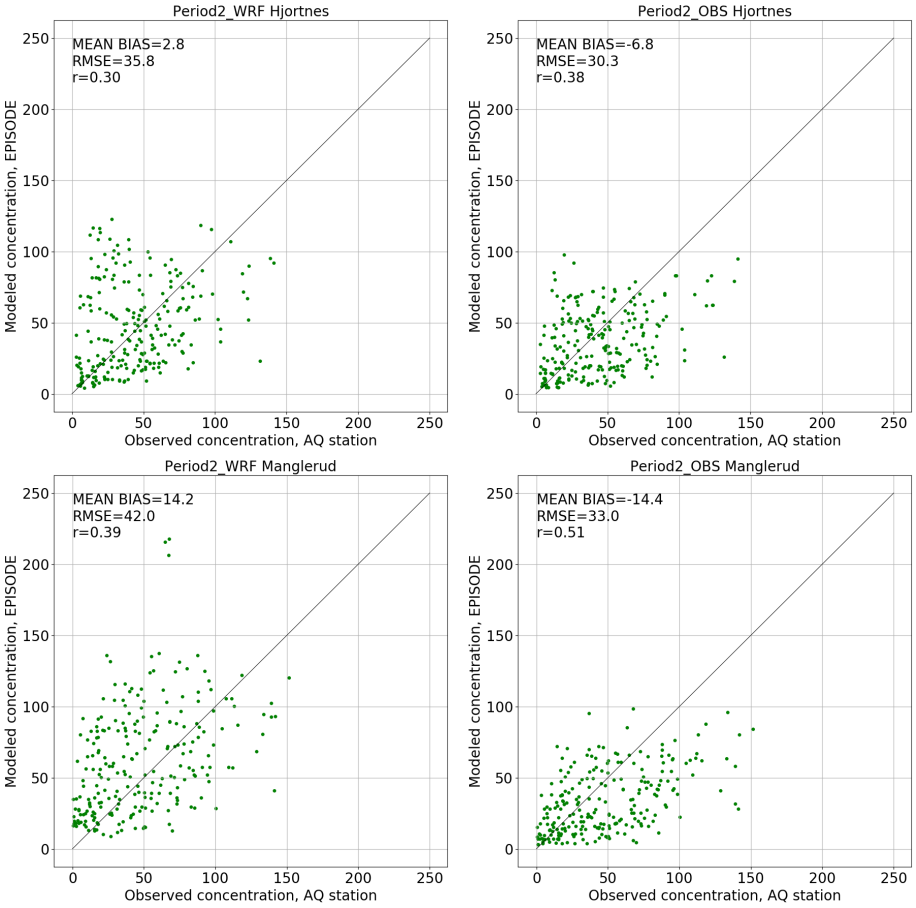
Period2_WRF Hjortnes
MEAN BIAS=2.8
RMSE=35.8
r=0.30
Period2_OBS Hjortnes
MEAN BIAS=-6.8
RMSE=30.3
r=0.38
Period2_WRF Manglerud
MEAN BIAS=14.2
RMSE=42.0
r=0.39
Period2_OBS Manglerud
MEAN BIAS=-14.4
RMSE=33.0
r=0.51
Modeled concentration, EPISODE
Observed concentration, AQ station
0
50
100
150
200
250

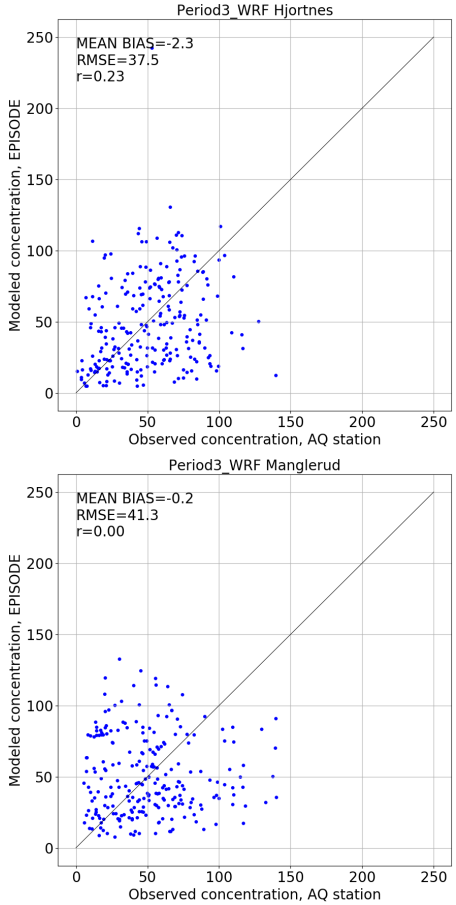
Period3_WRF Hjortnes
MEAN BIAS=-2.3
RMSE=37.5
r=0.23
Modeled concentration, EPISODE
Observed concentration, AQ station
0
50
100
150
200
250
Period3_WRF Manglerud
MEAN BIAS=-0.2
RMSE=41.3
r=0.00
Modeled concentration, EPISODE
Observed concentration, AQ station

Bibliography

S Pal Arya. *Air pollution meteorology and dispersion*, volume 6. Oxford University Press New York, 1999.

O. Badr and S. D. Probert. Oxides of Nitrogen in the Earth's Atmosphere: Trends, Sources, Sinks and Environmental Impacts. *Applied Energy*, 46:1–67, 1993.

Robert F. Banks, Jordi Tiana-Alsina, José María Baldasano, Francesc Rocadenbosch, Alexandros Papayannis, Stavros Solomos, and Chris G. Tzanis. Sensitivity of boundary-layer variables to PBL schemes in the WRF model based on surface meteorological observations, lidar, and radiosondes during the HygrA-CD campaign. *Atmospheric Research*, 176-177:185–201, jul 2016. ISSN 0169-8095. doi: 10.1016/J.ATMOSRES.2016.02.024. URL `https://www.sciencedirect.com/science/article/pii/S0169809516300412`.

Ekaterina Batchvarova and Sven-Erik Gryning. Applied model for the growth of the daytime mixed layer. *Boundary-Layer Meteorology*, 56(3):261–274, aug 1991. ISSN 0006-8314. doi: 10.1007/BF00120423.

T. Bøhler. MEPDIM. The NILU Meteorological Processor for Dispersion Modelling. Version 1.0. Model description. *Norwegian Institute for Air Research, Kjeller, (NILU F 4/98)*, 1996.

R. Briant, C. Seigneur, M. Gadrat, and C. Bugajny. Evaluation of roadway Gaussian plume models with large-scale measurement campaigns. *Geosci. Model Dev*, 6: 445–456, 2013. doi: 10.5194/gmd-6-445-2013. URL `www.geosci-model-dev.net/6/445/2013/`.

J. A. Businger, J. C. Wyngaard, Y. Izumi, E. F. Bradley, J. A. Businger, J. C. Wyngaard, Y. Izumi, and E. F. Bradley. Flux-Profile Relationships in the Atmospheric Surface Layer. *Journal of the Atmospheric Sciences*, 28(2): 181–189, mar 1971. ISSN 0022-4928. doi: 10.1175/1520-0469(1971)028⟨0181:FPRITA⟩2.0.CO;2. URL `http://journals.ametsoc.org/doi/abs/10.1175/1520-0469{%}281971{%}29028{%}3C0181{%}3AFPRITA{%}3E2.0.CO{%}3B2`.

Alan J. Cimorelli, Steven G. Perry, Akula Venkatram, Jeffrey C. Weil, Robert J. Paine, Robert B. Wilson, Russell F. Lee, Warren D. Peters, Roger W. Brode, Alan J. Cimorelli, Steven G. Perry, Akula Venkatram, Jeffrey C. Weil, Robert J. Paine, Robert B. Wilson, Russell F. Lee, Warren D. Peters, and Roger W. Brode. AERMOD: A Dispersion Model for Industrial Source Applications. Part I: General

Model Formulation and Boundary Layer Characterization. *Journal of Applied Meteorology*, 44(5):682–693, may 2005. ISSN 0894-8763. doi: 10.1175/JAM2227.1. URL http://journals.ametsoc.org/doi/abs/10.1175/JAM2227.1.

Yves Delage. Parameterising sub-grid scale vertical transport in atmospheric models under statically stable conditions. *Boundary-Layer Meteorology*, 82(Section 3): 23–48, jan 1997. ISSN 1573-1472. doi: 10.1023/A:1000132524077. URL http://link.springer.com/10.1023/A:1000132524077.

Bruce Denby and Ingrid Sundvor. Air quality mapping of NO2 with the use of passive samplers. *Norwegian Institute for Air Research, Kjeller (NILU OR 65/2008)*, 2008.

A. J. Dyer. A review of flux-profile relationships. *Boundary-Layer Meteorology*, 7 (3):363–372, nov 1974. ISSN 00068314. doi: 10.1007/BF00240838. URL http://link.springer.com/10.1007/BF00240838.

Martin Ferm and Henning Rohde. Measurements of Air Concentrations of SO2, NO2 and NH3 at Rural and Remote Sites in Asia. *Journal of Atmospheric Chemistry*, 27(1):17–29, 1997. ISSN 01677764. doi: 10.1023/A:1005816621522.

P. Fisher, J. Kukkonen, M. Piringer, M. W. Rotach, and M. Schatzmann. Meteorology applied to urban air pollution problems: concepts from COST 715. *Atmospheric Chemistry and Physics Discussions*, 2006. ISSN 1680-7375. doi: 10.5194/acpd-5-7903-2005.

Donald Golder. Relations among stability parameters in the surface layer. *Boundary-Layer Meteorology*, 3(1):47–58, sep 1972. ISSN 0006-8314. doi: 10.1007/BF00769106. URL http://link.springer.com/10.1007/BF00769106.

Kristin Gryteselv, Malin Eriksson, and Torbjørn Haugen. Veileder i trafikkdata. Nr. V714 i Statens vegvesens håndbokserie. 2014. URL https://www.vegvesen.no/{_}attachment/256135/binary/997080.

David Heist, Vlad Isakov, Steven Perry, Michelle Snyder, Akula Venkatram, Christina Hood, Jenny Stocker, David Carruthers, Saravanan Arunachalam, and R. Chris Owen. Estimating near-road pollutant dispersion: A model intercomparison. *Transportation Research Part D: Transport and Environment*, 25: 93–105, dec 2013. ISSN 13619209. doi: 10.1016/j.trd.2013.09.003.

Nina Holmengen and Nadiya Fedoryshyn. Utslipp fra veitrafikken i Norge. 2015. URL https://www.ssb.no/natur-og-miljo/artikler-og-publikasjoner/{_}attachment/225115?{_}ts=14ce05a5658.

Daniel J. Jacob. *Introduction to atmospheric chemistry*. Princeton University Press, 1999. ISBN 1400841542. URL https://books.google.no/books?hl=no{&}lr={&}id=7B8EEn{_}sj0cC{&}oi=fnd{&}pg=PP1{&}ots=6LAr{_}L4Dt6{&}sig=dfr5JQo13J6wtRDGMA4oy9Awxyc{&}redir{_}esc=y{#}v=onepage{&}q{&}f=false.

Sue Kimbrough, R. Chris Owen, Michelle Snyder, and Jennifer Richmond-Bryant. NO to NO2 conversion rate analysis and implications for dispersion model chemistry methods using Las Vegas, Nevada near-road field measurements. *Atmospheric Environment*, 165:23–34, sep 2017. ISSN 1352-2310. doi: 10.1016/J.ATMOSENV.2017.06.027.

Junsei Kondo and Hiromi Yamazawa. Aerodynamic roughness over an imhomogeneous ground surface. *Boundary-Layer Meteorology*, 35(4):331–348, jun 1986. ISSN 0006-8314. doi: 10.1007/BF00118563. URL http://link.springer.com/10.1007/BF00118563.

Ute Latza, Silke Gerdes, and Xaver Baur. Effects of nitrogen dioxide on human health: Systematic review of experimental and epidemiological studies conducted between 2002 and 2006. *International Journal of Hygiene and Environmental Health*, 212(3):271–287, may 2009. ISSN 1438-4639. doi: 10.1016/J.IJHEH.2008.06.003. URL https://www.sciencedirect.com/science/article/pii/S1438463908000539.

Jean François Louis. A parametric model of vertical eddy fluxes in the atmosphere. *Boundary-Layer Meteorology*, 17(2):187–202, sep 1979. ISSN 00068314. doi: 10.1007/BF00117978. URL http://link.springer.com/10.1007/BF00117978.

T. J. Lyons and W. D. Scott. *Principles of air pollution meteorology*. Belhaven, 1990. ISBN 1852930799.

Manju Mohan and T.A. Siddiqui. Analysis of various schemes for the estimation of atmospheric stability classification. *Atmospheric Environment*, 32(21):3775–3781, nov 1998. ISSN 1352-2310. doi: 10.1016/S1352-2310(98)00109-5.

A. S. Monin and A. M. Obukhov. Basic laws of turbulent mixing in the surface layer of the atmosphere. *Inst. Contract Number*, 24(19604):163–187, 1954. URL http://www4.ncsu.edu/{~}gary/mea716/pdf{_}pbl/Monin{_}and{_}Obukhov{_}1954.pdf.

F. T. M. Nieuwstadt. The Turbulent Structure of the Stable, Nocturnal Boundary Layer. *Journal of the Atmospheric Sciences*, 41(14):2202–2216, jul 1984. ISSN 0022-4928. doi: 10.1175/1520-0469(1984)041⟨2202:TTSOTS⟩2.0.CO;2. URL http://journals.ametsoc.org/doi/abs/10.1175/1520-0469{%}281984{%}29041{%}3C2202{%}3ATTSOTS{%}3E2.0.CO{%}3B2.

William H. Press. *Numerical Recipes : The Art of Scientific Computing*. Cambridge University Press, 2007. ISBN 0521880688. URL https://books.google.no/books?hl=no{&}lr={&}id=1aAOdzK3FegC{&}oi=fnd{&}pg=PA1{&}dq=william+et+al+2007{&}ots=3kPjHeHnnj{&}sig=T27r9UojYWJHHONq031CAKUBJNo{&}redir{_}esc=y{#}v=onepage{&}q=romberg{&}f=false.

Wenjun Qian and Akula Venkatram. Performance of Steady-State Dispersion Models Under Low Wind-Speed Conditions. *Boundary-Layer Meteorology*, 138(3):

475–491, mar 2011. ISSN 0006-8314. doi: 10.1007/s10546-010-9565-1. URL http://link.springer.com/10.1007/s10546-010-9565-1.

E Samoli, E Aga, G Touloumi, K Nisiotis, B Forsberg, A Lefranc, J Pekkanen, B Wojtyniak, C Schindler, E Niciu, R Brunstein, M Dodic Fikfak, J Schwartz, and K Katsouyanni. Short-term effects of nitrogen dioxide on mortality: an analysis within the APHEA project. *The European respiratory journal*, 27(6): 1129–38, jun 2006. ISSN 0903-1936. doi: 10.1183/09031936.06.00143905. URL http://www.ncbi.nlm.nih.gov/pubmed/16540496.

John H Seinfeld and Spyros N Pandis. *Atmospheric chemistry and physics: from air pollution to climate change*. John Wiley & Sons, 2016.

William C Skamarock, Joseph B Klemp, Jimy Dudhia, David O Gill, Dale M Barker, Michael G Duda, Xiang-Yu Huang, Wei Wang, and Jordan G Powers. A Description of the Advanced Research WRF Version 3. *NCAR Technical Note*, 2008.

L.H. Slørdal, S.E. Walker, and S. Solberg. The urban air dispersion model EPISODE applied in AirQUIS2003. Technical Description. *Norwegian Institute for Air Research, Kjeller (NILU TR 12/03)*, 2003.

Michelle G. Snyder, Akula Venkatram, David K. Heist, Steven G. Perry, William B. Petersen, and Vlad Isakov. RLINE: A line source dispersion model for near-surface releases. *Atmospheric Environment*, 2013. ISSN 13522310. doi: 10.1016/j.atmosenv.2013.05.074.

John M. Stockie. The Mathematics of Atmospheric Dispersion Modeling. *SIAM Review*, 53(2):349–372, jan 2011. ISSN 0036-1445. doi: 10.1137/10080991X. URL http://epubs.siam.org/doi/10.1137/10080991X.

Roland. Stull. *An Introduction to Boundary Layer Meteorology*. Springer Netherlands, Dordrecht, 1988. ISBN 978-90-277-2769-5. doi: 10.1007/978-94-009-3027-8. URL http://link.springer.com/10.1007/978-94-009-3027-8.

Roland. Stull. *Practical Meteorology - An Algebra-based Survey of Atmospheric Science*. University of British Columbia, 2012. ISBN 978-0-88865-178-5. doi: 10.14288/1.0300441. URL https://www.eoas.ubc.ca/books/Practical{_}Meteorology/world/print.html.

A. P. Van Ulden, A. A. M. Holtslag, A. P. Van Ulden, and A. A. M. Holtslag. Estimation of Atmospheric Boundary Layer Parameters for Diffusion Applications. *Journal of Climate and Applied Meteorology*, 24(11):1196–1207, nov 1985. ISSN 0733-3021. doi: 10.1175/1520-0450(1985)024⟨1196:EOABLP⟩2.0.CO;2. URL http://journals.ametsoc.org/doi/abs/10.1175/1520-0450{%}281985{%}29024{%}3C1196{%}3AEOABLP{%}3E2.0.CO{%}3B2.

A. Venkatram. Estimating the Monin-Obukhov length in the stable boundary layer for dispersion calculations. *Boundary-Layer Meteorology*, 19(4):481–485, dec 1980. ISSN 0006-8314. doi: 10.1007/BF00122347. URL http://link.springer.com/10.1007/BF00122347.

Akula Venkatram and T. W. Horst. Approximating dispersion from a finite line source. *Atmospheric Environment*, 40(13):2401–2408, apr 2006. ISSN 1352-2310. doi: 10.1016/J.ATMOSENV.2005.12.014. URL `http://www.sciencedirect.com/science/article/pii/S1352231005011921`.

Akula Venkatram, Michelle G. Snyder, David K. Heist, Steven G. Perry, William B. Petersen, and Vlad Isakov. Re-formulation of plume spread for near-surface dispersion. *Atmospheric Environment*, 77:846–855, oct 2013. ISSN 1352-2310. doi: 10.1016/J.ATMOSENV.2013.05.073.

John M. Wallace and Peter Victor Hobbs. *Atmospheric science : an introductory survey*. Elsevier Academic Press, 2006. ISBN 9780127329512.

S. S. Zilitinkevich. On the determination of the height of the Ekman boundary layer. *Boundary-Layer Meteorology*, 3(2):141–145, dec 1972. ISSN 00068314. doi: 10.1007/BF02033914. URL `http://link.springer.com/10.1007/BF02033914`.